Doctoral Dissertation

Physicochemical Properties of Molten Slag and Liquid Fe in Fe Extraction from Lunar Regolith

Sunglock Lim

July 2024

Division of Materials and Manufacturing Science
Graduate School of Engineering
Osaka University

Table of Contents

Chapter 1
Introduction

1.1 Lunar Metallurgy

The exploration and utilization of extraterrestrial resources are crucial for the sustainable development of humanity and the expansion of space activities. In particular, the development of lunar resources is being considered as the first step in human space exploration. The Moon is a celestial body close to the Earth and is known to contain various resources, such as helium-3, rare earth elements, oxygen, hydrogen, and metals [1]. Among these resources, metals are essential elements for various activities, construction, and energy generation on the Moon. Therefore, extracting metals from lunar regolith, with a focus on physicochemical properties, is crucial for ensuring the sustainable use of future resources and advancing metallurgical technology, which is defined as “Lunar Metallurgy”.

A deep understanding of lunar regolith is essential to beginning lunar metallurgy. This regolith, which consists of fragmented and unconsolidated rocky material, blankets the lunar surface. This layer was formed by the continuous impact of meteoroids of various sizes and the steady bombardment of charged particles from the sun and stars [1]. Regolith typically has a thickness of about 4–5 meters in the mare regions and 10–15 meters in the highlands, and it includes materials of all sizes, from large rocks to micron-sized dust particles [1]. Compositionally, lunar regolith consists of silicate minerals, including plagioclase feldspar; $(Ca,Na)(Al,Si)_4O_8$, pyroxene; $(Ca,Fe,Mg)_2Si_2O_6$, and olivine; $(Mg,Fe)_2SiO_4$, as well as minor amounts of metallic iron, ilmenite; $(Fe,Mg)TiO_3$. The particle size distribution in regolith is highly variable, ranging from fine dust to larger rock fragments [1,2]. Although “lunar soil” is synonymously used for “lunar regolith” in a lexical sense, “lunar soil” typically represents the finer-grained fraction of the unconsolidated regolith on the lunar surface, specifically referring to regolith particles less than 1 cm in size [1]. Lunar regolith holds significant potential for in-situ resource utilization (ISRU), a critical aspect of long-term lunar exploration and colonization. Key resources that can be extracted from lunar regolith include oxygen, silicon, iron, aluminum, and titanium. These elements can be used for life support, construction materials, and a variety of manufactured products. Additionally, water ice discovered in the

polar regions of the Moon could potentially be utilized [3]. This discovery is particularly significant as water is a vital resource for life support and can be split into hydrogen and oxygen for fuel.

Lunar regolith, or soil, varies significantly across different regions of the Moon, primarily divided into Mare (or Maria) and Highlands, as shown in **Fig. 1-1** [1,2]. Mare, which means "sea" in Latin, refers to the dark basaltic regions on the Moon that are rich in iron, titanium, and magnesium, covering low-lying areas of the lunar surface [1]. Mare regions are typically composed of basaltic lava, a type of rock produced from the eruption of volcanoes. Mare basalt lavas were created inside the Moon due to the partial melting of the lunar mantle [1]. In contrast, the "Highlands" are bright, high regions on the lunar surface [1]. The highlands are composed of anorthosite, which is a type of rock that is rich in plagioclase feldspar. Chemically, the lunar highlands are rich in calcium (Ca) and aluminum (Al), whereas the mare is richer in iron (Fe) and titanium (Ti). In terms of rock types, the highlands are composed mostly of old impact-shocked plutonic (deep-seated) rocks, while the mare consists of basaltic lavas [1]. Mineralogically, the highlands are dominated by plagioclase feldspar, whereas the mare is richer in pyroxene [1]. These differences in composition are not just of geological interest but also have implications for resource utilization and metallurgical research. **Table 1-1** represents the major chemical compositions of lunar regolith samples obtained from the mare and highland regions of the Moon through the Apollo and Luna missions [4]. The high metal concentration in the mare regions is the reason why those areas are considered prime candidates for future lunar resource mining.

To utilize lunar resources, various experiments using lunar regolith are necessary. However, obtaining lunar regolith for experiments on the Earth is extremely difficult, posing a significant limitation. A potential solution is to use terrestrial resources to create a simulant similar to lunar regolith. **Table 1-2** shows the chemical compositions of minerals that make up Earth's volcanic rocks [5], which are geologically similar to those on the Moon. This implies that even without directly using lunar regolith, terrestrial resources can be useful for research. **Table 1-3** presents the chemical compositions of lunar regolith simulants developed for research on lunar resource utilization [6,7]: lunar mare simulant (LMS-1) and lunar highland simulant (LHS-1). Mineralogical factors of lunar regolith simulants were also considered to reproduce the chemical stability of lunar regolith. **Table 1-4** shows the mineral compositions of lunar regolith

simulants, all of which are major constituents of rocks. **Table 1-5** shows the chemical compositions of typical steel industry slags originating from blast furnace (BF), basic oxygen furnace (BOF), and electric arc furnace (EAF) processes [8]. Commonalities among the components of lunar regolith, Earth's minerals, and slag can be utilized in designing various studies for future lunar metallurgy.

However, the Moon presents a vastly different environment compared to the Earth. As shown in **Table 1-6**, the Moon has a sixth of Earth's gravity and virtually no atmosphere compared to the Earth [9]. Additionally, there has never been life on the Moon, so there are no fossil fuels. These will act as limiting factors in applying Earth's conventional metallurgical processes to the Moon. Another limiting factor is the significant variation in the composition of lunar regolith. **Table 1-7** presents the range of compositional variation in lunar and terrestrial basalts, which are the primary material of interest for metal extraction on the Moon [2]. From **Table 1-7**, it can be seen that the chemical composition of lunar regolith shows significant variation, especially with respect to TiO_2. Therefore, to efficiently utilize lunar resources, the design of a new metallurgical process considering lunar environment is necessary, and the applicable processes will be discussed in the following section 1.2.

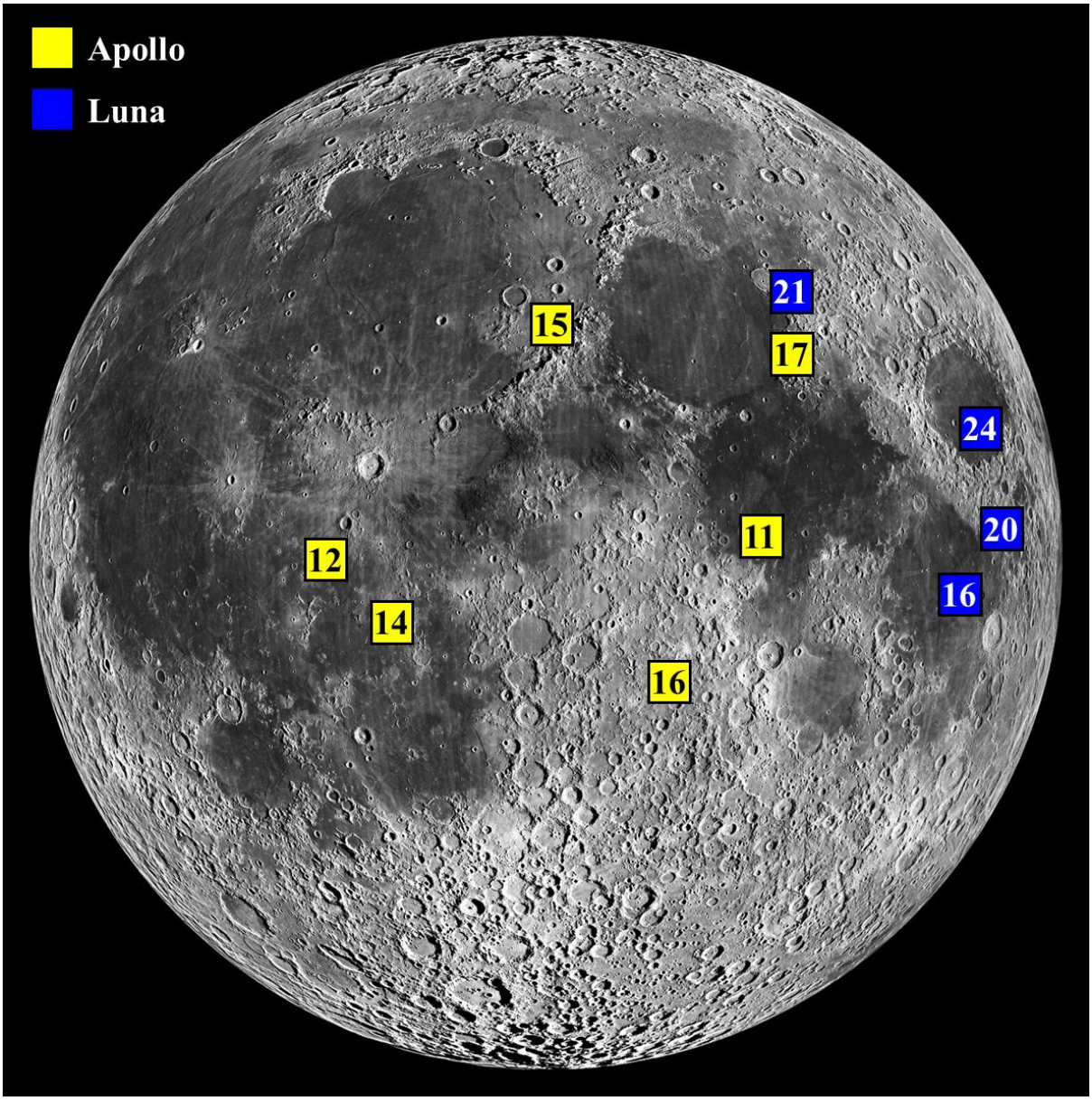

Fig. 1-1 Distinctive contrasts between Mare (dark) and Highland (bright) regions of the lunar surface with selected Apollo and Luna mission locations [1]. Adapted from: NASA/GSFC/Arizona State University [9].

Table 1-1 Chemical compositions (mass%) of main components of lunar regolith by region [4].

Oxide	Mare					Highland	
	High Ti		Low Ti				
	A-11	A-17	A-12	A-15	L-16	A-16	L-20
SiO_2	42.17	39.87	46.17	46.20	43.96	45.09	44.95
CaO	12.12	10.62	10.55	9.74	12.07	15.79	14.07
Al_2O_3	13.78	10.97	13.71	10.32	15.51	27.18	23.07
MgO	8.17	9.62	9.91	11.29	8.79	5.84	9.26
FeO	15.76	17.53	15.41	19.75	16.41	5.18	7.35
TiO_2	7.67	9.42	3.07	2.16	3.53	0.56	0.49
Na_2O	0.44	0.35	0.48	0.31	0.36	0.47	0.35
Cr_2O_3	0.30	0.46	0.35	0.53	0.29	0.11	0.15
MnO	0.21	0.24	0.22	0.25	0.21	0.07	0.11
K_2O	0.15	0.08	0.27	0.10	0.10	0.11	0.08
P_2O_5	0.12	0.07	0.31	0.11	0.14	0.12	0.11

***A**: Apollo mission, **L**: Luna mission

Table 1-2 Mean chemical compositions (mass%) of selected common volcanic rocks [5].

Oxide	Nephelinite	Basanite	Hawaiite	Tephrite	Basalt	Mugearite	Andesite
SiO_2	42.43	45.46	48.65	50.06	50.06	52.72	52.48
CaO	12.32	10.53	8.21	9.34	9.66	10.35	6.14
Al_2O_3	14.90	14.89	16.32	17.31	15.99	14.98	16.98
MgO	6.76	8.93	5.15	4.80	6.96	7.38	2.52
FeO	6.60	8.02	7.73	5.48	7.46	8.22	6.52
Fe_2O_3	5.78	4.14	4.92	4.21	3.92	3.51	5.17
TiO_2	2.71	2.56	3.30	1.80	1.86	1.96	2.11
Na_2O	4.97	3.58	4.15	3.77	2.97	2.44	4.87
K_2O	3.53	1.88	1.58	4.58	1.12	0.45	2.46

Oxide	Andesite	Phonolite	Trachyte	Latite	Dacite	Rhyodacite	Rhyolite
SiO_2	56.86	57.49	62.61	62.80	66.36	67.52	74.00
CaO	6.87	2.80	2.34	4.27	4.29	3.35	1.16
Al_2O_3	17.22	19.47	17.26	16.37	16.12	15.53	13.53
MgO	3.40	1.12	0.95	2.25	1.74	1.68	0.41
FeO	4.26	2.28	2.42	2.27	2.41	1.80	1.16
Fe_2O_3	3.29	2.87	3.07	3.34	2.39	2.46	1.47
TiO_2	0.88	0.64	0.71	0.83	0.58	0.60	0.27
Na_2O	3.54	7.98	5.57	3.88	3.89	3.90	3.62
K_2O	1.67	5.38	5.08	3.98	2.22	3.16	4.38

Table 1-3 Chemical compositions (mass%) of lunar regolith simulants [6,7].

Oxide	LMS-1	LHS-1
SiO_2	42.81	44.18
CaO	5.94	11.62
Al_2O_3	14.13	26.24
MgO	18.89	11.22
FeO_T	7.87	3.04
TiO_2	4.62	0.79
Na_2O	4.92	2.30
MnO	0.15	0.05
Cr_2O_3	0.21	0.02
K_2O	0.57	0.46
P_2O_5	0.44	-
SO_3	0.11	0.10

Table 1-4 Mineral compositions (mass%) of lunar regolith simulants [6,7].

Mineral	LMS-1	LHS-1
Glass-rich basalt	32.0	24.7
Anorthosite	19.8	74.4
Pyroxene	32.8	0.3
Ilmenite	4.3	0.4
Olivine	11.1	0.2

Table 1-5 Typical chemical compositions (mass%) of steel industry slags [8].

Slag	SiO_2	CaO	Al_2O_3	MgO	FeO	Others
Blast furnace (BF) slag	34.0	42.0	13.0	7.4	0.4	
Basic oxygen furnace (BOF) slag	11.0	46.0	2.0	6.5	17.4	Bal.
Electric arc furnace (EAF) slag	12–19	23–55	7–17	5–7	0.3–30	

Table 1-6 Comparison of the features of the Moon and the Earth [9].

Property	Moon	Earth
Mass (10^{24} kg)	0.07346	5.9724
Volume (10^{10} km^3)	2.1968	108.321
Equatorial radius (km)	1738.1	6378.1
Polar radius (km)	1736.0	6356.8
Volumetric mean radius (km)	1737.4	6371.0
Diurnal temperature (K)	95–390	283–293
Total mass of atmosphere (kg)	~25,000	5.1×10^{18}
Surface pressure (bar)	3×10^{-15}	1.014
Ellipticity (Flattening)	0.00120	0.00335
Mean density (kg/m^3)	3344	5514
Surface gravity (m/s^2)	1.62	9.80
Surface acceleration (m/s^2)	1.62	9.78
Escape velocity (km/s)	2.38	11.20
Bond albedo	0.11	0.294
Geometric albedo	0.12	0.434
Solar irradiance (W/m^2)	1361	1361
Black-body temperature (K)	270.4	254.0
Topographic range (km)	13	20
Moment of inertia (I/MR^2)	0.3940	0.3308

Table 1-7 Range in composition (mass%) of mare basalts and the 10-90 percent frequency range of terrestrial continental basalts [2].

Oxide	Moon	Earth
SiO_2	37–49	44–53
CaO	8–12	8–12
Al_2O_3	7–14	13–19
MgO	6–17	4–10
FeO	18–23	7–14
TiO_2	0.3–13	0.9–3.3
Na_2O	0.1–0.5	1.8–3.8
MnO	0.21–0.29	0.09–0.3
K_2O	0.02–0.3	0.3–2.0
P_2O_5	0.03–0.18	0.04–0.6
Cr_2O_3	0.12–0.70	0.005–0.04

1.2 Feasible Processes of In-Situ Metal Extraction for Lunar Resource Utilization

This section discusses methods for the utilization of lunar regolith proposed by various research groups. More than 20 different potential technologies have been proposed for recovering oxygen and metals from lunar regolith [10,11]. Among these, four methods have continued to be actively researched up to the present: Fray-Farthing-Chen Cambridge (FFC), molten oxide electrolysis (MOE), carbothermal reduction (CR), and hydrogen reduction (HR) [10-18]. The processes proposed so far can broadly be categorized into electrochemical processes (FFC, MOE) and pyrometallurgical processes (CR, HR). The proposed processes have been proven to be efficient by various research groups, but there are still challenges to be solved for application to the extreme lunar environment. This section introduces two processes (MOE, HR) that are considered potentially promising when taking into account the lunar environment.

1.2.1 Molten Oxide Electrolysis (MOE) Process

The molten oxide electrolysis (MOE) process, also known as the "magma" or "molten regolith electrolysis" (MRE) process, is an electrochemical technique that directly electrolyzes molten lunar regolith to produce oxygen and metals [12-24]. **Figure 1-2** shows a schematic diagram of the MOE process. The MOE process shares a reduction mechanism similar to that of the Hall-Héroult process used in aluminum production [13-15]. However, a key difference lies in the compensating oxidation reaction at the anode. While the Hall-Héroult process produces carbon dioxide due to the consumption of the carbon anode, the MOE process generates oxygen, relying on the use of an inert anode. As shown in **Figure 1-2**, when applying the electromotive force, oxygen anions (O^{2-}) move through the molten regolith to the anode [12-18], and they are oxidized and form gaseous oxygen (O_2) from the melt. Metal cations (M^{n+}) ionized from metal oxides move to the cathode, where they are reduced to liquid or solid metal (M) at the cathode. The MOE process requires an electrolysis cell operating at temperatures up to 1873 K, at which the lunar regolith melts, and an electric potential is applied to produce oxygen at the anode and deposit metals at the cathode [12-24].

$$\text{Anode: } O^{2-} = 0.5O_2 + 2e^- \qquad (1-1)$$

$$\text{Cathode: } M^{n+} + ne^{-} = M \qquad (1-2)$$

A major advantage of the MOE process is that it does not require additional reactants to produce oxygen and metals. This process does not require the input of reducing agents (such as hydrogen or carbon) or consumable reagents and does not rely on linking multiple processes to obtain refined products, making the process relatively simple [16]. Furthermore, it is reported that the MOE process exhibits uncommon versatility to feedstock composition in electrolysis since lunar regolith is used as the electrolyte [16]. In other words, the MOE process can utilize various lunar resources with different compositions from different regions of the Moon without requiring additional electrolytes from the Earth. This aspect makes it ideal for materials like lunar regolith with significant compositional variations [16]. Additionally, this process allows for the selective extraction of iron, titanium, and silicon by controlling the applied potential [18,20]. In theory, all metal oxides can be reduced through molten oxide electrolysis. Although the oxide precipitates in molten oxide sometimes disturb further reactions, reduction progresses even when the oxide composition changes to form $MgAl_2O_4$ spinel [12,18]. The mass of oxygen discharged per hour is proportional to the current and can be explained using Faraday's law as expressed by the following equation [12,16].

$$W_{O_2} = \varepsilon \frac{MIt}{ZF} \qquad (1-3)$$

where ε is current efficiency (%), M is the molecular weight (g/mol), I is current intensity (A), t is electrolysis time (seconds), Z is the valency (Z = 4 for O_2), and F is the Faraday constant (F = 96485 C/mol). In terms of electrolysis efficiency (oxygen evolution) in the MOE process, it is preferable for the electrolyte to have high electrical conductivity. In molten slag with high electrical conductivity, current increases, and electrochemical reaction is accelerated. This contributes to increasing the reduction rate of metal oxides and the productivity of oxygen. Additionally, low power loss improves the energy efficiency of the electrolysis process. That is, since electrical conductivity is the reciprocal of resistance, lower resistance in the electrolyte increases conductivity and thus improves electrolysis efficiency. However, electrical resistance occurs when an electric current flows through the electrolyte between electrodes in the electrolytic cell. This electrical resistance generates Joule heating, providing a high-

temperature environment suitable for the reaction to occur. Therefore, a certain amount of current is used for the Joule heating [12,13,20,21]. In addition, from the viewpoint of Joule heating generation, if the electrical resistance of the electrolyte is low, Joule heating may decrease. Since Joule heating is proportional to the square of the current and the resistance, when the current is constant, a decrease in the resistance of the electrolyte leads to a reduction in Joule heating generation. If the generation of Joule heating decreases, it is difficult to maintain the temperature of the electrolyte. Therefore, in the MOE process, the electrical resistance of the electrolyte requires an appropriate balance between conductivity and resistance for Joule heating generation.

The presence of iron in molten lunar regolith may reduce the efficiency of oxygen generation. The different oxidation states of iron have been reported to cause parasitic effects due to electron conduction, thereby decreasing the efficiency of the cathodic current used for oxygen generation [12,13,18,20]. The parasitic oxidation of iron oxide is a reaction in which ferrous ions (Fe^{2+}) in the molten slag lose electrons and become ferric ions (Fe^{3+}), as follows.

$$\text{Anode: } Fe^{2+} = Fe^{3+} + e^{-} \qquad (1-4)$$

In molten regolith, anions tend to move toward the anode and cations toward the cathode. Ideally, oxygen ions at the anode should lose electrons and be oxidized, but Fe^{2+} loses electrons and is oxidized instead [12,13,18,20]. Parasitic oxidation of Fe^{2+} at the anode reduces the opportunity for oxidation reactions of oxygen ions, thereby reducing the efficiency of oxygen production reactions, which means that less oxygen is generated for a given current [20]. As shown in **Table 1-1**, lunar regolith contains iron oxide, and its concentration is significantly higher in the mare regions compared to the highland regions. This could be a limiting factor for the application of the MOE process on the Moon. Sibille et al. [20] reported that the removal of iron in the initial stage of electrolysis could bring the current efficiency close to 100%.

One of the issues considered in the realization of the MOE process is the high-temperature inert anode. The MOE process involves electrolysis at high temperatures (around 1873 K); thus, the anode must satisfy various physical, chemical, and electrochemical properties to withstand corrosion. Sadoway's group [14,15] has reported that the desired inert anode for the MOE process should possess the following characteristics: (a) Temperatures that exceed the melting

point of iron. (b) Electrochemically stable. (c) Evolution of pure oxygen gas at atmospheric pressure. (d) Mechanically robust. The selection of an inert anode material with high oxygen evolution capability and corrosion resistance is a crucial consideration for the MOE process. Platinum group metals (platinum, iridium) have demonstrated promising performance in this regard. Among these metals, iridium exhibits greater potential than platinum. It is known that platinum anodes exhibit poor mechanical strength when immersed in molten slag with high viscosity above 1573 K, whereas iridium is known for its superior electrochemical stability and higher strength at elevated temperatures [22]. It has been reported that iridium, with a high melting point and chemical inertness, is widely used in the manufacture of oxide-based single crystals, and does not chemically interact with silicate-based molten oxides at temperatures up to 2273 K [22]. Sadoway et al. [13-15] have demonstrated that iridium anodes can extract oxygen from lunar regolith and various silicate-based molten oxides. Additionally, according to research by Kim et al. [15], iridium is considered more suitable for silicate-based electrolytes like lunar regolith. Kim et al. [15] investigated the use of iridium as an anode for the MOE process in two types of electrolytes: a basic slag (57.9 mol%CaO–10.3 mol%MgO–31.8 mol%Al_2O_3) and an acidic slag (45.5 mol%SiO_2–19.1 mol%CaO–23.6 mol%MgO–11.7 mol%Al_2O_3) electrolytes. Here, “basic slag” refers to a melt with high contents of magnesia or calcia, while “acidic slag” refers to a melt with high silica content. Their research showed that the basicity of the electrolyte dramatically affects the stability of the iridium anode in the MOE process. In their study, the rate of iridium loss was much lower in acidic melts with high silica content compared to basic melts with high calcium oxide content. The weight loss of the anode was 20 times higher in the high-calcia melt compared to the high-silica melt. The difference in anode weight loss is attributed to the attack of iridium by basic melts due to the high concentration of free oxide ion coupled with the low viscosity, which results in unimpaired mass transport. Therefore, iridium anodes are reported to be suitable only as oxygen-evolving anodes in acidic melts [15]. Since lunar regolith has a high-silica content as shown in **Table 1-1**, it seems reasonable to use iridium as the material for the anode in the MOE process. However, the high operating temperatures of the MOE process pose various challenges related to the available battery and electrode materials. Kim et al. [15] have reported that at high temperatures, iridium metal can react with oxygen to form volatile iridium oxide or stable solid iridium oxide. Additionally, iridium is extremely scarce, with an abundance of about 0.4 ppb in the Earth’s

crust, making it difficult and expensive to secure sufficient quantities [23]. Additionally, iridium has extremely high hardness, which presents significant processing challenges.

Another factor to consider is the stability of the electrolysis cell. The molten regolith is chemically aggressive, posing challenges in selecting appropriate refractory-containing materials. Refractory materials containing large amounts of Al_2O_3 and MgO can cause rapid deterioration due to reactions between molten lunar regolith [24]. Additionally, since pure oxygen is generated within the MOE reactor, the materials in contact with the molten regolith should not oxidize upon reaction with the produced oxygen [24]. Yttria-stabilized zirconia (YSZ) has been reported as a promising refractory oxide exhibiting limited reactivity [24,25]. However, the high concentration of FeO in lunar regolith can not only reduce current efficiency due to parasitic oxidation but also promote reactivity with the electrolytic cell. Yu et al. [24] reported that the higher FeO and MgO content in mare regions compared to highland regions could increase the reactivity with YSZ crucibles, indicating the highland composition is more suitable for prolonged contact with molten lunar regolith.

As previously described, several studies on the MOE process for utilizing lunar regolith have been actively conducted, and it has been confirmed that continuous oxygen and metal production through stable electrolytic cell operation is essential for successful application on the Moon. From the material perspective for the electrolysis cell, the high-temperature inert anodes and refractories must be developed based on a fundamental electrochemistry and thermodynamics standpoints. In addition, the transport property, such as electrical conductivity, for molten lunar regolith, is a critical issue for the optimal process conditions for realizing high throughput and low energy consumption. Here, comprehensive and accurate information on the electrical conductivity for multicomponent oxide systems is strongly required. However, the existing data and estimation models of electrical conductivity for multicomponent oxide systems targeting lunar regolith are insufficient.

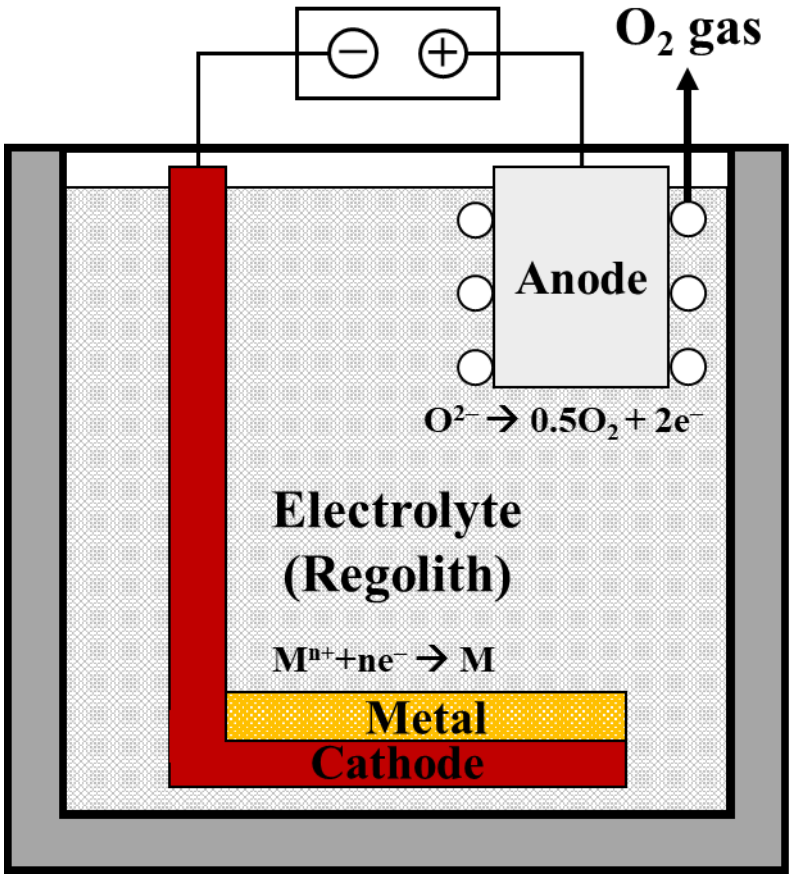

Fig. 1-2 Schematic of molten oxide electrolysis process.

1.2.2 Hydrogen Reduction (HR) Process

The hydrogen reduction process is a pyrometallurgical method aiming at reducing oxides in lunar regolith to obtain oxygen and metals. Since oxygen and metals are strongly bound within the minerals, a significantly strong reducing agent is required for the reaction to occur, and hydrogen is the prominent reducing agent for ISRU on the Moon [18]. The application of the hydrogen reduction process on the Moon also considers the extraction of oxygen, unlike the metallurgical process on the Earth, which mainly targets metal extraction. The overall gas-solid reaction between hydrogen and metal oxides is given as follows.

$$MO + H_2 = M + H_2O \qquad (1-5)$$

Here, hydrogen reacts with the metal oxides (MO) in the regolith to separate the oxygen with the formation of water (H_2O). The water produced from the reaction is electrolyzed in the electrolysis cell subsystem to generate oxygen, and the hydrogen can be recycled [12,17,18]. The primary target of the hydrogen reduction process is the iron oxide (FeO) in the lunar regolith. Therefore, the yield of this process depends on the content of iron oxide in the feedstock. Iron oxide exists in various minerals within the lunar regolith, and it has been reported that the reduction extent varies depending on the type of mineral containing iron oxide [17]. Mare basalt contains a particularly abundant iron oxide, and the main minerals within the basalt include ilmenite, olivine, and pyroxene. Meanwhile, many investigations have been conducted on these minerals for their potential for oxygen and metallic iron extraction [12,17,18,26-33]. Ilmenite $(Fe,Mg)TiO_3$ is a black mineral that reflects the high TiO_2 content of basalts, and is the most easily reducible mineral containing iron oxide found in lunar regolith [32,33]. The direct reduction process of ilmenite in lunar regolith using hydrogen has long been proposed as a potential method for producing water on the Moon [12,17,18,26-33]. The hydrogen reduction of ilmenite can operate at a moderate temperature of about 1173 K [31]. The hydrogen reduction of lunar ilmenite proposed for oxygen production is a two-step process [12,17,18,26-33].

$$FeTiO_3 + H_2 = Fe + TiO_2 + H_2O \qquad (1-6)$$

$$H_2O = H_2 + 0.5O_2 \qquad (1-7)$$

In the first step, iron oxide in ilmenite is reduced, and oxygen is released to form water. Then, in the second step, the water is electrolyzed into hydrogen and oxygen, with the hydrogen being recycled back into the reactor and the oxygen being liquefied for storage [32]. Here, the equilibrium constant of Eq. (1-7) determines the ratio of partial pressures of hydrogen and water [12]. To sustain the reduction process, the water vapor produced by the reaction must be continuously removed from the gas phase.

Gibson et al. [31] investigated the feasibility of the hydrogen reduction process on actual lunar soil samples containing high concentrations of TiO_2 (Lunar sample 70035) at 1173–1323 K. Lunar sample 70035 is an ilmenite basalt of plagioclase-poikilitic, mainly composed of clinopyroxene, plagioclase, and ilmenite [31,34,35]. The composition of 70035 is listed in **Table 1-8** along with the compositions of other samples to be described later [31-33]. In all experiments, water evolution began almost immediately [31]. Lunar sample 70035 contains FeO in ilmenite as well as in olivine and pyroxene. The ilmenite in the 70035 samples was completely reduced, while olivine and pyroxene can be partially reduced. This means that the major contributor to the oxygen yield is the reaction of ilmenite due to the faster reduction of ilmenite. On the other hand, it has been reported that TiO_2 (rutile), a byproduct of ilmenite reduction, can be further reduced at sufficiently high temperatures [17,31,36,37].

Allen et al. [32] also reported the results similar to Gibson's results [31,32]. They performed sub-solidus reduction experiments on two lunar samples (titanium-rich mare soil, 75061 and iron-rich volcanic glass, 74220) with hydrogen at the temperatures between 1173–1373 K. Sample 75061 is one of the most titanium-rich soils in the Apollo collection, with its main components including agglutinates, basalt, pyroxene, ilmenite, plagioclase, and breccia, accompanied by minor olivine and volcanic glass [38]. Lunar sample 74220 is referred to as "orange soil", and the majority of the sample consists of orange spheres that are entirely glassy [39]. The compositions of these samples are shown in **Table 1-8**. In their experiments, the iron in ilmenite was completely reduced to metal and the partial reduction of iron occurs in olivine and pyroxene as well as in Gibson's research [31]. They conclude that ilmenite has been found to be the most reactive among the major crystalline phases in mare soil [31,32].

In addition, as a follow-up to the above study, Allen et al. [33] additionally conducted

experiments on 16 lunar soil and 3 lunar pyroclastic glass samples. For example, they used highland and mare soils, Apollo 17 orange, black glass, and Apollo 15 green glass as experimental samples, and reduced them in a hydrogen flow at 1323 K. Based on the results of oxygen production rate, it was found that total oxygen evolution is closely correlated with the initial iron content of each sample, which is in good agreement with their previous findings [31,32]. They also demonstrated the possibility of extracting oxygen from TiO_2 and SiO_2. The reagent-grade TiO_2 samples were reduced at 1323 K to obtain the reduction rate corresponding to the reduction of TiO_2 to Ti_4O_7. Likewise, they reduced quartz glass samples with hydrogen at 1323 K, which results in 0.2 mass% weight loss by the reduction of SiO_2. It was emphasized that even slight reduction can produce a significant amount of oxygen, since SiO_2 is the most abundant oxide in lunar soil. Based on their results, it was concluded that oxygen in lunar regolith is primarily extracted from FeO, with lesser amounts from TiO_2 and SiO_2.

Separately from the viewpoint of reduced mineral phases, Allen et al. [32,33] focused on the reduction temperature. They reported that lunar soil sintered and melted at temperatures above approximately 1323 K. The melting and agglomeration of particles by sintering significantly reduce the surface area/volume ratio of the sample interacting with hydrogen, which in turn decreases the oxygen production [32,33]. It was also mentioned that an efficient operating temperature for oxygen production should be set below 1323 K to prevent melting and sintering.

As discussed above, the hydrogen reduction process of lunar regolith has been conducted by several research groups [26-33]. Previous studies have reported that the reactivity of mineral phases to iron oxide reduction follows the order of ilmenite > olivine > pyroxene [31-33]. Thus, ilmenite is the most suitable mineral for the hydrogen reduction process. An important issue in the application of the hydrogen reduction process for oxygen production on the Moon is the distribution of ilmenite on the lunar surface. The efficiency of this hydrogen reduction process depends on the ilmenite content of the feedstock. Therefore, this process is particularly suitable for lunar mare and not suitable for highlands. Iron-bearing olivine and pyroxene are more widespread than ilmenite and occupy a larger proportion of rocks and soils [17]. If the reduction of minerals other than ilmenite, such as olivine or pyroxene, is achieved, higher efficiency for the hydrogen reduction process can be expected.

Although the main extraction target from the lunar regolith is oxygen and the metals are regarded as by-product, some of the research on hydrogen reduction of lunar regolith focused

on not only the oxygen production but also the recovery of metal [26]. However, the efficiency of reduction for solid state minerals has been mainly investigated, and little research on the extraction of metal, i.e. the separation of metals from the remaining oxide by smelting, has not been intensively investigated to date. Therefore, from a metallurgical perspective, investigation of the separation and recovery behavior of metals by smelting can provide important information for future lunar metallurgy.

Table 1-8 Chemical compositions (mass%) of lunar samples [31-33].

Oxide	70035	75061	74220
SiO_2	37.84	39.51	38.50
CaO	10.07	10.72	7.40
Al_2O_3	8.85	10.51	5.79
MgO	9.89	9.59	14.90
FeO	18.46	18.02	22.90
TiO_2	12.97	10.38	9.12
Na_2O	0.35	0.35	0.38
Cr_2O_3	0.61	0.48	0.69
MnO	0.28	0.24	n.a.
P_2O_5	0.05	0.06	n.a.
K_2O	0.06	0.08	n.d.

***n.a.**: not analyzed, **n.d.**: not detected.

1.3 Metallurgical Challenges to In-Situ Metal Production on the Moon

As previously introduced, two potential processes are considered for utilization of lunar regolith, which are electrochemical and pyrometallurgical processes. Both processes have the potential to be applied for oxygen evolution and metal recovery, but each has metallurgical limitations that may arise when applied in the lunar environment. In this section, the metallurgical limitations of the two potential processes introduced for lunar metallurgy are discussed.

a. Limitation in Electrochemical Processes: Lack of Electrical Conductivity Information on Lunar Regolith

The MOE process is an electrochemical method that utilizes molten lunar regolith as an electrolyte, making it a promising process for future lunar metallurgy. Molten lunar regolith is considered to be the multicomponent oxide, or slag, and the electrical conductivity of molten slag is critical information in designing and optimizing the MOE process because the electrical conductivity affects the efficiency of electrolysis reactions, energy consumption, and Joule heating. The necessary conductivity data can be obtained through direct experimentation using terrestrial minerals. Several studies on the electrical conductivity of TiO_2-bearing slags have been reported [40-46]. Evseev and Filippov [40] found that increasing TiO_2 content slightly increases the electrical conductivity of the $CaO–Al_2O_3–TiO_2$ system. Shi and Wang [41] reported that in the $CaO–MgO–SiO_2–TiO_2–Al_2O_3$ slag system, the TiO_2 content initially showed little effect on conductivity, but a significant increase was observed beyond approximately 50 mass%TiO_2 [41]. Sato and Sakao [42], as well as Mori [43], discovered that in $CaO–TiO_2–SiO_2$ melts, the electrical conductivity increases with higher TiO_2 content at a fixed basicity, indicating that TiO_2 acts as a network modifier. Conversely, in the $FeO–TiO_2$ system, the addition of TiO_2 initially decreases electrical conductivity, reaching a minimum at approximately 39 mass%TiO_2, followed by a sharp increase with further TiO_2 addition [44]. Shinozaki et al. [45] also found that increased TiO_2 in the $MnO–TiO_2$ system decreases electrical conductivity. Hu et al. [46] reported that high-titania slag ($TiO_2–Ti_2O_3–FeO–CaO–SiO_2–Al_2O_3–MgO$) exhibits semiconductor properties, showing that electrical conductivity increases as TiO_2 content and Ti^{3+}/Ti^{4+} ratio increase.

However, a lack of information on the electrical conductivity of molten slag with respect to

temperature, particularly for multicomponent slags containing TiO_2, in designing and optimizing the MOE process. Lunar regolith typically contains a variety of oxides, as shown in **Table 1-1**, and there is a significant variation of chemical composition as shown in **Table 1-6**. The chemical composition variation on the region of lunar regolith makes it inefficient and time-consuming to obtain all necessary conductivity data only through direct experimentation. Electrical conductivity may be sensitive to slag composition; even small compositional changes can alter the slag structure, leading to abrupt increases or decreases in conductivity [47]. Applying estimation models to calculate electrical conductivity and obtain the desired information is one of the efficient methods. Therefore, various estimation models on electrical conductivity have been developed based on experimentally measured conductivity data [47-50].

Jiao et al. [47] proposed a method of estimating the electrical conductivity of SiO_2–CaO–MgO–MnO system from the chemical composition and temperature by the following equation.

$$k = a + bX_{CaO} + cX_{MgO} + dX_{MnO} \qquad (1-8)$$

where k is the electrical conductivity, X_M is the mole fraction of the oxide (CaO, MgO, MnO) and a is constant ($\Omega^{-1}cm^{-1}$), b, c and d are coefficients ($\Omega^{-1}cm^{-1}$). Here, the values on a, b, c, and d can be determined by multiple linear regression analysis of experimental data, which are applicable only at 1773 K.

Meanwhile, Lambert et al. [48] proposed an estimation model of the electrical conductivity on SiO_2–CaO–MgO–Fe_2O_3 system from the mole fraction of the chemical components at approximately 1673 K as follows.

$$\log k = 0.697 - 2.835F \qquad (1-9)$$

where F is the silica ratio of the mole fraction in SiO_2–CaO–MgO–Fe_2O_3. This equation can be applied to SiO_2–CaO–MgO–Fe_2O_3 slag only at 1673 K.

Zhang et al. [49] proposed estimation of the electrical conductivity of Al_2O_3–CaO–SiO_2–MgO and Al_2O_3–CaO–SiO_2 system using optical basicity. Based on the Arrhenius relationship, the equations derived by Zhang et al. are expressed as follows.

$$\ln k = \ln A - B/(R \cdot T) \qquad (1-10)$$

$$B = \mathrm{m} \cdot \Lambda + \mathrm{n} \qquad (1-11)$$

where A, m, n are constants, which are affected by chemical composition and temperature, B is the activation energy, R is the gas constant, T is the temperature, and Λ is the optical basicity. Zhang's model is more appropriate for estimating the electrical conductivity of molten slag than those of Jiao and Lambert. However, these estimation models can be applied only to the slag systems with a limited number of oxides and are difficult to apply to multicomponent oxides like lunar regolith. In addition, the complex mechanism of electrical conductivity for molten slag systems makes the development of an estimation model difficult [47]. It is known that temperature dependence of electrical conductivity in molten slag is generally positive, and the Arrhenius equation can be used to describe this behavior [51,52].

$$k = A \exp\left(-\frac{E_\mathrm{a}}{RT}\right) \qquad (1-12)$$

where k is electrical conductivity ($\Omega^{-1}\mathrm{cm}^{-1}$), A is the pre-exponential factor, E_a is activation energy ($\mathrm{J \cdot mol^{-1}K^{-1}}$), R is the gas constant (8.314 $\mathrm{J \cdot mol^{-1}K^{-1}}$), and T is the absolute temperature (K). Activation energy (E_a) refers to the energy barrier that ions or electrons must overcome to facilitate their movement. Additionally, when plotting log k against the inverse of temperature ($1/T$), a linear relationship is observed, which is known as an Arrhenius plot [51,52]. Electrical conduction in silicate melts, such as lunar regolith, is associated with the migration of cations and anions through the liquid [53,54]. Thus, the electrical conductivities of silicate melts containing transition metal oxides involve contributions from both ionic and electronic conduction mechanisms [51-55], and can be expressed as follows:

$$k_\mathrm{total} = k_\mathrm{ion} + k_\mathrm{elect} \qquad (1-13)$$

By focusing on the conduction mechanism, although the predominant conduction mechanism for slag is ionic, the electronic conduction can become dominant in the slag with high content

of FeO or MnO. Electronic conduction occurs through the "charge hopping" mechanism, where hopping conduction arises from the transfer of charge between neighboring ions of different valency states [53,54]. In the case of $FeO–Fe_2O_3–SiO_2$ melts, as the temperature increases and thermal excitation occurs, electrons are released; thus, these electrons can jump from Fe^{2+} ions to Fe^{3+} ions [51]. Many transition metal oxide melts have been observed to exhibit relatively high conductance [56], which is attributed to the mechanism of electronic conduction within the melt.

On the other hand, in the case of ionic conduction, there is a big difference in the transference of the cations and the anions in the ionic conduction, the former larger and the latter small, because of the ionic size. Because anions are large polymeric species that tend not to move easily, electrical conductivity is generally related to the movement of existing cations [51]. In general, basic oxides such as CaO, MnO, and MgO are ionized in molten slag, and ionized cations are known to contribute to increasing electrical conductivity [47]. In addition, Zhu et al. [57] reported that the electrical conductivity increases monotonically with increasing R_2O (R=Li, Na, K) content at a fixed CaO/SiO_2 ratio of 1.1 in $CaO–SiO_2–(Al_2O_3)$ melts. On the other hand, the anionic network or complexes formed by the Si, Al, P and Ti oxides prevent the movement of the cations through the melt. This means that the small cations transfer by evading the interference of the network or complex structure, which increases the electrical conductivity for molten slag. Therefore, it is mentioned that the "network-breaking" capacity of the cations is one of the dominant factors for determining the electrical conductivity of molten silicate system. Thus, since electrical conductivity comprises both ionic and electronic conductivity, estimating the overall conductivity of systems that include both is challenging [49]. Therefore, there are significant limitations in developing estimation models for reliable electrical conductivity predictions in multicomponent oxides. From the above aspects, the machine learning like a neural network computation is considered to be one of the potential methods. Haraguchi et al. [58] have applied the neural network computation with respect to the electrical conductivity of molten multicomponent slags, and estimate them reasonably. However, their target systems do not contain TiO_2 which should be considered for regolith simulant, and the neural network computation with deeper layer could achieve the further improvement. The lack of data on the electrical conductivity concerning composition and temperature is a clear limitation in the MOE process. For the future application of the MOE process in lunar

metallurgy, developing new estimation models for electrical conductivity that can well adapt to the variability in the composition and temperature of lunar regolith is necessary.

b. Limitation in Pyrometallurgical Process: Presence of Dispersed Particles in Molten Slag

The hydrogen reduction process allows oxygen and metals (iron) to be obtained from the lunar regolith. To utilize metals on the Moon, it is necessary to consider the separation/recovery of reduced metallic iron from lunar regolith (slag). Typically, when considering the separation/recovery of metals from the remaining oxides, gravity separation of two liquids in high-temperature molten state is an effective method. Such a method is a well-understood and applied high-temperature pyrometallurgical process in various fields of the metallurgical industry on the Earth. Therefore, it is necessary to evaluate the states of metallic Fe and slag based on the thermodynamic evaluation such as phase diagrams to ensure the temperature satisfying the melting of Fe and slag. In addition to the thermodynamic evaluation, the high-temperature physical properties of liquid Fe and molten slag, which are related to the phenomena like fluidity and separation, must be considered.

Additionally, one of the important aspects to consider in this process is the dispersion of metal particles within the molten slag [59-61]. Considering the mean particle size of the lunar regolith (45–100 μm), metallic iron obtained by hydrogen reduction is considered to be smaller. In other words, when the lunar regolith is reduced to a solid state by hydrogen, fine metallic iron particles are dispersed in the lunar regolith, and when melted at high temperatures, it is expected to be dispersed in slag and sedimented by gravity. The presence of dispersed particles in slag can pose significant challenges during metal recovery [59-61]. These particles can hinder the separation process, reduce the efficiency of metal extraction, and lead to lower yields. In this regard, several cases have been reported where particle dispersion is a problem when recovering metals from slag.

He et al. [59] reported that dispersed iron droplets reduce the efficiency of iron recovery from converter slag: thus, in this process, particle coalescence is essential for the efficient recovery of dispersed reduced iron droplets within the molten slag. They also reported that the recovery of metallic iron is directly influenced by the extent of recovery and coalescence of iron droplets in the molten slag, and that the mechanical stirring of the molten slag can facilitate the coalescence of these dispersed particles to enhance the sedimentation efficiency [59]. They

investigated the coalescence mechanism of iron droplets to improve the sedimentation and separation of metallic iron from slag. **Figure 1-3** presents the coalescence mechanism proposed based on their research findings. As shown in **Fig. 1-3**, when iron droplets in a fluid approach each other, deceleration and deformation occur, and a thin film is formed between the droplets. For the droplets to coalesce, drainage of the liquid film must occur, and this drainage is reported to depend on Capillary number (Ca), which is defined as follows [59].

$$Ca = \frac{\mu_l |v_d'|}{\sigma} \qquad (1-14)$$

where μ_l is the liquid-phase viscosity, and v_d' and σ are the relative velocity of droplets and interfacial tension, respectively. Besides, the critical Capillary number (Ca_c) is taken as the critical criterion for droplet coalescence. If $Ca \leq Ca_c$, the droplets will coalesce, otherwise the droplets will not coalesce. When $Ca \leq Ca_c$, the larger the Ca, the slower the liquid film drainage, and the longer the drainage time, and thus, the more difficult the coalescence becomes. Consequently, when the Capillary number between iron particles in the molten slag exceeds a critical value, they coalesce to form large clusters, which facilitates the separation of metal from the slag and leads to an increase in the recovery [59].

Another example of the research on particle dispersion and coalescence can be found in the copper recovery process from pyrometallurgical slag [60]. Similar to the previous case, in this process, dispersed copper particles within the slag settle prior to the solidification, and the size distribution of the copper droplets was reported to exhibit a higher frequency of larger droplets towards the furnace bottom. These findings highlight the importance of droplet size, which influences sedimentation velocity.

Additionally, studies on the interfacial tension between matte and slag have shown that increasing interfacial tension leads to larger droplet sizes [61], indicating the role of interfacial tension in determining droplet size. Natsui et al. [61] have investigated the relationship between the coalescence of droplets dispersed in slag and the interfacial tension. Using smoothed particle hydrodynamics (SPH) method, they studied the transient behavior of molten matte and molten slag, two immiscible liquids with high interfacial tension. Their results demonstrated that coalescence occurs more rapidly with increasing interfacial tension, revealing that droplet size and coalescence rate are governed by interfacial tension. Notably, in the case of a multiple-

droplet system, variations in interfacial tension were observed to influence the curvature of the interface formed between the matte and slag phases. This suggests that when interfacial tension decreases, droplets exhibit a tendency to disperse, while conversely, when interfacial tension increases, droplets exhibit a tendency to coalesce. This implies that interfacial tension serves as a key factor in determining not only droplet size but also the coalescence mechanism, thereby exerting a significant impact on recovery efficiency.

These cases occurring in these various processes underscore the importance of particle coalescence in metallurgical recovery processes, and the significantly lower gravity of the lunar environment presents potential issues that could affect the efficiency of these processes. Considering the lower gravity of the Moon compared to that of the Earth, these particles are more likely to disperse and may not settle as quickly or effectively as under Earth's gravitational conditions. Such dispersion and the resultant behavior of metallic particles play a pivotal role in understanding the efficiency of metal recovery during reduced lunar gravity. Therefore, it is necessary to re-evaluate and potentially adapt these processes for the lunar environment.

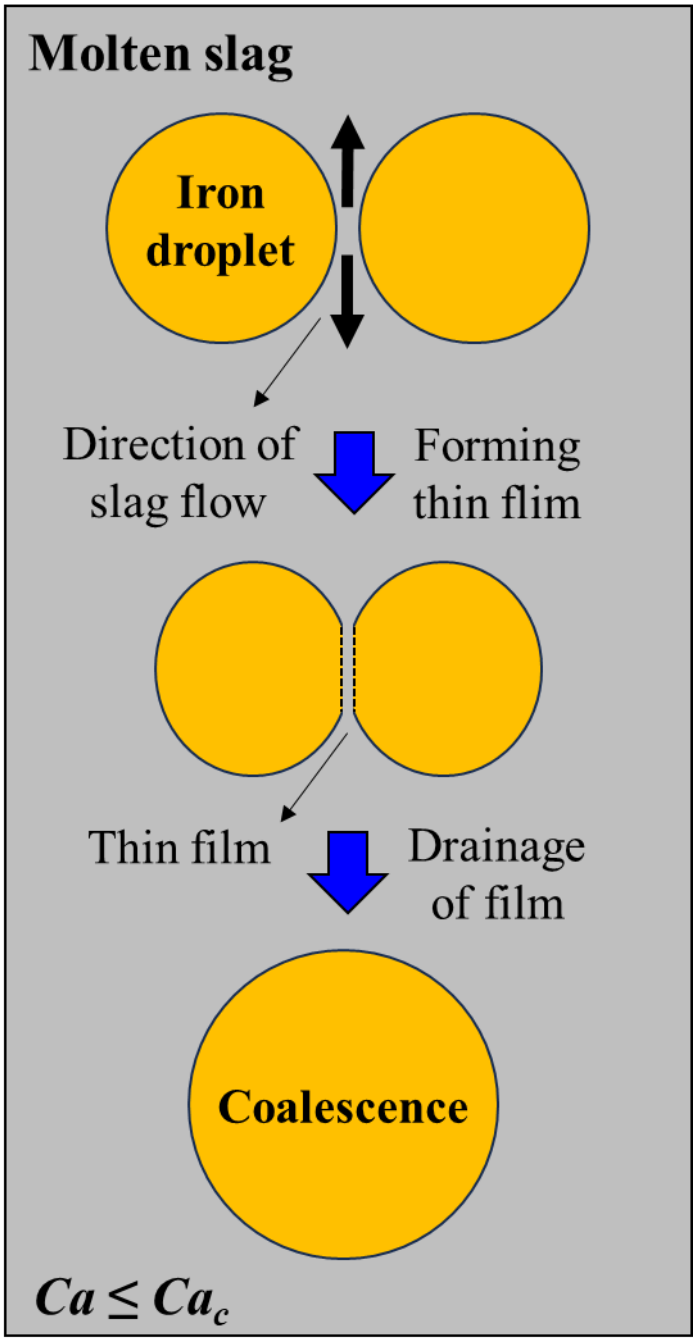

Fig. 1-3 Schematic of coalescence after collision between two droplets [59].

1.4 Objective

This dissertation discusses the potential processes and metallurgical methods for the realization of "Lunar Metallurgy" to recover valuable metal resources from the lunar regolith. In order to utilize valuable metal resources from the lunar regolith, (1) neural network computations were applied to estimate the electrical conductivity of lunar regolith (multicomponent oxides). Additionally, (2) a pyrometallurgical process using hydrogen was designed, and various physical and chemical properties of this process were investigated.

In Chapter 2, neural network computations were applied to estimate the electrical conductivity of variable lunar regolith compositions, and a predictive model for electrical conductivity was developed to respond to the regional variability in lunar regolith composition. Based on the developed model, the changes in electrical conductivity were estimated according to the concentration change of seven major oxides (SiO_2, CaO, Al_2O_3, MgO, FeO, TiO_2, Na_2O) in lunar regolith. Specifically, this chapter focused on the changes in electrical conductivity by the addition of oxides to multicomponent slags containing titanium, particularly targeting regolith from the mare region. The validity of these estimations was discussed from the perspectives of the basicity and the structure of the molten slag.

In Chapter 3, the effect of wettability on the coalescence of liquid droplets within another immiscible solution was investigated. For the experiments, two immiscible liquids, liquid paraffin, and 89 mass% glycerin aqueous solution, were used to first observe the wetting behaviors of each droplet on the surface of the other, based on the difference in surface tension. Coalescence experiments were then performed, followed by a discussion on the mechanism of droplet coalescence of one liquid in another liquid from the perspective of wettability.

In Chapter 4, a reduction process for lunar regolith simulant using hydrogen was designed based on thermodynamic predictions, and experiments were conducted in two steps: reduction and melting processes. By comparing the thermodynamic predictions with experimental results, differences from equilibrium conditions were investigated. Based on the investigation of the behavior occurring in each step of the process, a mechanism for the reduction and melting processes of regolith simulant was proposed.

In Chapter 5, the variations in recovery on the addition of various oxides to lunar regolith simulant were observed, and the causes of recovery variations were investigated in terms of viscosity and wettability. Wettability was evaluated using contact angles calculated based on Neumann's relation, confirming the influence of wettability on coalescence of liquid Fe particles.

Chapter 6 summarizes the results from chapters 2 to 5. This chapter briefly discusses the potential applications of lunar metallurgy and outlines future prospects for process development and improvement.

REFERENCES

[1] G. H. Heiken, D. T. Vaniman, and B. M. French: Lunar Source book, Cambridge University Press, New York, (1991), 1, 6, 27, 61, 121, 183, 285.

[2] J. F. Lindsay: Lunar Stratigraphy and Sedimentology, Elsevier Scientific Publishing Company, New York, (1976), 119, 227.

[3] S. Li, P. G. Lucey, R. E. Milliken, P. O. Hayne, E. Fisher, J. P. Williams, D. M. Hurley and R. C. Elphic: Proc. Natl. Acad. Sci. USA, 115 (2018), 8907.

[4] D. B. Stoeser, D. L. Rickman and S. Wilson: Design and Specifications for the Highland Regolith Prototype Simulants NU-LHT-1M and -2M, (NASA/Technical Memorandum), (2010), https://ntrs.nasa.gov/citations/20110008071, (accessed 2024-05-28).

[5] K. Wohletz and G. Heiken: Volcanology and Geothermal Energy, University of California Press, Berkeley, (1992), 338.

[6] CLASS Exolith Lab., https://sciences.ucf.edu/class/simulant_lunarmare, (accessed 2024-05-28).

[7] CLASS Exolith Lab., https://sciences.ucf.edu/class/simulant_lunarhighlands, (accessed 2024-05-28).

[8] T. Isawa: Proc. 3rd Int. Slag Valorisation Symp. on The Transition to Sustainable Materials Management, SVS 2013, Taylor & Francis, U. K, (2013), 87.

[9] D. R. Williams: Moon Fact Sheet, https://nssdc.gsfc.nasa.gov/planetary/factsheet/moonfact.html, (accessed 2024-05-28).

[10] S. S. Schreiner, J. A. Hoffman, G. B. Sanders, K. A. Lee: IEEE Aerospace Conference, (2015), 1.

[11] G. B. Sanders and W. E. Larson: Journal of Aerospace Engineering, 26 (2013), 5.

[12] L. Schlüter and A. Cowley: Planetary and Space Science, 181 (2020), 104753.

[13] A. H. C. Sirk, D. R. Sadoway and L. Sibille: ECS Trans., 28 (2010), 367.

[14] D. Wang, A. J. Gmitter and D. R. Sadoway: J. Electrochem. Soc., 158 (2011), E51.

[15] H. Kim, J. Paramore, A. Allanore and D. R. Sadoway: J. Electrochem. Soc., 158 (2011), E101.

[16] P. A. Curreri, E. C. Ethridge, S. B. Hudson, T. Y. Miller, R. N. Grugel, S. Sen and D. R. Sadoway: Process Demonstration For Lunar In Situ Resource Utilization-Molten Oxide

Electrolysis (MSFC Independent Research and Development Project No. 5-81), (NASA/Technical Memorandum), (2006), https://ntrs.nasa.gov/citations/20070018263, (accessed 2024-05-28).
[17] K. Ramohalli and J. Lewis: NASA Space Engineering Research Center for utilization of local planetary resources, (NASA/Collected Works), (1992), https://ntrs.nasa.gov/citations/19930017485, (accessed 2024-05-28).
[18] C. Schwandt, J. A. Hamilton, D. J. Fray and I. A. Crawford: Planetary and Space Science, 74 (2012), 49.
[19] E. Standish, D. Stefanescu and P. Curreri: 47th AIAA Aerospace Sciences Meeting including The New Horizons Forum and Aerospace Exposition, (2009), 1657.
[20] L. Sibille, D. R. Sadoway, P. Tripathy, E. Standish, A. Sirk, O. Melendez and D. M. Stefanescu: 48th AIAA Aerospace Sciences Meeting Including the New Horizons Forum and Aerospace Exposition, (2010), 367.
[21] S. Schreiner, L. Sibille, J. A. Dominguez, J. A. Hoffman, G. B. Sanders and A. H. Sirk: 8th Symposium on Space Resource Utilization, (2015), 1180.
[22] A. Shchetkovskiy, T. McKechnie, D. R. Sadoway, J. Paramore, O. Melendez and P. A. Curreri: Earth and Space 2010 (Engineering, Science, Construction, and Operations in Challenging Environments), (2010), 1039.
[23] M. Esmaily, A. N. Mortazavi, N. Birbilis and A. Allanore: Scientific Reports, 10 (2020), 14833.
[24] K. Yu, J. Stokes, B. Harder, L. Reidy and K. T. Faber: Journal of the American Ceramic Society, (2024), 1.
[25] S. D. Rosenberg, O. Musbah and E. E. Rice: Lunar Planet Sci., (1996), 1105.
[26] A. Radl, K. M. Neumann, H. Wotruba, E. Clausen and B. Friedrich: CEAS Space Journal, 15 (2023), 585.
[27] U. Hegde, R. Balasubramaniam and S. Gokoglu: Development and Validation of a Model for Hydrogen Reduction of JSC-1A, (NASA/Technical Memorandum), (2009), https://ntrs.nasa.gov/citations/20090023167, (accessed 2024-05-28).
[28] U. Hegde, R. Balasubramaniam, S. Gokoglu, K. Rogers, M. Reddington and L. Oryshchyn: Hydrogen Reduction of Lunar Regolith Simulants for Oxygen Production, (NASA/Technical Memorandum), (2011), https://ntrs.nasa.gov/citations/20110008071, (accessed 2024-05-28).

[29] H. M. Sargeant, F. A. J. Abernethy, M. Anand, S. J. Barber, P. Landsberg, S. Sheridan, I. Wright and A. Morse: Planetary and Space Science, 180 (2020), 104759.
[30] H. M. Sargeant, S. J. Barber, M. Anand, F. A. J. Abernethy, S. Sheridan, I.P. Wright and A.D Morse: Planetary and Space Science, 205 (2021), 105287.
[31] M. A. Gibson, C. W. Knudsen, D. J. Brueneman, C. C. Allen, H. Kanamori and D. S. McKay: Journal of Geophysical Research (Planets), 99 (1994), 10887.
[32] C. C. Allen, R. V. Morris and D. S. McKay: Journal of Geophysical Research (Planets), 99 (1994), 23173.
[33] C. C. Allen, R. V. Morris and D. S. McKay: Journal of Geophysical Research (Planets), 101 (1996), 26085.
[34] J. J. Papike, A. E. Bence and D. H. Lindsley: Lunar Science Conference, 5th, Houston, Tex., March 18-22, Proceedings. (A75-39540 19-91) New York, Pergamon Press, Inc., 1 (1974), 471.
[35] G. M. Brown, A. Peckett, C. H. Emeleus, R. Phillips and R. H. Pinsent: Lunar Science Conference, 6th, Houston, Tex., March 17-21, Proceedings. (A78-46603 21-91) New York, Pergamon Press, Inc., 1 (1975), 1.
[36] G. Ostberg: Jernkontorets Annaler, 144 (1960), 46.
[37] Y. Zhao and F. Shadman: Industrial & engineering chemistry research, 30 (1991), 2080.
[38] G. Heiken and D. S. McKay: Lunar Science Conference, 5th, Houston, Tex., March 18-22, Proceedings. (A75-39540 19-91) New York, Pergamon Press, Inc., 5 (1974), 843.
[39] E. W. Wolfe, N. G. Bailey, B. K. Lucchitta, W. R. Muehlberger, D. H. Scott, R. L. Sutton, H. G. Wilshire, R. M. Batson, K. B. Larson and R.L. Tyner: The geologic investigation of the Taurus-Littrow valley, Apollo 17 landing site, (Washington: US Govt. Print. Off. 1981).
[40] P. Evseev and A. Filippov: Izv. Vyssh. Uchebn. Zaved. Chern. Met., (1967), 55.
[41] H. Y. Shi and J. C. Wang: Iron Steel Vanadium Titan., (1987), 56.
[42] H. Sato and F. Sakao: Electrochemistry, 26 (1958), 560.
[43] K. Mori: Tetsu-to-Hagané, 46 (1960), 34.
[44] K. Mori and Y. Matsushita: Tetsu-to-Hagané, 42 (1956), 1024.
[45] N. Shinozaki, K. Mizoguchi, and Y. Suginohara: J. Jpn. Inst. Met., 42 (1978), 162.
[46] K. Hu, X.W Lv, Z.M. Yan, W. Lv and S.P. Li: Metall. Mater. Trans. B, 50 (2019), 2982.
[47] Q. Jiao and N. J. Themelis: Metall. Trans. B, 19 (1988), 133.

[48] J. Lambert Bates: Proc. Conf. on High Temperature Sciences Related to Open-cycle, Coal-fired MHD Systems, U. S. Energy Research and Development Administration, Washington, D.C., (1977), 196.
[49] G. H. Zhang and K. C. Chou: Metall. Mater. Trans. B, 41 (2010), 131.
[50] G. H. Zhang and K. C. Chou: Metall. Mater. Trans. B, 43 (2012), 849.
[51] K. C. Mills, M. Hayashi, L. Wang and T. Watanabe: Treatise on process metallurgy, 1 (2014), 149.
[52] K. C. Mills and B. J. Keene: Int. Materials Rev., 32 (1987), 1.
[53] T. Yoshino: Surveys in Geophysics, 31 (2010), 163.
[54] T. Yoshino: Magmas Under Pressure, (2018), 281.
[55] J. H. Liu, G. H. Zhang, Y. D. Wu and K. C. Chou: Metal. and Mater. Trans. B, 47 (2016), 798.
[56] M. Barati and K. S. Coley: Metal. and Mater. Trans. B, 37 (2006), 41.
[57] J. H. Zhu, Y. Hou, W. W Zheng, G. H. Zhang, K. C. Chou: ISIJ Int., 59 (2019), 1947.
[58] Y. Haraguchi, M. Nakamoto, M. Suzuki, K. Fuji-ta and T. Tanaka: ISIJ Int., 58 (2018), 1007.
[59] M. He, N. Wang, Q. How, M. Chen and H. Yu: Powder Technol., 362 (2020), 550.
[60] J. Isaksson, A. Andersson, T. Vikström, A. Lennartsson and C. Samuelsson: Journal of Sustainable Metallurgy, 9 (2023), 1378.
[61] S. Natsui, R. Nashimoto, T. Kumagai, T. Kikuchi and R. O. Suzuki: Metal. and Mater. Trans. B, 48 (2017), 1792.

Chapter 2

Neural Network Modeling of Multicomponent Oxides for Estimation of Electrical Conductivity of Lunar Regolith

2.1 Background

The electrical conductivity of molten slag is an important physical property in the design and optimization of system operation of metallurgical processes such as electric smelting furnaces and MOE processes [1]. This knowledge supports the design of new processes for resource utilization on the Earth and potentially other celestial bodies.

The lunar surface, primarily the dark "Mare" and the bright "Highland" regions, is composed of silicate minerals similar to Earth's volcanic rocks. The composition of the mare regions, particularly the ilmenite-rich basalts, is especially conducive to the extraction of metals such as Fe and Ti [2,3]. Some research suggests electrolysis processes to extract these metals and oxygen from lunar regolith [4-15]. The electrolysis process is the most widely used process for high-yield oxygen production, where electricity is applied to decompose regolith into oxygen at the anode and into metals at the cathode [6]. In the field of lunar regolith utilization, both the Fray-Farthing-Chen (FFC) Cambridge process and the molten oxide electrolysis (MOE) process have been studied for a potential application [6,12]. Among these processes, the MOE process involves using lunar regolith as the electrolyte, which melts at high temperatures to produce oxygen and metals without the need for additional electrolytes [6,12]. The composition of lunar regolith varies significantly depending on the location, with the mare regions known to exhibit substantial variations in ilmenite concentration [2,3]. This suggests that the effect of TiO_2 on electrical conductivity can vary greatly depending on the composition change in the mare regions [16]. Direct measurement of electrical conductivity over a wide range in order to respond to changes in the composition of lunar regolith is time-consuming, which makes it inefficient. The application of estimation models to obtain electrical conductivity information is a more efficient approach. In addition, various estimation models have been developed based on experimental information on electrical conductivity [17-20]. However, existing electrical

conductivity estimation models can only be applied to specific compositions and are difficult to apply to multicomponent oxides such as lunar regolith. Therefore, a new estimation model for the electrical conductivity of multicomponent oxides needs to be developed for lunar regolith utilization.

Recently, neural network (NN) computation has been efficiently applied to identify universal correlations among various factors [21-26]. Haraguchi et al. [24] reproduced the electrical conductivity in eight-component systems comprising SiO_2, CaO, MgO, MnO, Al_2O_3, FeO, Fe_2O_3, and Na_2O by conducting a neural network computation with SlagVis [23] software, which provides a single-layer model with one hidden (middle) layer. However, Haraguchi et al.'s model is difficult to apply to estimate electrical conductivity in the lunar mare region because the TiO_2 component is not included in the calculation.

Therefore, in this chapter, a neural network prediction model was developed to estimate the electrical conductivity of multicomponent oxides such as lunar mare regolith. A multilayer neural network was applied for more accurate predictions compared to the single-layer model. In neural network modeling, the electrical conductivity data collected from the literature were used as training data in the learning process, and Bayesian optimization was utilized for hyperparameter optimization. Using the developed model, the changes in electrical conductivity of lunar mare regolith in response to changes in composition were estimated.

2.2 Procedure

2.2.1 Structure of Neural Network Computation

Artificial neural networks are a set of algorithms created by imitating the operating principles of neurons, the nerve cells in the brain, and are used to process and learn from data. A neural network operation receives multiple input signals, multiplies each signal by a weight, and then applies an activation function to the sum to produce an output value. In particular, multilayer neural networks allow complex problems to be solved because these operations are repeated through multiple layers [25,26]. **Figure 2-1** shows the structure of the hierarchical neural network, which was used in this study as a model for nonlinear regression of a specific physical quantity (y) from multiple variables (x_i). The neural network used in this study consists of the input layer, the hidden layer, and the output layer. When numerical values are input to the input

layer, these values propagate through the hidden layer to the output layer to generate an output value. The error is calculated by comparing the output value with training data, and parameters are updated to the minimize the error. The method of updating parameters is determined by an optimization algorithm, such as Stochastic Gradient Descent (SGD) [27]. In this work, regression calculations of neural networks were performed using Adaptive Moment Estimation (ADAM) [28], which has recently been reported to achieve high-precision optimization. ADAM is an optimization algorithm that is widely used in deep learning. This method integrates the advantages of AdaGrad to deal with sparse gradients with the capabilities of RMSProp for handling non-stationary objectives, potentially leading to improvements in learning speed and accuracy [28]. In addition, the root-mean-square error (RMSE) given by Eq. (2-1) was used as the error metric.

$$\mathrm{RMSE} = \sqrt{\sum_{i=1}^{N} \frac{(y-t)^2}{N}} \qquad (2-1)$$

Here, N is the number of samples, y represents the values predicted by the neural network, and t represents the target values from the training data. The rectified linear unit (ReLU) function, given by Eq. (2-2), was used as the activation function.

$$\text{ReLU function} : f(x) = max\{0, \mathrm{x}\} \qquad (2-2)$$

L2 regularization was used to suppress overfitting [29]. L2 regularization aims to minimize the objective function L, which includes the RMSE and the sum of squares of all weights w_{ij} in the network. The objective function L is expressed in Eq. (2-3). In this study, λ=0.001 [26], where λ is a coefficient that determines the strength of the regularization.

$$L = \mathrm{RMSE} + \sum_{i,j=1}^{n} w_{ij}^2 \qquad (2-3)$$

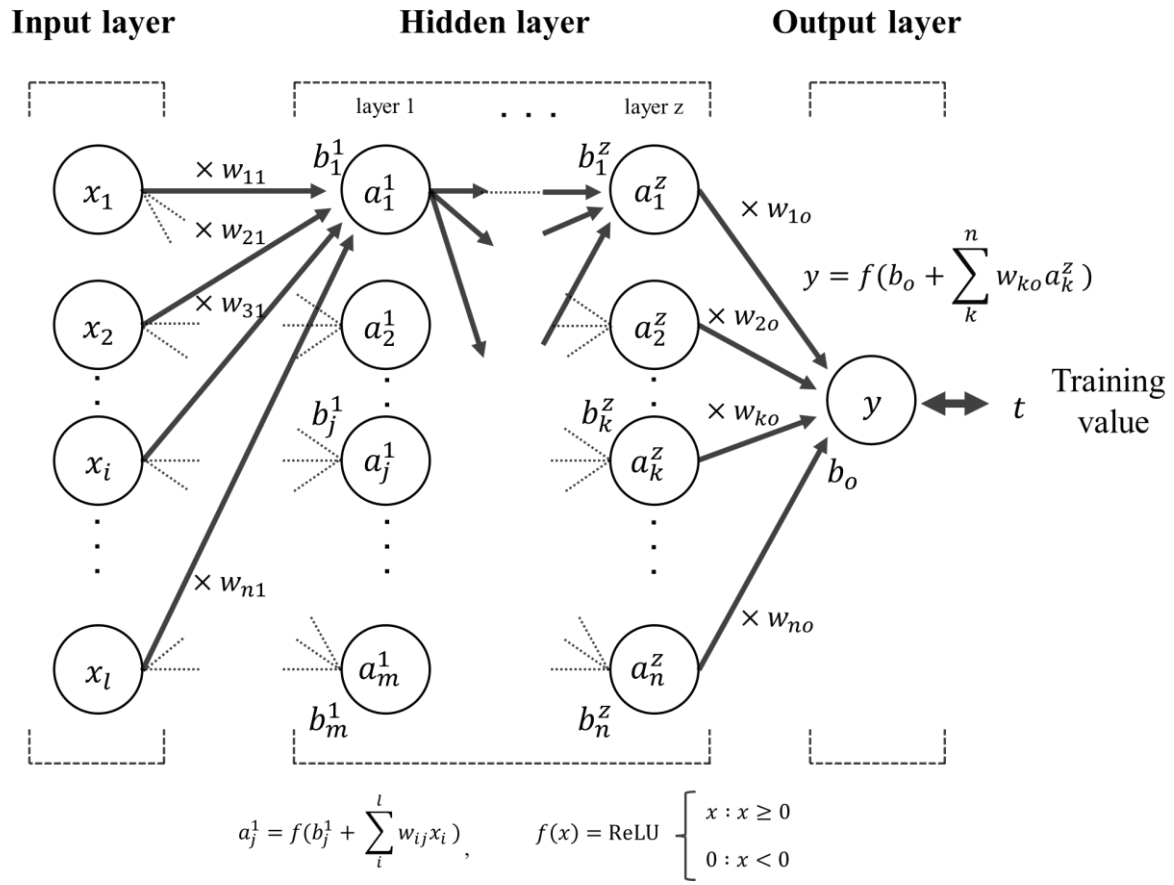

Fig. 2-1 Schematic diagram of hierarchical neural network used in neural network computation.

2.2.2 Data Selection

The total number of literature data items [30-61] used in this study is 2803, as shown in **Table 2-1**. The collected literature data were limited to compositional systems containing SiO_2 as the main component. It is generally known that the inherent error in the measured values for electrical conductivity is about 30% due to the experimental conditions [62]. The 2243 data items, which accounted for about 80% of the total data items, were randomly selected as training data, and 560 data items of the remaining 20% were selected as test data to evaluate the validity of the learning result. **Table 2-2** shows the distribution of the data in **Table 2-1** before normalization. The data in **Table 2-2** are converted to values between 0 and 1 using normalization by Eq. (2-4) in the preprocessing step of neural network analysis.

$$z' = \frac{z - z_{min}}{z_{max} - z_{min}} \qquad (2-4)$$

Here, z and z' represent the input and output values before and after normalization, respectively, while z_{max} and z_{min} are the maximum and minimum values of z.

Table 2-1 Literature data used to estimate the electrical conductivity of molten slag.

System	Temperature (K)	Ref.
SiO_2–CaO, SiO_2–MgO, SiO_2–FeO, SiO_2–Na_2O	1372–2051	30–34, 43–45, 50, 61
SiO_2–MgO–CaO	1623	35, 36
SiO_2–MgO–Al_2O_3	1773–2073	37, 38
SiO_2–CaO–Al_2O_3	1773–1923	39, 40, 58
SiO_2–FeO–CaO	1573–1773	46, 47, 61
SiO_2–FeO–MgO	1573–1673	48
SiO_2–Na_2O–MgO	1623	35
SiO_2–Na_2O–CaO	1033–1662	59
SiO_2–Na_2O–FeO	1405–1542	51, 61
SiO_2–TiO_2–FeO	1573	48
SiO_2–TiO_2–Na_2O	1523–1823	52, 53
SiO_2–TiO_2–CaO	1453–1873	54–57, 61
SiO_2–MgO–CaO–Al_2O_3	1515–1893	34, 41, 60, 61
SiO_2–FeO–CaO–Al_2O_3	1250–1776	49, 61
SiO_2–TiO_2–Al_2O_3–Na_2O	1624–1863	53
SiO_2–TiO_2–Al_2O_3–CaO	1565–1873	58, 61
SiO_2–FeO–CaO–Al_2O_3–MgO	1673–1873	42

Table 2-2 Distribution of collected data before normalization.

Parameter	Maximum	Minimum	Mean	Standard deviation
SiO_2 (mass%)	88.8	0.5	43.7	12.8
CaO (mass%)	60.0	0	19.2	19.1
Al_2O_3 (mass%)	50.3	0	9.1	11.7
MgO (mass%)	59.5	0	9.5	14.6
FeO (mass%)	75.4	0	5.6	16.2
TiO_2 (mass%)	54.1	0	7.3	13.6
Na_2O (mass%)	87.5	0	5.6	14.3
Temperature (K)	2073	1033	1723	181

2.2.3 Determination of Parameters

When building a neural network, certain parameters need to be pre-tuned and remain unchanged during the learning process. These parameters are called hyperparameters. In this study, the number of hidden layers and the number of units in each hidden layer are designated as hyperparameters. The values of the hyperparameters determine the accuracy of the model. In this study, mini-batch learning was used in the learning process. Mini-batch learning is a method in which the training data are divided into smaller subsets called batches. The number of training samples used in one batch is called batch size, which is also a hyperparameter. In this study, hyperparameters were determined using Bayesian optimization [63]. In hierarchical neural networks, the number of hidden layers is known to have a substantial effect on estimation. Therefore, Bayesian optimization was performed for each of the 1 to 10 different hidden layers, and regression calculations were carried out under the optimal conditions where a hidden layer with a minimum value was identified by the objective function. The parameter search ranges were as follows: the number of the hidden layers (1–10), the number of units in the hidden layers (1–50), the number of epochs (1–100000), and batch size (30–300). Expected Improvement (EI) was used as the acquisition function in this study [25,26]. Other than selecting EI as the acquisition function, the optimization was performed using the default settings of the library.

2.2.4 Estimation of Electrical Conductivity of Lunar Mare Regolith

With the network obtained from Bayesian optimization, the electrical conductivity of multicomponent oxides was investigated for different composition and temperature conditions. The mean composition of the lunar mare regolith [3] was used as a reference composition to predict the electrical conductivity of multicomponent oxides. **Table 2-3** gives the mean composition of lunar mare regolith used in the estimation of electrical conductivity, representing the mean result from the eight mare sites on the Moon [3,64]. Based on the composition shown in **Table 2-3**, the change in electrical conductivity was calculated when 1 to 5 mol% of each component was added to the reference composition. The electrical conductivity was estimated at 50 K intervals in the temperature range from 1773 K to 1923 K. The temperature ranges of calculation include the temperature range of literature data collected, indicating that the data within this range are reliable, and the predictions should be accurate.

Table 2-3 Mean composition of lunar mare regolith applied to neural network computation [3,64].

Oxide	SiO_2	CaO	Al_2O_3	MgO	FeO	TiO_2	Na_2O
mass%	45.4	11.8	14.9	9.2	14.1	3.9	0.6

2.3 Results and Discussion

2.3.1 Neural Network Modeling by Bayesian Optimization

Table 2-4 presents the parameter values obtained by Bayesian optimization aimed at minimizing the objective function *L*. The objective function *L* is a function used to evaluate the performance of the model in neural network learning. The performance of the model means the balance of reproducibility and predictiveness. The objective function *L* contains RMSE, which indicates the error, and the sum of squares of all weights in the network, as shown in Eq. (2-3). The sum of squares of all weights means that the objective function *L* increases when the number of layer and unit increase. Therefore, the minimum value of the objective function *L* represents the error is low (high reproducibility) and the number of variables is small (high predictive accuracy), which could satisfy the optimization of the parameters. With the number of hidden layers, the value of the objective function *L* progressively decreases, achieving its minimum value (0.06862) at eight hidden layers as shown in **Table 2-4**. The minimum value of the objective function *L* means the minimum difference between the predicted value and the actual value. Thus, the number of hidden layers, which is the prediction model parameter in this study, was determined to be eight.

Figure 2-2 shows the objective function *L* and RMSE for test data across epochs when the training data are processed through the neural network with the above parameters. In this process, the objective function *L* was used for training. In addition, the RMSE of test data was calculated only for the performance evaluation of the model during the learning process. The objective function *L* and RMSE converge to constant values after a significant decrease at the beginning of learning, indicating that overfitting is minimized with the selected parameters and appropriate learning has been achieved.

Figure 2-3 shows the comparison between the experimental and calculated values for the training data (2243 data items) to evaluate the accuracy of the predictive model. The x-axis presents the experimental values derived from the literature, which have been normalized to a range of 0 to 1 according to Eq. (2-4). The y-axis represents the calculated value obtained from the neural network computation, which was calculated to a value corresponding to the normalized values on the x-axis. Consequently, both the x-axis and y-axis are dimensionless. The accuracy of the predictive model is evaluated by comparing the calculated values with the

experimental values. Specifically, the closer the slope of the line is to 1, the higher the accuracy of the predictive model. The dotted lines indicate the range of the difference between the experimental and calculated values. Most of the data fall within an error range of 30%, with a coefficient of determination (R^2) of 0.9302, demonstrating a highly linear relationship. This indicates that the calculated values obtained from neural network computation accurately reproduce the experimental values for training data. The experimental values measured by various groups in actual experiments had an error of up to approximately 30% [62]. Therefore, the error range of the calculation values is considered reasonable.

Figure 2-4 shows the comparison between the experimental and calculated values for test data (560 data items) to evaluate the validity of the estimation results from the training data. The coefficient of determination (R^2) was 0.9068, indicating that the predictive model effectively reproduces the experimental values for the unknown data. The results in **Figs. 2-3** and **2-4** suggest that the electrical conductivity of slag can be accurately predicted using a neural network.

Table 2-4 Results of Bayesian optimization for the parameters, the number of units in hidden layers, epochs, and batch sizes.

Number of hidden layers	Number of units in each layer										Batch size	Epochs	Objective function L
	1st	2nd	3rd	4th	5th	6th	7th	8th	9th	10th			
1	35	-	-	-	-	-	-	-	-	-	49	74666	0.10250
2	50	48	-	-	-	-	-	-	-	-	147	69172	0.08613
3	40	29	16	-	-	-	-	-	-	-	114	21152	0.07813
4	42	40	2	47	-	-	-	-	-	-	290	72505	0.07189
5	49	20	50	42	29	-	-	-	-	-	232	97409	0.07066
6	41	46	34	32	24	41	-	-	-	-	177	90432	0.07005
7	38	47	34	13	37	20	50	-	-	-	147	62063	0.07038
8	50	39	33	11	37	10	6	34	-	-	206	39254	0.06862
9	42	25	25	33	39	19	6	39	40	-	274	83520	0.06935
10	38	46	22	5	40	35	13	27	43	45	132	10162	0.07411

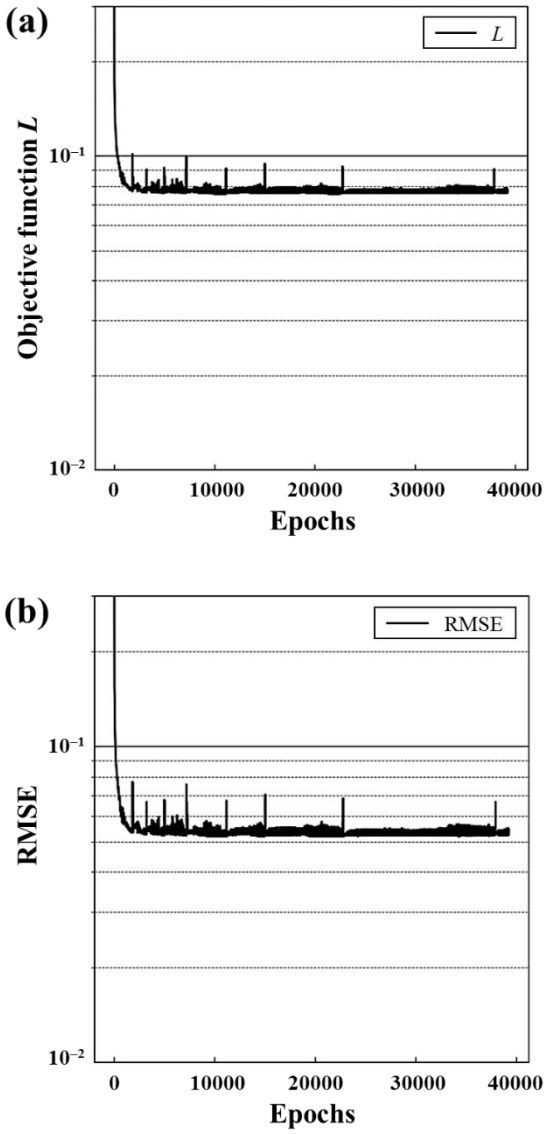

Fig. 2-2 Learning curves with the number of learning iterations (epochs): (a) The objective function *L* including both RMSE of training data and the L2 regularization term, and (b) RMSE of test data.

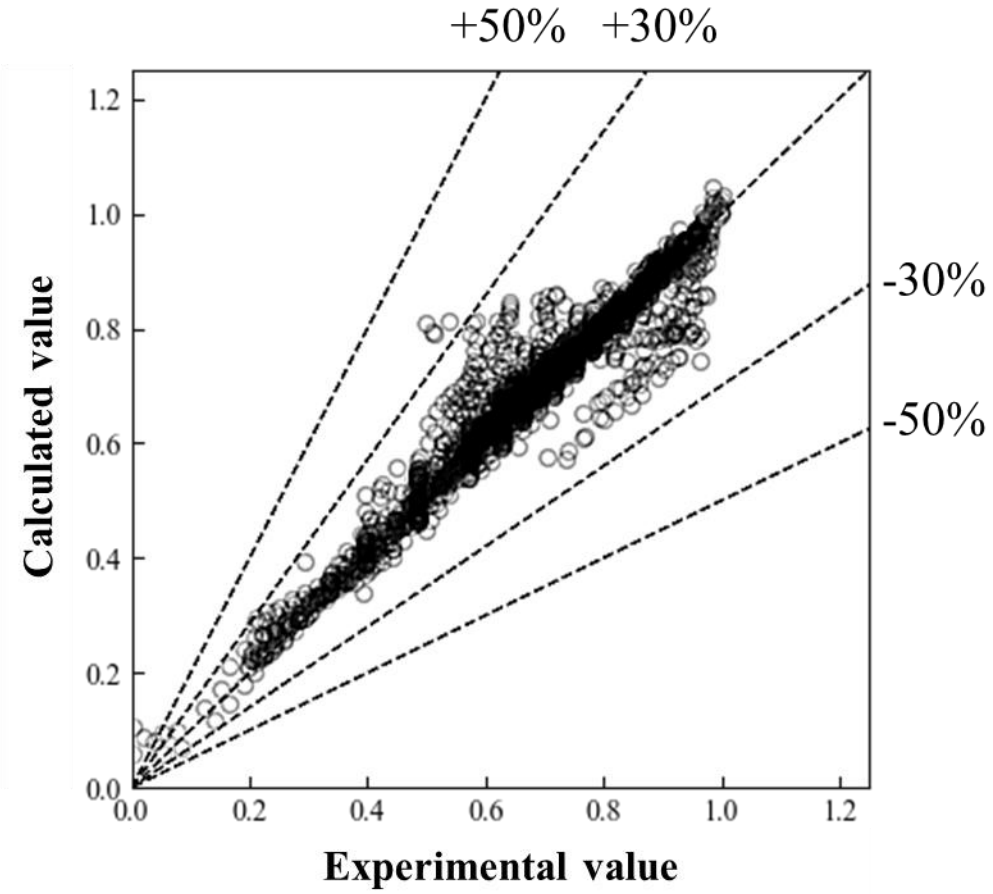

Fig. 2-3 Comparison of experimental and calculated values of electrical conductivity obtained by neural network computation using training data.

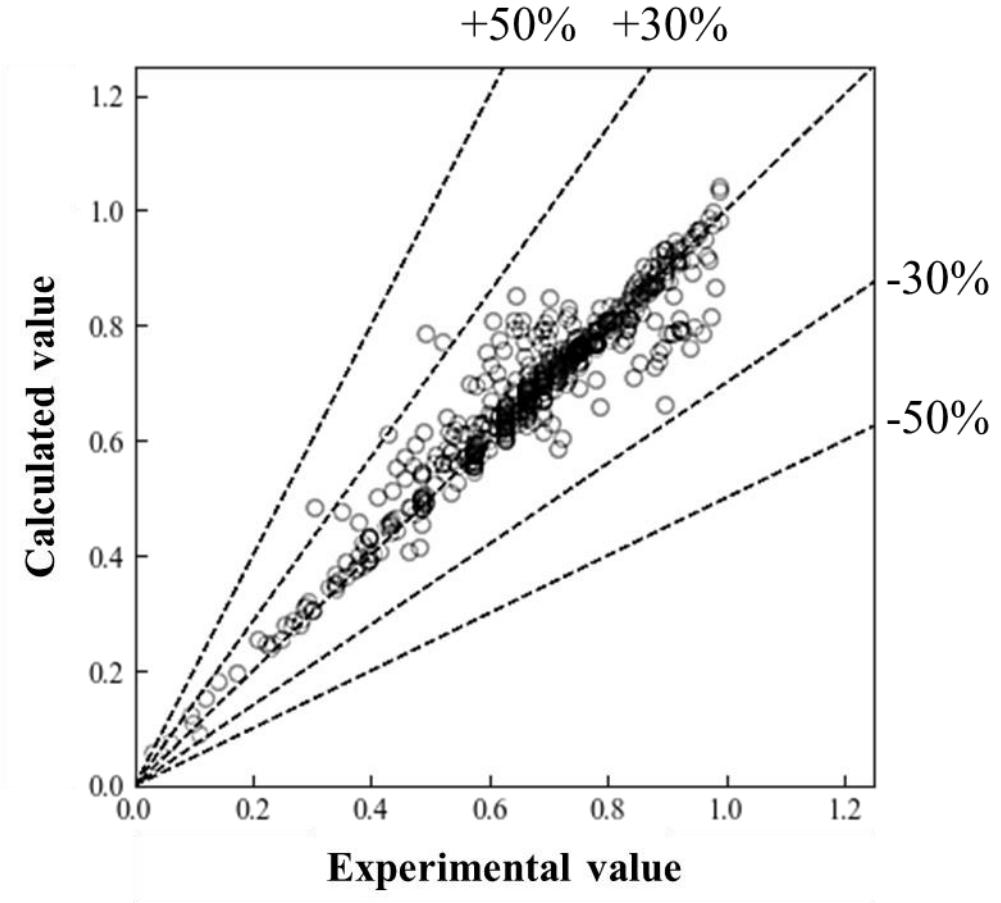

Fig. 2-4 Comparison of experimental and calculated values of electrical conductivity obtained by neural network computation using test data.

2.3.2 Estimation of Change in Electrical Conductivity of Lunar Mare Regolith with Addition of Oxides

Figure 2-5 shows the change in electrical conductivity when different oxides are added to lunar mare regolith, within the temperature range of 1773 K to 1923 K, as estimated by the Bayesian optimization model. In all temperature ranges, electrical conductivity increased linearly with the addition of Na_2O, CaO, FeO, and MgO, while SiO_2 decreased as shown in **Fig. 2-5**. The contribution to the increase in electrical conductivity due to the addition of oxides was in the following order: Na_2O > CaO > FeO > MgO. Al_2O_3 and TiO_2 have different contributions to electrical conductivity depending on slag composition and temperature. In the case of Al_2O_3, electrical conductivity both decreased and increased depending on composition and temperature. In particular, the change in electrical conductivity decreased as the temperature increased, remaining generally constant at 1873 K, and decreasing at 1923 K. TiO_2 generally increases electrical conductivity depending on the amount added, but as the temperature increases, its effect on changes in electrical conductivity decreases. The magnitude of the contribution to the electrical conductivity by the addition of such oxide components depends on the magnitude of the attractive force acting between the cation and oxygen ion. The magnitude (I) of the attraction between the cation and oxygen ion is expressed as follows.

$$I = \frac{2Z_i}{(R_c + R_a)^2} \qquad (2-5)$$

Here, Z_i is the valency of cation in component i, and R_c and R_a are the radii of the cation and oxygen ion, respectively. The larger I value, the more difficult it is for the oxide to break the bond with the oxygen ion, that is, to become a cation. Typically, oxides can be classified as acidic, basic, or intermediate oxides based on the magnitude of I value. **Table 2-5** shows ion-oxygen parameters for oxides. Here, Na_2O, CaO, FeO, and MgO are classified as basic oxides, TiO_2, Al_2O_3 are classified as intermediate oxides, and SiO_2 is classified as acidic oxides [65].

Figure 2-6 shows the difference in electrical conductivity between the reference composition and the addition of +5 mol% of each oxide, based on the value of I. As shown in **Fig. 2-6**, the basic oxides generally contribute to an increase in electrical conductivity, with a smaller value of I corresponding to a greater increase in electrical conductivity. Basic oxides

can break bonds to the oxygen ions and form cations, increasing the number of charge carriers. In addition, the free oxygen ion (O^{2-}) dissociated from a basic oxide reacts with bridging oxygen (O^0) covalently bonded to two Si atoms in the form of Si–O–Si, converting it into non-bridging oxygen (O^-) and forming a Si–O bond [66-68]. **Figure 2-7** shows that complex silicate anions become simpler anions through reaction with a free oxygen ion, which relaxes the silicate structure. In other words, the addition of basic oxides increases the number of cations carrying an electric charge and enhances the mobility of cations by breaking the silicate network structure. Jiao et al. [17] analyzed experimental data from various sources and then concluded that the electrical conductivity of molten slags is primarily attributed to the movement of cations, while the conduction by anions can be considered negligible. Additionally, they estimated that in the SiO_2–CaO–MnO–MgO slag system, the basic oxides CaO, MnO, and MgO exist as Ca^{2+}, Mn^{2+}, and Mg^{2+}, respectively. This suggests that the electrical conductivity of the slag is directly related to the molar fraction of the contained basic oxides. In addition, Zhang et al. [69] reported that the electrical conductivity of CaO–MgO–Al_2O_3–SiO_2–Na_2O melts increases monotonically with the gradual addition of Na_2O. This finding is in good agreement with what is commonly known as a factor in the increase in electrical conductivity of molten slag by basic oxides [17,62,69,70].

In contrast, since SiO_2, an acidic oxide, has relatively large *I* value, it is difficult for the oxide to break the bonding force with the oxygen ion [71]. In the molten slag, SiO_2 combines with O^{2-} to form complex anions. Additionally, as the amount of SiO_2 in molten slag increases, SiO_4^{4-} forms large anions with ring or chain structures, such as $Si_2O_7^{6-}$, $Si_3O_{10}^{8-}$, $Si_4O_{13}^{10-}$, $Si_3O_9^{6-}$ or $Si_4O_{12}^{8-}$ [65]. Therefore, the addition of SiO_2 is considered to promote the formation of a silicate network, which reduces the mobility of carriers and consequently decreases electrical conductivity.

In the case of intermediate oxides, the electrical conductivity behavior of molten slag may vary depending on the composition of the slag. It is known that intermediate oxides function as basic oxides in slag compositions with acidic oxides and as acidic oxides in slag compositions with basic oxides [17]. **Table 2-6** provides the basicity, CaO/Al_2O_3 and CaO/SiO_2 ratios for lunar mare regolith used in the calculations. Since the mare regolith represents the acidic slag composition, Al_2O_3 is considered to act as a basic oxide in the molten mare regolith. It is known that Al^{3+} in molten slag acts as network formers by forming AlO_4^{5-} tetrahedron like

Si^{4+} [17,72-74]. However, due to the difference in charge between Al^{3+} and Si^{4+}, cations such as alkali metals and alkaline earth metals are required to compensate for electrical neutrality of Al^{3+} [62,68-70]. When M^{n+} (an n-valent cation) compensates for the charge of Al^{3+} in molten slag, it does not act as a network modifier. However, when Al^{3+} is present in higher amounts than M^{n+}, the unbalanced Al^{3+} may function as a network modifier [75]. Thus, excess Al^{3+} ions act as network modifiers, which reduce the viscosity of the molten slag and enhance carrier mobility. Therefore, it is expected that the addition of Al_2O_3 to acidic slag will generally result in an increase in electrical conductivity. However, for molten slag with high Al_2O_3 contents, it has been reported that there is a strict order for cations when compensating for Al^{3+} ions in the presence of several basic oxides together in the slag [76]. This means that the contribution of Al_2O_3 to electrical conductivity may vary depending on its concentration. If there are sufficient Ca^{2+} ions, the lower-priority Fe^{2+} ions are not used for the charge compensation of Al^{3+}. In other words, as the concentration of Al_2O_3 in molten slag increases, the relative concentration of cations decreases, allowing metal ions other than Ca^{2+} to participate in charge compensation. This results in a decrease in electrical conductivity. LIU et al. [76] measured the electrical conductivity of Fe_xO–SiO_2–CaO–Al_2O_3 slags at 1823 K when the CaO/Al_2O_3 ratio changed from 0.5 to 2.0. They found that as the C/A ratio increased from 0.5 to 0.8, the electrical conductivity increased despite a decrease in Al_2O_3 content. The variation in the behavior of intermediate oxides depending on the slag composition is considered to be due to the amphoteric character of Al_2O_3 [17].

TiO_2 may also function as a basic oxide in lunar regolith. According to Nakamoto et al. [77], an increase in TiO_2 concentration in the SiO_2–CaO–MgO–TiO_2 slag system resulted in a reduction in the viscosity of the molten slag. However, unlike Al cations, which can have coordination numbers of 4 and 6, Ti cations have a coordination number of 6. Ti cations are known to relax the network structure due to the strong attraction of Ti–O [68,78]. Additionally, because TiO_2 has a high *I* value, unlike basic oxides, Ti cations (Ti^{4+}) do not participate in conduction. In other words, while the addition of TiO_2 does not increase the number of charge carriers (cations), it may reduce the viscosity of the molten slag. In general, the electrical conductivity of molten slag tends to increase as its viscosity decreases. Specifically, the addition of TiO_2 can reduce the viscosity of molten slag, leading to enhanced mobility of cations. Thus, the reduction in viscosity is considered one of the factors contributing to the

increase in electrical conductivity.

Liu et al. [79] investigated the effects of temperature, CO/CO_2 ratio, and TiO_2 content on electrical conductivity of TiO_2–SiO_2–CaO slag. They reported that the mechanism by which Ti affects the electrical conductivity in molten slag is mainly governed by the high mobility of Ti^{3+} ions and the Ti^{3+}/Ti^{4+} ratio, which is greatly influenced by CO/CO_2 ratio. Additionally, they reported that increasing temperature stabilizes the lower oxidation state of titanium (Ti^{3+} is more stable than Ti^{4+} in this case), thereby increasing ionic conductivity. According to their results, Ti^{3+} can replace Ti^{4+} with increasing CO/CO_2 ratio. In other words, as the CO/CO_2 ratio decreases (or oxygen partial pressure increases), the oxidation reaction of Ti^{3+} becomes more thermodynamically favorable. On the other hand, at low oxygen partial pressure, Ti^{4+} can be reduced to Ti^{3+}. Consequently, when the equilibrium oxygen partial pressure increases at high temperature, Ti^{3+} ions are oxidized to Ti^{4+} ions, leading to a decrease in both ionic and electronic conductivity due to the reduction in Ti^{3+} ions. In **Fig. 2-5**, the decrease in electrical conductivity with the addition of TiO_2 as the temperature increases reflects their results well. From this perspective, it is reasonable to conclude that the electrical conductivity increases with the addition of TiO_2, which means that the estimated model accurately reproduces the effect of oxide addition on electrical conductivity.

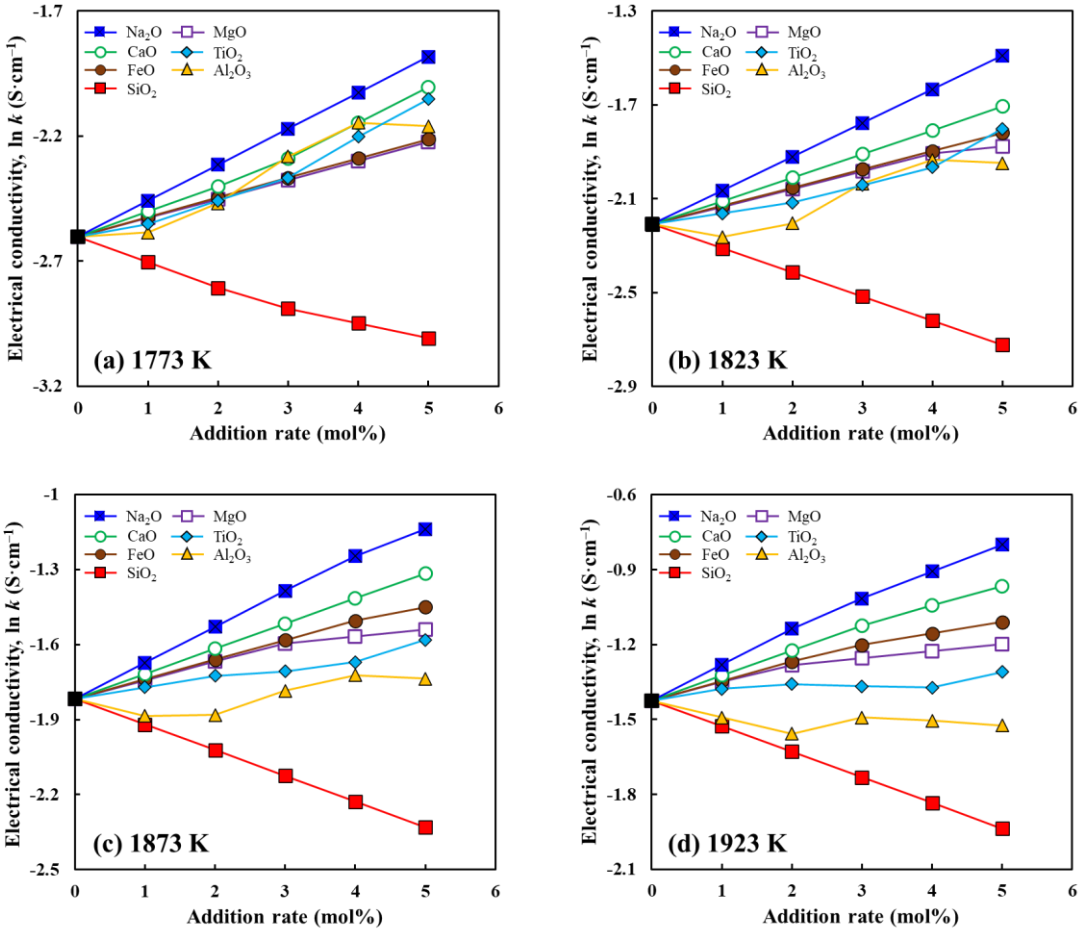

Fig. 2-5 Estimation of electrical conductivity by neural network computation with the addition of each oxide to lunar mare regolith. (a) 1773 K, (b) 1823 K, (c) 1873 K, (d) 1923 K.

Table 2-5 Ion-oxygen parameters for oxides [65].

Oxide	Cation	Cation valency (Z)	R_c (nm)	Coordination number of O^{2-}	I ($Å^{-2}$)
Na_2O	Na^+	1	0.095	6	0.36
CaO	Ca^{2+}	2	0.099	6	0.70
FeO	Fe^{2+}	2	0.075	6	0.87
MgO	Mg^{2+}	2	0.065	6	0.95
Al_2O_3	Al^{3+}	3	0.050	6	1.66
TiO_2	Ti^{4+}	4	0.068	6	1.85
SiO_2	Si^{4+}	4	0.041	4	2.45

*R_a = 0.14 nm

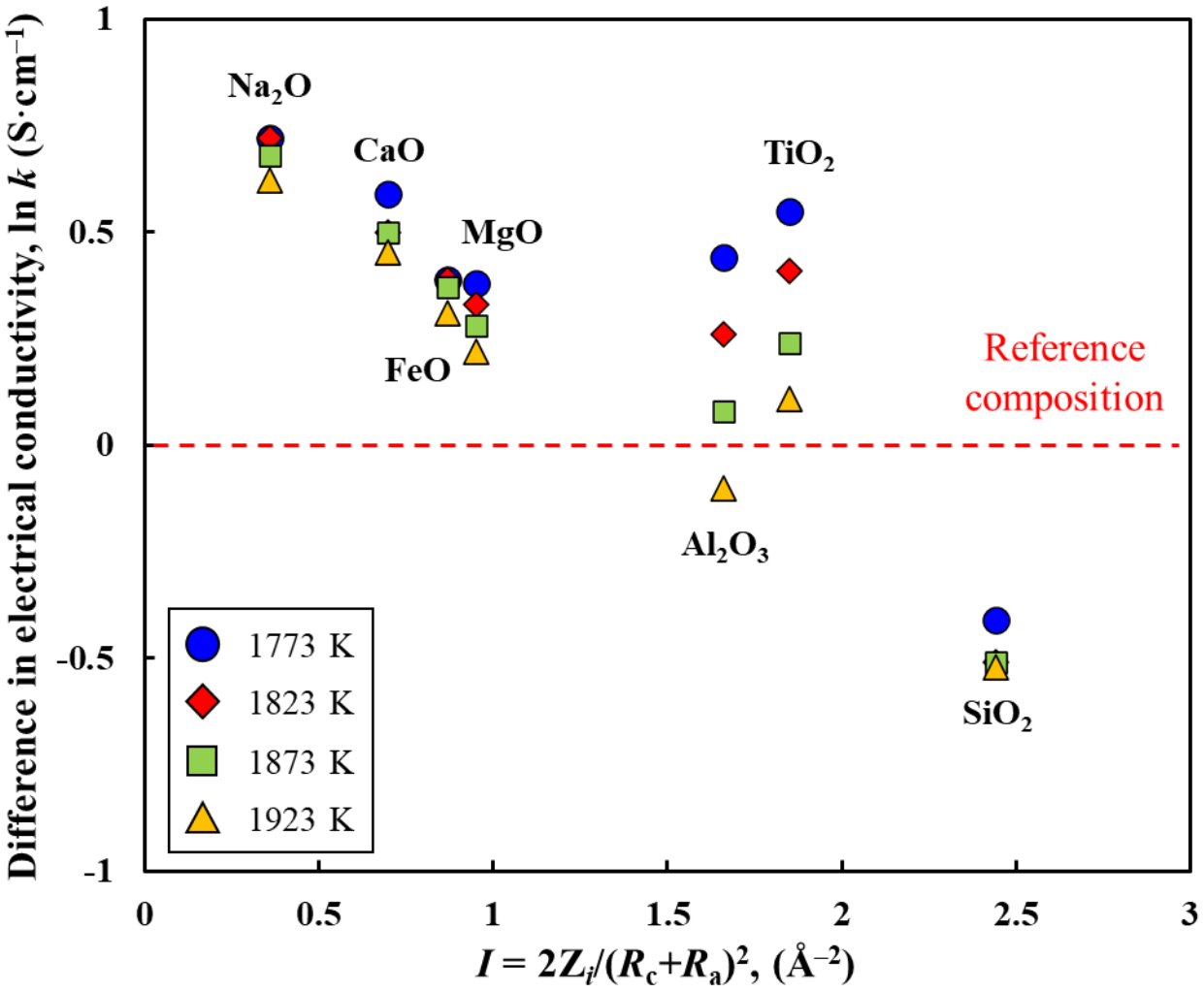

Fig. 2-6 Difference in electrical conductivity between reference composition and +5 mol% addition of each oxide with a value of *I*.

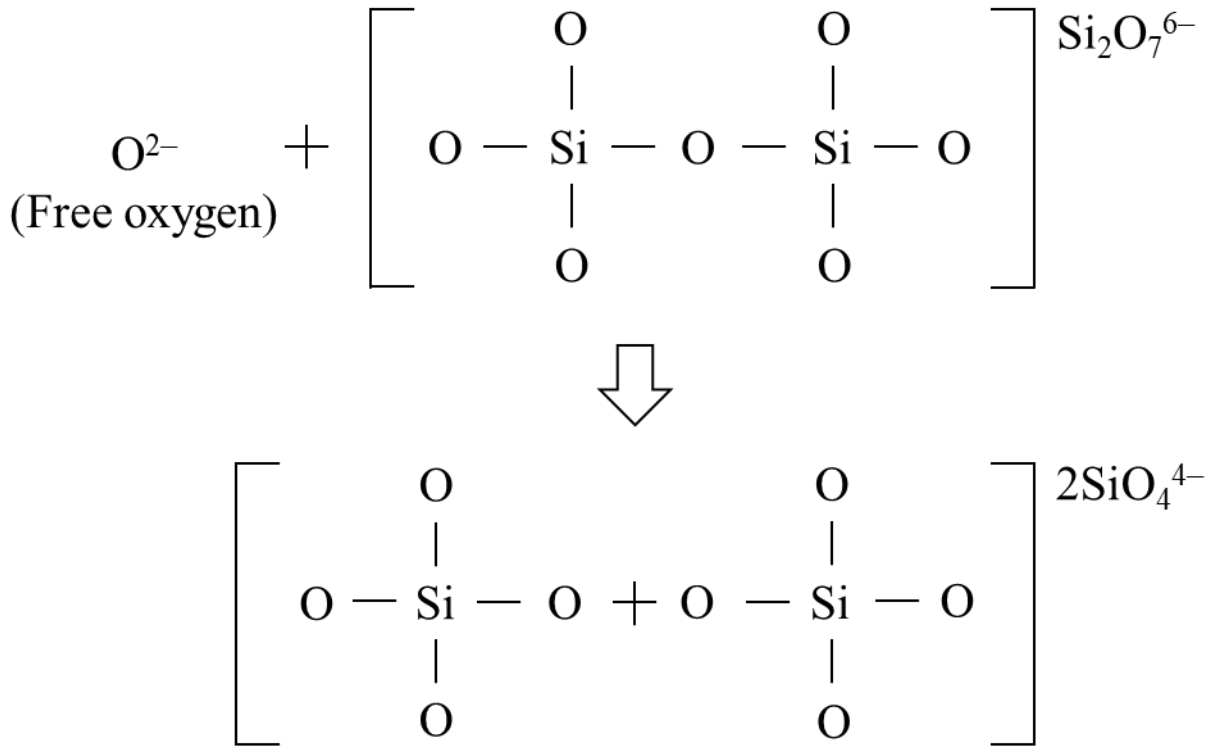

Fig. 2-7 Change in silicate network structure by a free oxygen ion.

Table 2-6 Basicity, C/A and C/S for the lunar mare regolith.

mass%	Basicity	C/A	C/S
Mare regolith	0.66	0.79	0.26

$$* \text{ Basicity} = \frac{\sum\left(X_{CaO} + X_{FeO} + X_{MgO} + X_{TiO2} + X_{Na2O}\right)}{\sum\left(X_{SiO2} + X_{Al2O3}\right)}$$

$* X_{MO}$ is mass% of MO.

2.4 Summary

In this study, the multilayer neural network modeling was performed for the reliable prediction of the electrical conductivity of multicomponent oxides. Electrical conductivity data collected from the literature for neural network modeling were used as training data in the learning process, and Bayesian optimization was utilized for hyperparameter optimization. The results obtained through this process are as follows.

(1) The predictive model accurately reproduced the literature data and demonstrated high predictive accuracy for arbitrary data. These results suggest that a reliable model for estimating electrical conductivity has been successfully developed.

(2) The estimated effect of each oxide on the electrical conductivity of the lunar mare regolith showed that basic oxides (Na_2O, CaO, FeO, MgO) increased electrical conductivity, and acidic oxides (SiO_2) decreased electrical conductivity, which is considered to depend on the magnitude of the attractive force acting between cations and oxygen ions. Al_2O_3 showed different contributions to electrical conductivity depending on composition and temperature, which is due to the amphoteric behavior of Al_2O_3. Unlike Al_2O_3, another amphoteric oxide, TiO_2, was found to contribute to increasing electrical conductivity similarly as basic oxides, which is due to a mechanism different from that of Al_2O_3.

REFERENCES

[1] M. Barati and K. S. Coley: Metall. Mater. Trans. B, 37 (2006), 51.

[2] G. H. Heiken, D. T. Vaniman, and B. M. French: Lunar Source book, Cambridge University Press, New York, (1991), 121.

[3] J. F. Lindsay: Lunar Stratigraphy and Sedimentology, Elsevier Scientific Publishing Company, New York, (1976), 227.

[4] S. S. Schreiner, J. A. Hoffman, G. B. Sanders, K. A. Lee: IEEE Aerospace Conference, (2015), 1.

[5] G. B. Sanders and W. E. Larson: Journal of Aerospace Engineering, 26 (2013), 5.

[6] L. Schlüter and A. Cowley: Planetary and Space Science, 181 (2020), 104753.

[7] A. H. C. Sirk, D. R. Sadoway and L. Sibille: ECS Trans., 28 (2010), 367.

[8] D. Wang, A. J. Gmitter and D. R. Sadoway: J. Electrochem. Soc., 158 (2011), E51.

[9] H. Kim, J. Paramore, A. Allanore and D. R. Sadoway: J. Electrochem. Soc., 158 (2011), E101.

[10] P. A. Curreri, E. C. Ethridge, S. B. Hudson, T. Y. Miller, R. N. Grugel, S. Sen and D. R. Sadoway: Process Demonstration For Lunar In Situ Resource Utilization-Molten Oxide Electrolysis (MSFC Independent Research and Development Project No. 5-81), (NASA/Technical Memorandum), (2006), https://ntrs.nasa.gov/citations/20070018263, (accessed 2024-05-28).

[11] K. Ramohalli and J. Lewis. NASA Space Engineering Research Center for utilization of local planetary resources, (NASA/Collected Works), (1992), https://ntrs.nasa.gov/citations/19930017485, (accessed 2024-05-28).

[12] C. Schwandt, J. A. Hamilton, D. J. Fray and I. A. Crawford: Planetary and Space Science, 74 (2012), 49.

[13] L. Sibille, D. R. Sadoway, P. Tripathy, E. Standish, A. Sirk, O. Melendez and D. M. Stefanescu: 48th AIAA Aerospace Sciences Meeting Including the New Horizons Forum and Aerospace Exposition, (2010), 367.

[14] S. Schreiner, L. Sibille, J. A. Dominguez, J. A. Hoffman, G. B. Sanders and A. H. Sirk: 8th Symposium on Space Resource Utilization, (2015), 1180.

[15] A. Shchetkovskiy, T. McKechnie, D. R. Sadoway, J. Paramore, O. Melendez and P. A.

Curreri: Earth and Space 2010 (Engineering, Science, Construction, and Operations in Challenging Environments), (2010), 1039.
[16] K. Hu, X.W Lv, Z.M. Yan, W. Lv and S.P. Li: Metall. Mater. Trans. B, 50 (2019), 2982.
[17] Q. Jiao and N. J. Themelis: Metall. Trans. B, 19 (1988), 133.
[18] J. Lambert Bates: Proc. Conf. on High Temperature Sciences Related to Open-cycle, Coal-fired MHD Systems, U. S. Energy Research and Development Administration, Washington, D.C., (1977), 196.
[19] G. H. Zhang and K. C. Chou: Metall. Mater. Trans. B, 41 (2010), 131.
[20] G. H. Zhang and K. C. Chou: Metall. Mater. Trans. B, 43 (2012), 849.
[21] M. Hanao, M. Kawamoto, T. Tanaka and M. Nakamoto: ISIJ Int., 46 (2006), 346.
[22] M. Nakamoto, M. Hanao, T. Tanaka, M. Kawamoto, L. Holappa and M. Hamalainen: ISIJ Int., 47 (2007), 1075.
[23] B. Derin, E. Alan, M. Suzuki and T. Tanaka: ISIJ Int., 56 (2016), 183.
[24] Y. Haraguchi, M. Nakamoto, M. Suzuki, K. Fuji-ta and T. Tanaka: ISIJ Int., 58 (2018), 1007.
[25] N. Saeki, M. Nakamoto and T. Tanaka: J. Japan Inst. Met. Mater., 87 (2023), 24.
[26] I. Hasegawa, T. Koizumi, K. Kita, M. Suzuki and T. Tanaka: J. Japan Inst. Met. Mater., 85 (2021), 247.
[27] H. Robbins and S. Monro: Ann. Math. Stat., 22 (1951), 400.
[28] D. P. Kingma and J. Ba: Conference paper at ICLR, (2015), 1.
[29] K. P. Murphy: Machine Learning: A Probabilistic Perspective, The MIT Press, Massachusetts, (2012), 245.
[30] T. Hoster, J. Pötschke: Archiv für das Eisenhüttenwesen., 54 (1983), 389.
[31] J. O'M. Bockris, J. A. Kitchener, S. Ignatowicz and J. W. Tomlinso: Discussions of the Faraday Soc., (1948), 265.
[32] J. O'M. Bockris, J. A. Kitchener, S. Ignatowicz and J. W. Tomlinso: Trans. Farad. Soc., 48 (1951), 75.
[33] A. Adachi, K. Ogino: Yoyuen (Fused Salts), 1 (1961), 151.
[34] A. Adachi, K. Ogino: Yoguen (Fused Salts), 7 (1964), 370.
[35] M. Kawahara, Y. Ozima, K. Morinaga, T. Yanagase: Nippon Kinzoku Gakkaishi., 42 (1978), 618.

[36] T. Licko, V. Danek: Silicaty., 27 (1983), 55.
[37] M. S. Rennie, D. D. Howat, P. R. Jochens: J. South Afr. Inst. Min.Metall., (1972), 1.
[38] N. L. Zhilo, I. S. Ostretsova, G. V. Charushnikova, R. F. Pershina: Izv VUZ Chern Met., 4 (1982), 35.
[39] A. I. Manakov, B. M. Lepinskikh, O. I. Bukmoyarov, A. E. Goncharov, G. I. Solovev: Izv.VUZ Chern Met., 12 (1975), 14.
[40] S. O. Baisanov, T. D. Takenov, T. G. Gabdullin, E. A. Buketov: VINITI Tech Report., (1981), 1770.
[41] S. Nesterenko, V. M. Khomenko: Russ. Metall., 2 (1985), 42.
[42] V. A. Luganov, M. E. Turkeev, T. K. Ishchanov: Metallurgia I Obogashch., 12 (1977), 75.
[43] T. Baak: Acta Chem. Scand., 8 (1954), 1727.
[44] L. Bobok, L. Bodnar, J. Schmiedl: Hutn Listy., 37 (1982), 419.
[45] A. Fuwa, M. Bessho: Nippon Kogyo Kaishi., 104 (1988), 37.
[46] W. A. Fischer, H. Vom Ende: Arch. Eisenhüttenwes., 21 (1950), 217.
[47] W. A. Fischer, H. Vom Ende: Arch. Eisenhüttenwes., 22 (1951), 417.
[48] K. Narita, T. Onoye, T. Ishii, K. Uemura: Tetsu-to-Hagané, 61 (1975), 2943.
[49] H. B. Hofmann, B. Marincek: Archiv Eisenhüttenwes., 25 (1954), 523.
[50] G. Bonetti: Riv. Stn. Sper. Vetro (Murano, Italy), 6 (1976), 241.
[51] K. Mori, Y. Matsushita: Tetsu-to-Hagané, 38 (1952), 444.
[52] T. Nakamura, Y. Suginohara, T. Yanagase: Nippon Kinzoku Gakkaishi., 39 (1975), 48.
[53] Y. Kusuda, T. Nakamura, K. Morinaga, T. Yanagase: Kyushu Daigaku Kogaku Shuho., 50 (1977), 133.
[54] K. Morinaga, Y. Suginohara, T. Yanagase: Nippon Kinzoku Gakkaishi., 38 (1974), 658.
[55] K. Mori: Tetsu-to-Hagané, 46 (1960), 134.
[56] Y. Kusuda, T. Nakamura, T. Yanagase: Nippon Kinzoku Gakkaishi., 41 (1977), 160.
[57] H. Sato, H. Sakao: Electrochem., 26 (1958), 569
[58] A. S. Churkin, Y. M. Tsikarev, G. A. Toporishchev, V. I. Lazarev, G. A. Khasin: Fizkhim Issled metallurg. Protsessov (Sverdlovsk)., 7 (1979), 40.
[59] H. Wakabayashi: Terai. R., 91 (1983), 335.
[60] A. E. Sokolov, V. I. Deev and A. I. Tikhonov: Nauch Tr Perm. Politekn. Inst., 135 (1973), 118.

[61] The Iron and Steel Institute of Japan: Physical and Chemical Data book for Iron and Steelmaking-Ironmaking-, The Iron and Steel Institute of Japan, Tokyo, (2006), 510.
[62] K. C. Mills and B. J. Keene: Int. Mater. Rev., 32 (1987), 1.
[63] F. Nogueira: Bayesian Optimization, Open source constrained global optimization tool for Python (2014), https://github.com/fmfn/BayesianOptimization, (accessed 2023-08-04).
[64] A. L. Turkevich: Proc. of The Lunar Science Conf., U. S. A, (1973), 1159.
[65] The Japan Institute of Metals: Physical Chemistry of metals, The Japan Institute of Metals, Sendai, (1996), 151.
[66] J. Park: ISIJ Int., 52 (2012), 1627.
[67] K. C. Mills: ISIJ Int., 33 (1993), 148.
[68] M. Sajid, C. Bai, M. Aamir, Z. You, Z. Yan and X. Lv: ISIJ Int., 59 (2019), 1153.
[69] G. H. Zhang, W. W Zheng and K. C. Chou: Metall. Mater. Trans. B, 48 (2017), 1134.
[70] J. H. Zhu, Y. Hou, W. W Zheng, G. H. Zhang, K. C. Chou: ISIJ Int., 59 (2019), 1947.
[71] L. Wang: Steel Research Int., 80 (2009), 680.
[72] V. V. Hoang: Phys. Rev. B, 70 (2004), 134204.
[73] S. Sukenaga, K. Kanehashi, H. Yamada, K. Ohara, T. Wakihara and H. Shibata: ISIJ Int., 63 (2023), 1263.
[74] T. S. Kim, J. H. Park: ISIJ Int., 54 (2014), 2031.
[75] Y. Sasaki, K. Ishii: Tetsu-to-Hagané, 88 (2002), 419.
[76] J. H. Liu, G. H. Zhang and K. C. Chou: ISIJ Int., 55 (2015), 2325.
[77] M. Nakamoto, Y. Tsugawa, A. Kiyose, J. Lee and T. Tanaka: J. High Temp. Soc., 32 (2006), 74.
[78] K. Mori: J. Weld. Soc., 36 (1967), 608.
[79] J. H. Liu, G. H. Zhang, Y. D, Wu and K. C. Chou: Metall. Mater. Trans. B, 47 (2016), 798.

Chapter 3

Effect of Wettability on Coalescence Behavior of Droplet in Two Immiscible Liquids

3.1 Background

As described in chapter 1, the coalescence of dispersed droplets in immiscible liquids is sometimes an issue in material processes [1-4]. Especially in the metallurgical industry, the coalescence of liquid metal droplets dispersed in molten slag can act as a major factor determining the efficiency of the process [1-4]. Although droplet coalescence is generally known to be dependent on the physical properties of the two liquids, such as viscosity, interfacial tension, and wettability, the role of wettability is still controversial [1-4]. Meanwhile, there have been various reports on the influence of wettability on the coalescence of droplets dispersed in different liquids [1-4], but the mechanism has not yet been fully explained. For a more intuitive comprehension of the effect of wettability on droplet coalescence, this chapter will examine the coalescence behavior of dispersed droplets within an immiscible liquid at room temperature from the perspectives of wetting and non-wetting phenomena, and the fundamental mechanisms will be elucidated.

To determine the wettability effect on the coalescence of droplets of one liquid in a different liquid, two experiments, (1) wettability and (2) coalescence, were conducted using immiscible liquids, liquid paraffin and glycerin aqueous solution. Based on the experimental results, the coalescence mechanism of droplets of one liquid in the other liquid was discussed in terms of the wettability phenomenon.

3.2 Experimental

The liquid paraffin and 89 mass% glycerin aqueous solution were prepared as immiscible liquids with similar viscosities to determine the wettability effect between two liquids on the coalescence of droplets. **Table 3-1** shows physical properties [5,6], such as the density, viscosity, and surface tension of two immiscible liquids at 293 K. The viscosity of liquid paraffin changes dramatically with temperature [7]. Therefore, the viscosity of liquid paraffin

was measured at 293 K using a capillary viscometer (Ubbelohde, Sibata Scientific Technology, Soka, Japan).

Table 3-1 Physical properties of liquid paraffin and glycerin aqueous solution at 293 K [5,6].

At 293 K	Density (g/cm^3)	Viscosity (mPa·s)	Surface tension (mN/m)
Liquid paraffin	0.86	204	33
89 mass% glycerin aqueous solution (11 mass% water)	1.23	204	65

3.2.1 Wettability Experiment by Placing a Droplet on an Immiscible Liquid

Two types of equipment were prepared for the wettability experiment: (a) a quartz tube (outer diameter: 45 mm, inner diameter: 41 mm), and (b) a rectangular plastic box (width: 45 mm, height: 70 mm, depth: 12 mm). First, the quartz tube is filled with liquid paraffin. Then, a drop of glycerin solution is placed on the surface of the paraffin liquid and observed from the side. Although the density of the glycerin aqueous solution is higher than that of liquid paraffin (**Table 3-1**), the droplet of the glycerin solution floats on the liquid paraffin owing to the balance of interfacial tensions working at the boundary of three phases [8,9]. A camera with 8 million pixels was used for observation, and the glycerin droplet was photographed after it floated and stabilized on the surface of the flowing paraffin.

Secondly, the rectangular plastic box is filled with glycerin solution. Similarly, a drop of paraffin solution is placed on the surface of the glycerin solution and observed from the side. Since the density of the flowing paraffin solution is lower than that of the glycerin solution, the paraffin floats on top of the glycerin solution. Different equipment was used in the two experiments because the second experiment facilitates smoother observation of the liquid paraffin on the surface of the glycerin solution. Liquid paraffin forms a very thin layer on the surface of the glycerin solution, and it is difficult to observe this thin layer from the side in the quartz tube because the glycerin solution inside the tube creates a curved concave surface.

3.2.2 Coalescence Experiment by Settling and Floating of Droplets

Two layers in a quartz tube were prepared for coalescence experiments. The thicknesses of the upper paraffin layer and the lower glycerin solution layer were 25 mm, respectively, as shown in **Fig. 3-1**. Glycerin droplets were dropped, or paraffin droplets were floated by the injector positioned at 10 and 20 mm from the interface. The droplet volume was restricted to 0.009 mL by adjusting the diameter of the nozzle. Since the two liquids have similar viscosities, the wettability effect on the coalescence of paraffin droplets through a glycerin solution can be compared with that of glycerin droplets through liquid paraffin. The time required for coalescence was measured after the droplet reached the interface until it coalesced with the same solution layer. In the experiment, the force due to gravity working on the droplet, F, is expressed by the following equation.

$$F = (\rho_2 - \rho_1) \cdot g \cdot V \qquad (3-1)$$

Here, ρ_1 is the density of the fluid, ρ_2 is the density of the droplet, g is the gravitational acceleration, and V is the volume of the droplet. Since the volume of the droplet is adjusted to be the same, the force (F) acting on the droplet during settling/floating is always the same. In addition, since the two liquids in a quartz tube share the same interface, the interfacial tension of the two liquids is also the same, which means that only the effect of wettability on droplet coalescence can be observed in this experiment. 10 experiments were performed on settling and floating of droplets at two different initial positions. All experiments were recorded on video, and the same camera used in 3.2.1 was used.

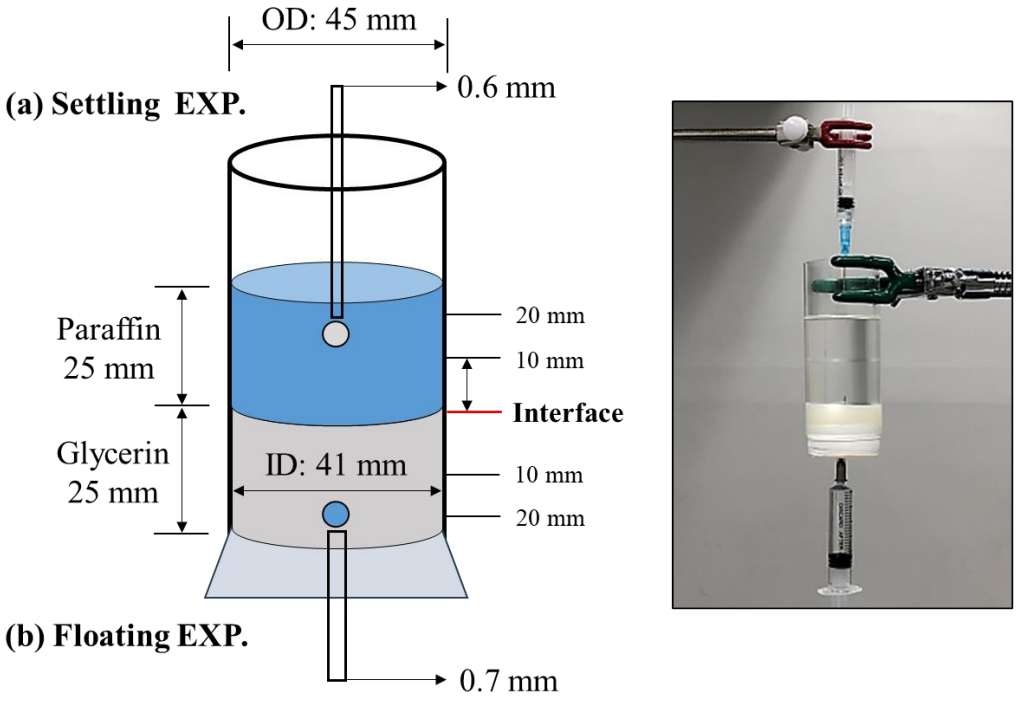

Fig. 3-1 Schematic of the experimental apparatus.

3.3 Results and Discussion

3.3.1 Wettability between Droplet and Immiscible Liquid

Figure 3-2 shows the appearance of droplets placed in an immiscible solution under two conditions. The glycerin droplet maintains a spherical shape in liquid paraffin solution, and the liquid paraffin covers most of the glycerin droplet surface as shown in **Fig. 3-2(a)**. This is because the glycerin droplet does not wet the paraffin. Wettability is determined by the contact angle formed between a liquid droplet and the interface it rests upon. In general, when $0^{o} < \theta < 90^{o}$, it is defined as "wetting", and when $90^{o} < \theta < 180^{o}$, it is defined as "non-wetting".

The contact angle (θ) between the droplet and the interface, as shown in **Fig. 3-2(a)**, is $90^{o} < \theta < 180^{o}$, indicating "non-wetting". In contrast, the paraffin droplet spread on the surface of the glycerin solution as shown in **Fig. 3-2(b)**. In other words, the paraffin droplet wets the glycerin; as shown in **Fig. 3-2(b)**, the contact angle is $0^{o} < \theta < 90^{o}$, indicating "wetting". This wetting behavior depends on the surface tension of the liquid. In general, a solution with a low surface tension will wet a liquid with a high surface tension [1-4].

Therefore, in this study, "wetting" and "non-wetting" are defined by the contact angle between the droplet and the interface. **Figure 3-2(a)** indicates "non-wetting", while **Figure 3-2(b)** indicates "wetting". Based on this definition, the effect of wettability on coalescence was examined in the following section.

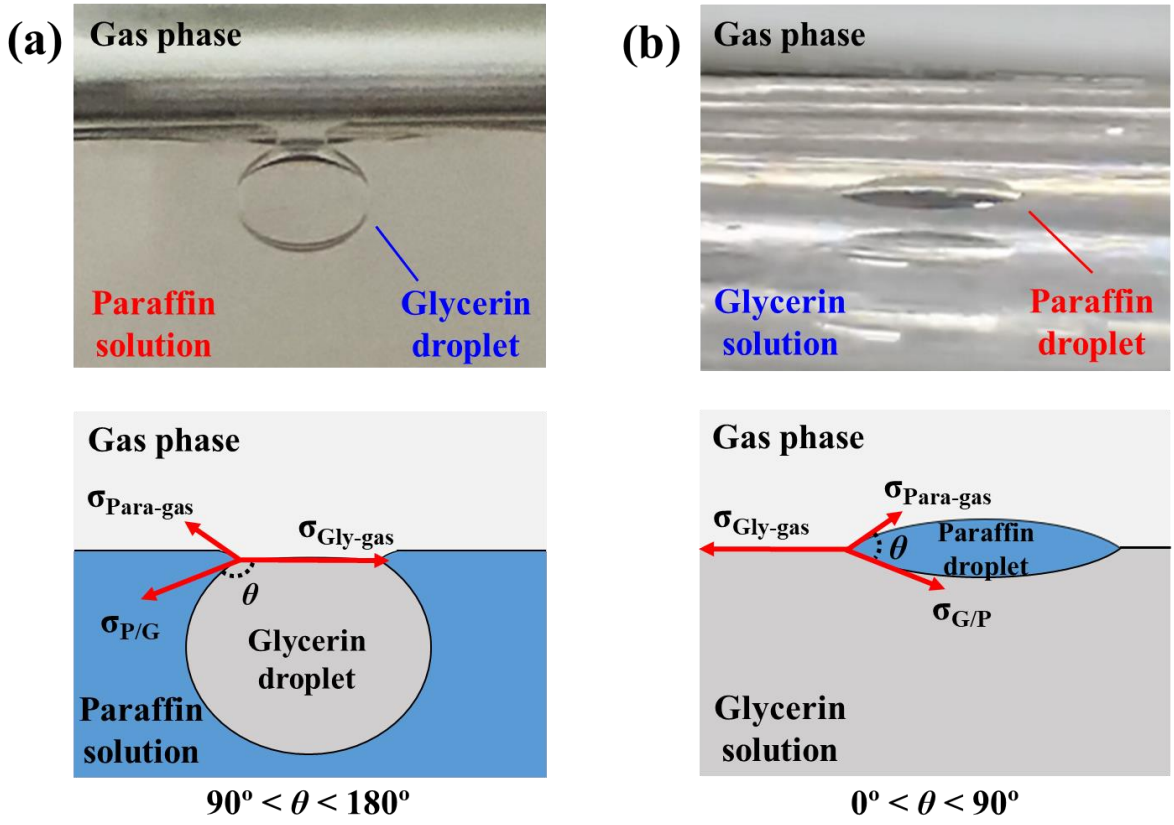

Fig. 3-2 Wetting shape between the droplet and solution. (a) "Non-wetting" case and (b) "Wetting" case.

3.3.2 Coalescence of Droplet in Immiscible Liquid

Figure 3-3 shows the motions of the droplets, from settling/floating to arrival at the interface and then coalescing. In this study, the time for the droplet to be absorbed into the body after reaching the interface was measured, and this was defined as the coalescence time. A glycerin droplet released in the paraffin solution reached the top of the interface, as shown in **Fig. 3-3(a)**. A glycerin droplet did not immediately coalesce into the glycerin body and floated on the interface. Since gravity acts on a droplet, a convex curve was formed under the interface, and after a certain period of time, a droplet coalesced into the body. A paraffin droplet floated in the glycerin solution reached below the interface, as shown in **Fig. 3-3(b)**. A paraffin droplet also did not immediately coalesce into the paraffin body, remained below the interface, and after a certain period of time, coalesced in the paraffin body. Here, based on the definition of wettability in Section 3.3.1, the glycerin droplet in the paraffin solution, as shown in **Fig. 3-3(a)**, corresponds to the "wetting" case. On the other hand, the paraffin droplets in the glycerin solution, as shown in **Fig. 3-3(b)**, corresponds to the "non-wetting" case. That is, the settling and floating experiments are "wetting" and "non-wetting" cases, respectively.

Figure 3-4 shows the results for the coalescence times of all the experiments. Here, a slight scattering was observed at the coalescence time for the same conditions, probably due to small bubbles contained in the interface while the two layers are being prepared. Thus, the difference in coalescence time is discussed qualitatively here. The mean times on the coalescence of glycerin droplets settled in liquid paraffin at distances of 10 and 20 mm from the interface were 310 and 267 s, respectively. Meanwhile, the mean times on the coalescence of paraffin droplets floated in the glycerin solution at distances of 10 and 20 mm from the interface were 26 and 19 s, respectively. A quantile-quantile (Q-Q) plots of the experimental results were performed to assess the adequacy of the mean considering data dispersion, as shown in **Fig. 3-5**. The data obtained from the coalescence experiments roughly indicates a straight line in the Q-Q plot, indicating a Gaussian distribution, although some data points deviate from the line. This deviation is considered to be due to the small sample size. It is expected that with an increase in the number of experimental data points, the graph will more closely approximate a Gaussian distribution in the Q-Q plot [10]. Therefore, the mean of the measured data is considered to be an appropriate representative value. As illustrated in **Fig. 3-4**, the coalescence time observed in this experiment did not significantly differ depending on the droplet settling/floating distance.

This indicates that the droplets reached their terminal velocity during settling/floating, resulting in consistent coalescence times regardless of the distance. The coalescence of paraffin droplets with the body in the glycerin solution occurred more rapidly than that of glycerin droplets. This suggests that the “non-wetting” case facilitates droplet coalescence more readily. Since the forces acting on the two liquids are equal, the difference in the coalescence behavior can be explained in terms of the wettability below.

Figure 3-6 illustrates the expected coalescence mechanism in the experiment. In **Fig. 3-6(a)**, the glycerin droplet settles onto the interface due to gravity (orange arrow), and the liquid paraffin between the glycerin droplet and the body is expelled from the gap (yellow arrow). As the liquid paraffin wets both the glycerin droplet and the body, a capillary force (red arrow) acts to cover the surfaces of the glycerin droplet and the body with the liquid paraffin, generating a repulsive force (blue arrow) in the narrow gap. Therefore, when the glycerin droplet reaches the interface, a thin film of liquid paraffin forms between the glycerin droplet and the body. After the thin film of liquid paraffin is completely drained from the narrow gap at the contact point, the droplet and the body can come into contact and coalesce. The liquid paraffin drains from the narrow gap over time due to gravity acting on the glycerin droplet, and the glycerin droplet eventually coalesces into the body. Here, the drainage of liquid paraffin means the flow of liquid paraffin from the gap, and the drainage velocity at which paraffin flows from the gap depends on the wettability.

Wang et al. [11] reported that wettability can affect boundary slip when a liquid flows over a solid surface. They found that as the wettability of the surface improves, the slip length monotonically decreases, resulting in a reduction of the liquid flow velocity. Although the liquid-liquid system in this study differs from the liquid-solid system, the trend of the wettability effect on boundary slip is reasonably considered to be independent of the system [12]. Consequently, the drainage velocity of the liquid in the gap decreases as wettability improves. In other words, when liquid paraffin wets the glycerin droplet and body, the drainage velocity of liquid paraffin film in the gap decreases, resulting in an increased coalescence time of glycerin droplet.

Similarly, in **Fig. 3-6(b)**, the paraffin droplet is suspended at the interface due to buoyancy (orange arrow), and the glycerin solution between the paraffin droplet and the body is expelled from the gap (yellow arrow). The drainage velocity of the glycerin solution in the gap between

the paraffin droplet and the body is faster in the non-wetting case than in the “wetting” case, due to the longer slip length [11]. Since the glycerin solution does not wet the paraffin droplet and the body, it is spontaneously expelled from the narrow gap by capillary action (red arrow), generating a contracting force (blue arrow) in the gap.

Additionally, in the non-wetting case, a cavity can form in the gap between the paraffin droplet and the body during the drainage of glycerin solution when a certain distance is reached, as shown in **Fig. 3-6(b)**. Several studies [13-18] have reported the formation of a cavity between solid particles in hydrophobic liquids. Sasai [16,17] observed a cavity between Al_2O_3 cylinders in molten iron and reported that the appearance of a cavity in the gap promotes the agglomeration of solids by the cavity bridging force. It has also been reported that when the distance between solid particles is less than a certain distance, a cavity spontaneously appears even if the particles are not in contact [17]. Assuming the same mechanism applies to liquid-liquid systems as to liquid-solid systems, it is reasonable to consider that the glycerin solution spontaneously recedes from the narrow gap between the paraffin droplet and the body due to capillary action, forming a cavity in the gap. Given that the equilibrium thickness of cavities in solid-liquid systems has been reported to be submicron [14], the cavity was not confirmed in the present observation system. Nevertheless, capillary action can generate a cavity in the narrow gap, resulting in the formation of cavity bridging forces. Consequently, the coalescence of droplets in non-wetting liquids is expected to be facilitated by the faster drainage and the contracting force generated by the cavity effect.

The present findings indicate that the wettability between two liquid substances affects the coalescence behavior of the droplet in another liquid. This fundamental knowledge can be applied to the coalescence phenomenon of liquid iron droplets dispersed in the molten slag generated in the metallurgical process discussed in chapter 1. Here, considering the results in chapter 3, it is expected that the worse the wettability between the droplets and another liquid, the easier the drainage between the droplets, thus promoting coalescence of liquid droplets. In the metallurgical process, conversely, it is expected that better wettability between molten slag and iron droplets will lead to slower drainage between droplets, making the coalescence of iron droplets more difficult. A detailed discussion in this regard is discussed in chapter 5.

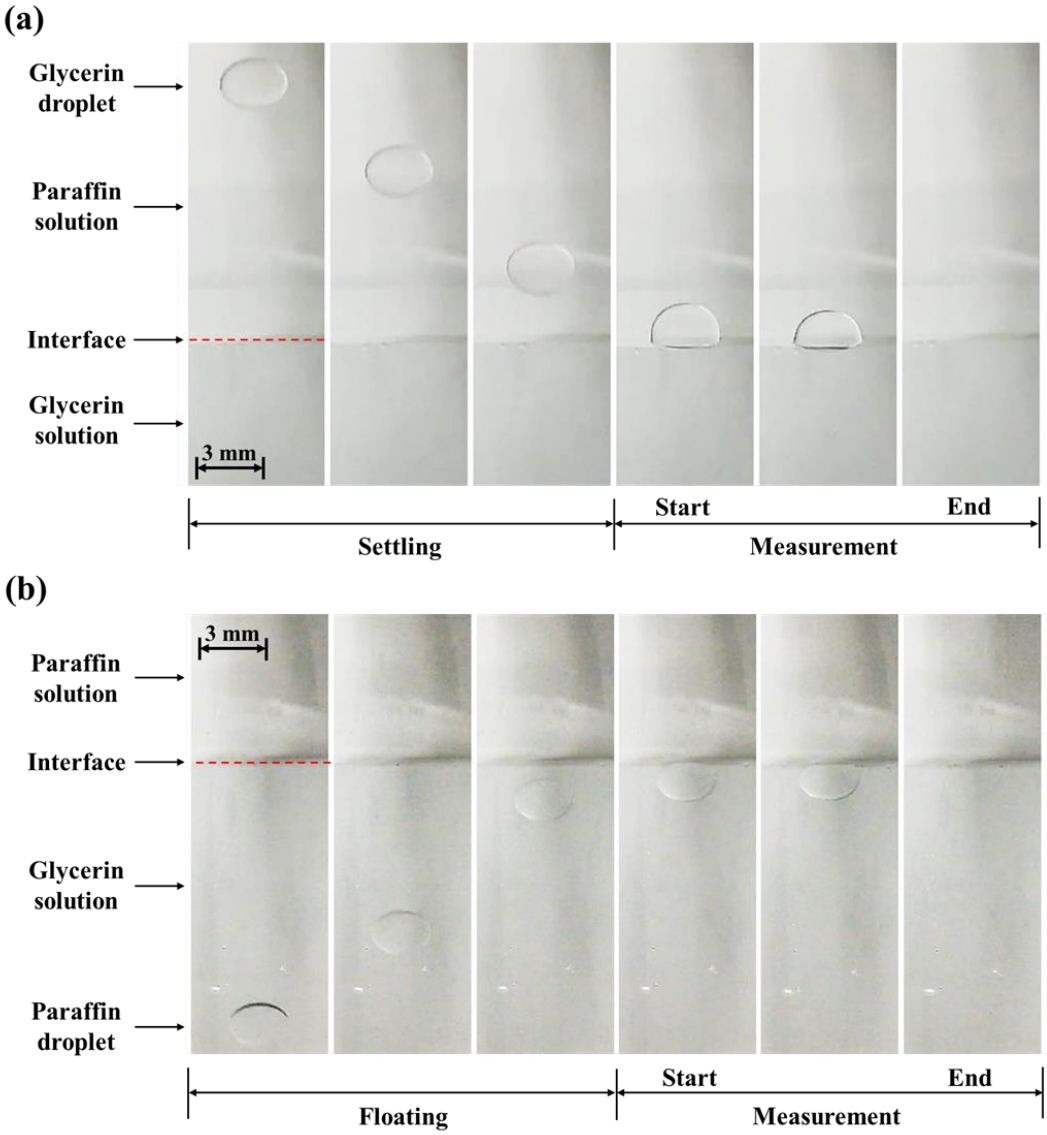

Fig. 3-3 Motions of droplets from settling/floating to their arrival at the interface and subsequent coalescence. (a) Settling of glycerin droplet in liquid paraffin solution and (b) Floating of paraffin droplet in glycerin aqueous solution.

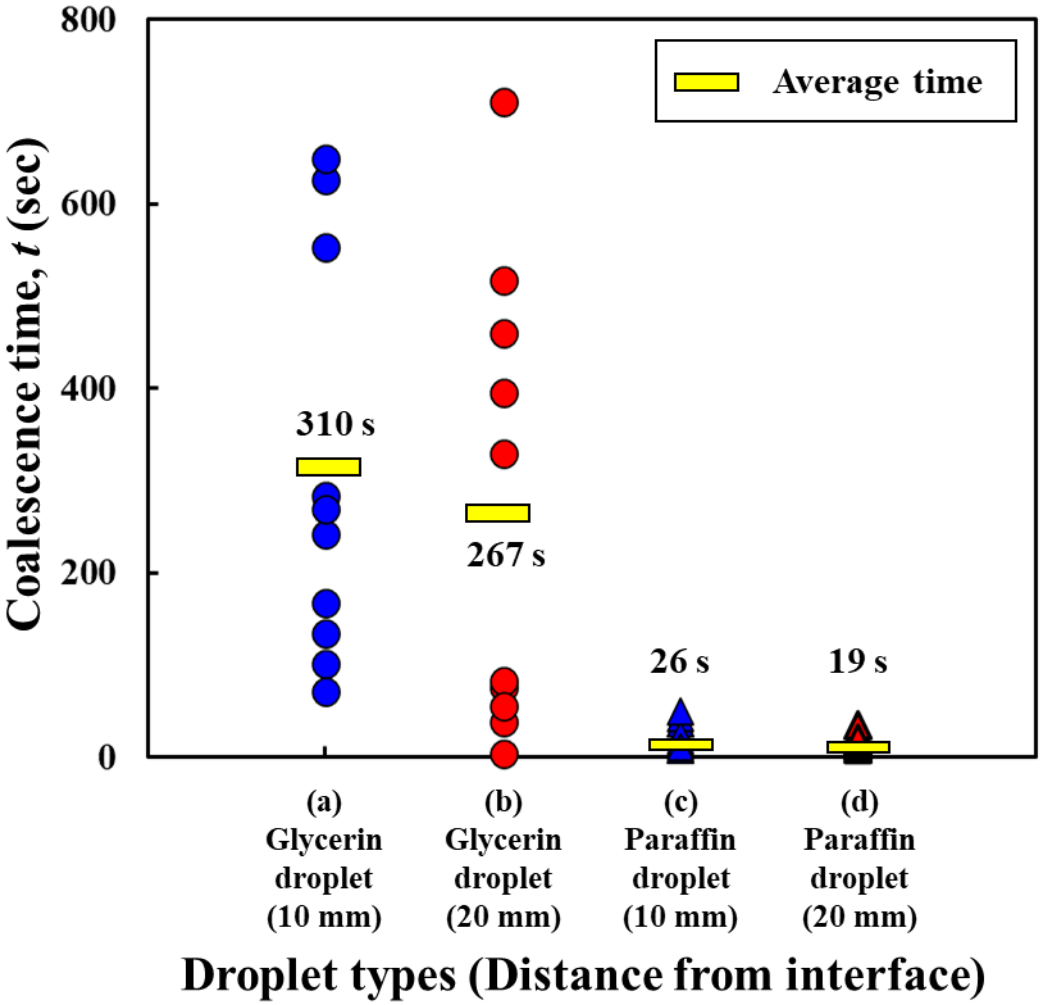

Fig. 3-4 Comparison of coalescence time with the type of droplet and distance from interface. (a), (b): Wetting cases. (c), (d): Non-wetting cases.

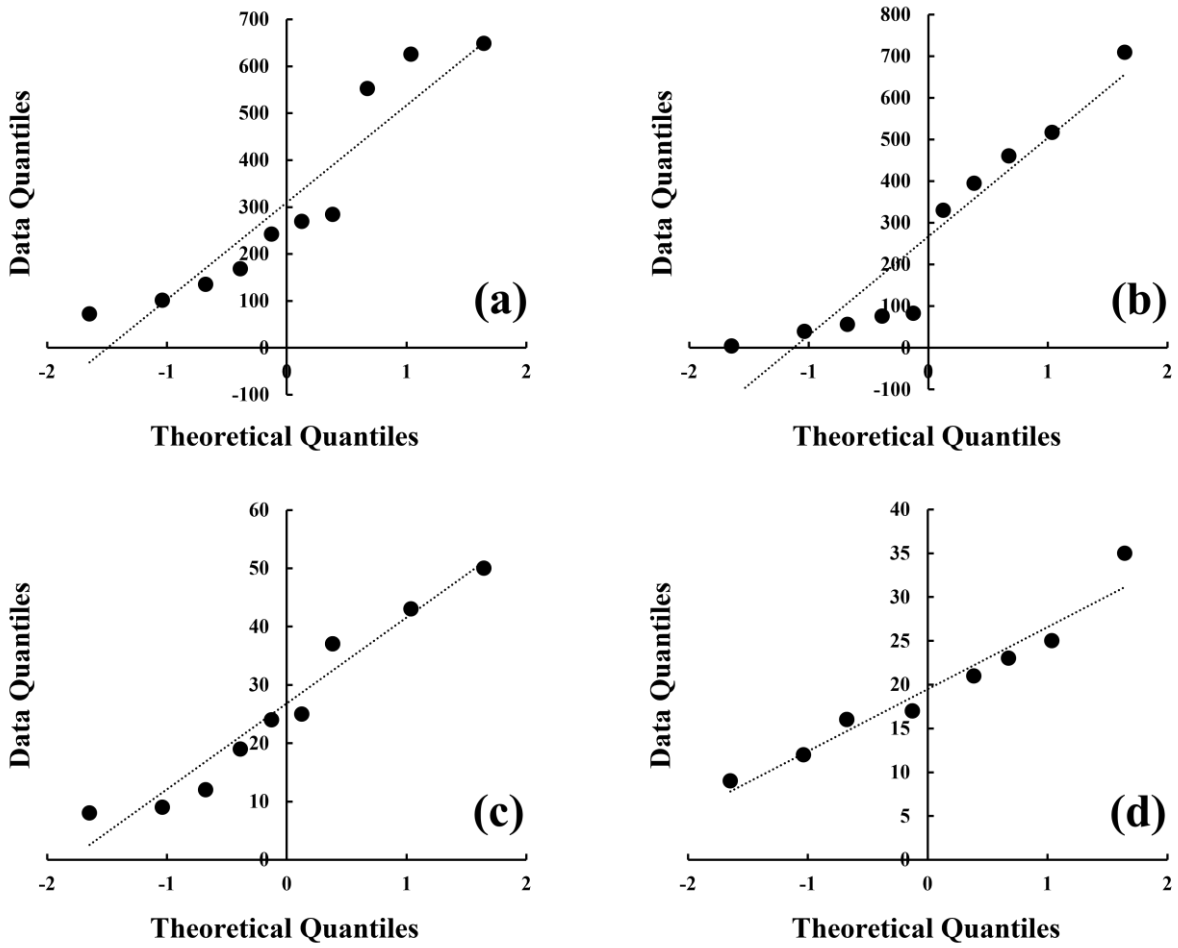

Fig. 3-5 Q-Q plot on experimental data for (a) Glycerin 10 mm, (b) Glycerin 20 mm, (c) Paraffin 10 mm, (d) Paraffin 20 mm.

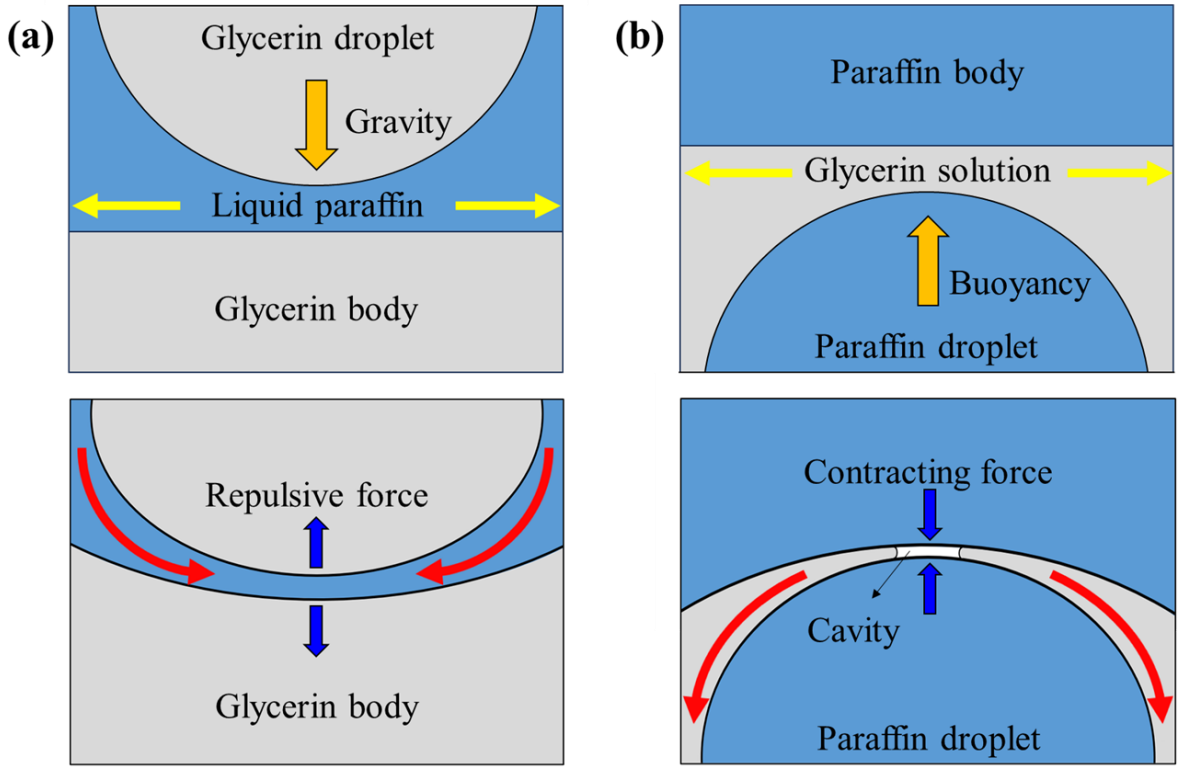

Fig. 3-6 Process on coalescence of droplet in (a) “Wetting” and (b) “Non-wetting” cases.

3.4 Summary

To determine the effect of wettability on the coalescence behavior of droplets in immiscible liquids, two basic experiments were performed using liquid paraffin and aqueous glycerin solutions, and the conclusions were as follows.

(1) In the wettability experiments, it was found that liquid paraffin “wetted” glycerin droplets, whereas glycerin aqueous solution did not “wet” paraffin droplets, which was attributed to the difference in the surface tension.

(2) In the coalescence experiments, the coalescence of paraffin droplets in the glycerin solution (non-wetting) exhibited a shorter time than that of glycerin droplets in liquid paraffin (wetting). This is attributed to the difference in drainage velocity of the thin film at the interface due to different wettability, and the promotion of coalescence in the non-wetting case by the formation of cavities in the gap.

The above findings are expected to be applied to the system of molten slag and dispersed liquid iron droplets in a metallurgical process. The discussion in molten slag and liquid Fe system is described in chapter 5.

REFERENCES

[1] M. Nakamoto, H. Goto, M. Suzuki and T. Tanaka: Int. J. Microgravity Sci. Appl., 32 (2015), 320103.

[2] S. Natsui, R. Nashimoto, T. Kumagai, T. Kikuchi and R. O. Suzuki: Metal. and Mater. Trans. B, 48 (2017), 1792.

[3] M. He, N. Wang, Q. How, M. Chen and H. Yu: Powder Technol., 362 (2020), 550.

[4] J. Isaksson, A. Andersson, T. Vikström, A. Lennartsson and C. Samuelsson: Journal of Sustainable Metallurgy, 9 (2023), 1378.

[5] J. Yong, F. Chen, Q. Yang, J. Hou and X. Hou: Chem. Soc. Rev., 46 (2017), 4168.

[6] J. B. Segur, H. E. Oberstar: Ind. Eng. Chem., 43 (1951), 2117.

[7] M. D. Marko, J. P. Kyle, Y. S. Wang and E. J. Terrell: PLoS One, 12 (2017), 1.

[8] M. Nakamoto, Y. Kasai, T. Tanaka and T. Yamamoto: Colloids and Surfaces A, 603 (2020), 125250.

[9] M. Nakamoto, T. Tanaka and T. Yamamoto: Metals, 12 (2022), 1198.

[10] D. M. Lane, D. Scott, M. Hebl, R. Guerra, D. Osherson, and H. Zimmer: Online Statistics Educatio, Rice University, Houston, 272, https://onlinestatbook.com/2/, (accessed 2024-05-28).

[11] R. Wang, J. Chai, B. Luo, X. Liu, J. Zhang, M. Wu, M. Wei and Z. Ma: J. Nanotechnol., 12 (2021), 1237.

[12] L. Hilaire, B. Siboulet, S. Charton and J. F. Dufrêche: Langmuir, 39 (2023), 2260.

[13] V. V. Yaminsky, V. S. Yushchenko, E. A. Amelina and E. D. Shchukin: J. Coll. Int. Sci., 96 (1983), 301.

[14] V. S. Yushchenko, V. V. Yaminsky and E. D. Shchukin: J. Coll. Int. Sci., 96 (1983), 307.

[15] M. Nakamoto, T. Tanaka, M. Suzuki, K. Taguchi, Y. Tsukaguchi and T. Yamamoto: ISIJ Int., 54 (2014), 1195.

[16] K. Sasai: ISIJ Int., 54 (2014), 2780.

[17] K. Sasai: ISIJ Int., 56 (2016), 1013.

[18] M. Nakamoto and T. Tanaka: Testu-to-hagané, 109 (2023), 847.

Chapter 4

Reduction and Recovery Behavior of Lunar Regolith Simulant to Metallic Fe by Hydrogen

4.1 Background

As introduced in chapter 1, the reduction of lunar regolith by hydrogen is a process with potential realization. This chapter discusses the hydrogen reduction process to extract and recover Fe from lunar regolith, focusing on metal extraction rather than oxygen extraction from a metallurgical perspective. Although several investigations on the hydrogen reduction of metal oxides from the regolith simulant for the recovery of metal have been actively conducted, the research has remained at the efficiency of reduction under the solid state [1-7]. In addition, to the best of our knowledge, studies emphasizing the separation of reduced metals from residual oxides in the lunar regolith, such as the metal-slag separations in conventional metallurgical process, which is a critical issue for recovering metals, have not been conducted so far. Given the comparable components of the Moon, the Earth and slag as shown in **Tables 1-1, 1-2** and **1-3**, the findings accumulated on physicochemical properties of high-temperature liquids, as well as the approaches developed in the research for conventional metallurgical processes could be valuable and utilized in the development of metal extraction processes.

In this chapter, high-temperature H_2 reduction and melting experiments were designed to extract metallic Fe from lunar regolith based on thermodynamic predictions with FactSage as a first step investigation. In the experiment, the fractional reduction of regolith simulant and the Fe recovery after melting were evaluated to discuss the reaction behavior for each process step and the recovering of metallic Fe in the melting process with the cross-sectional observations and the viscosity of molten slag as a physical property of molten slag.

4.2 Experimental

4.2.1 Sample Preparation

In this study, a lunar regolith simulant was used instead of the actual lunar regolith. **Figure 4-1** shows regolith simulant used in the experiment, which was manufactured by processing volcanic rock from Mt. Fuji. **Table 4-1** shows the chemical composition of regolith simulant, which is similar to the mean composition of the Lunar mare region. The major elements of regolith simulant were analyzed using inductively coupled plasma spectroscopy, and the type and amount of Fe oxide were estimated by potassium dichromate titration.

The actual lunar regolith is known to contain only Fe^{2+} due to its low oxygen partial pressure [8,9]. On the other hand, samples produced on the Earth contain a small amount of Fe^{3+} that is completely uncontrollable. The regolith simulant used in this study contains Fe^{3+} in addition to Fe^{2+}. In this study, Fe^{3+} was assumed to be Fe_2O_3, and the amount of Fe_2O_3 was estimated from the total Fe in the regolith simulant. The total Fe was approximately 9.33 mass% in the regolith simulant, and FeO and Fe_2O_3 were estimated to be 6.13mass% and 6.53mass%, respectively. **Figure 4-2** shows the XRD patterns of regolith simulant. The main peaks indicated anorthite; $CaAl_2Si_2O_8$ and pyroxene; $XY(Si, Al)_2O_6$ where X = Fe^{2+}, Mg, Ca and Na, Y = Fe^{3+}, Ti, Al and Mg. Iron (Fe) and titanium (Ti) are considered to exist in pyroxene. Regolith simulant was crushed to less than 125 μm and dried it at 473 K for 24 h to remove moisture.

Fig. 4-1 Lunar regolith simulant powder used in the experiment.

Table 4-1 Chemical composition of regolith simulant by ICP analysis.

Oxide	SiO_2	T.Fe	FeO	Fe_2O_3	TiO_2
mass%	49.60	9.33	6.13	6.53	1.53

CaO	Al_2O_3	MgO	Na_2O	K_2O	P_2O_5
9.45	16.90	5.62	2.61	0.71	0.26

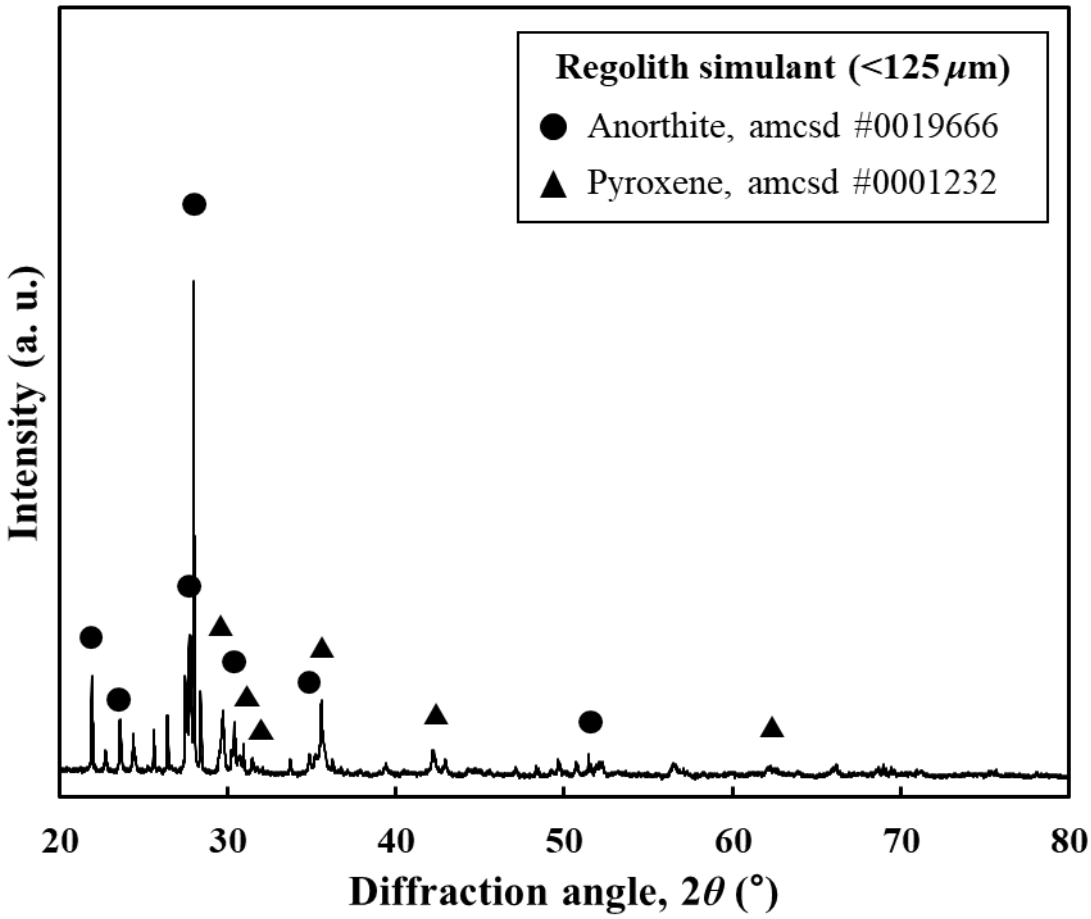

Fig. 4-2 XRD pattern of regolith simulant before reduction.

4.2.2 Equilibrium Phase Prediction by Thermodynamics Software

To design the experimental process, the equilibrium phases of the regolith simulant were predicted using FactSage 8.1 thermodynamic software with FactPS and FToxide databases. Only the components that make up more than 1 mass% were used in the FactSage prediction, excluding potassium oxide (K_2O) and phosphorus pentoxide (P_2O_5). **Figure 4-3** shows the equilibrium phases of the lunar regolith as predicted by FactSage under an oxygen partial pressure of 10^{-15} atm. Here, the total pressure is 1 atm and the temperature range is 1273–2073 K. The oxygen partial pressure was set by directly specifying the activity of the oxygen gas phase in FactSage system.

In **Fig. 4-3**, the y-axis and x-axis represent weight (g) and temperature (K), respectively. A total of 98.37 g was input for the calculation, excluding oxygen and trace elements. The formation of molten slag and metallic Fe begins at 1323 K, as shown in **Fig. 4-3**. At this temperature, four minerals coexist: feldspar, clinopyroxene, titania spinel, and tridymite (SiO_2). That is, Fe exists as complex oxides with various elements in clinopyroxene and titania spinel at 1323 K. Similarly, Ti is primarily combined with Fe oxides to form titania spinel at this temperature. All mineral phases melt at approximately 1573 K, resulting in the maximum amount of molten slag at this point. The Fe phase formed at 1323 K undergoes phase transformations as the temperature increases and eventually melts completely into a liquid phase at 1773 K. Only molten slag and liquid iron are present at 1873 K, as listed in **Table 4-2**, with their chemical compositions calculated by FactSage. **Table 4-2** indicates that the slag phase is primarily composed of SiO_2-based complex compounds, while the liquid metal phase mainly consists of Fe–Si–Ti alloy at 1873 K. Therefore, the results of FactSage calculations suggest that it is possible to extract metallic Fe from the regolith simulant under equilibrium conditions at low oxygen partial pressure.

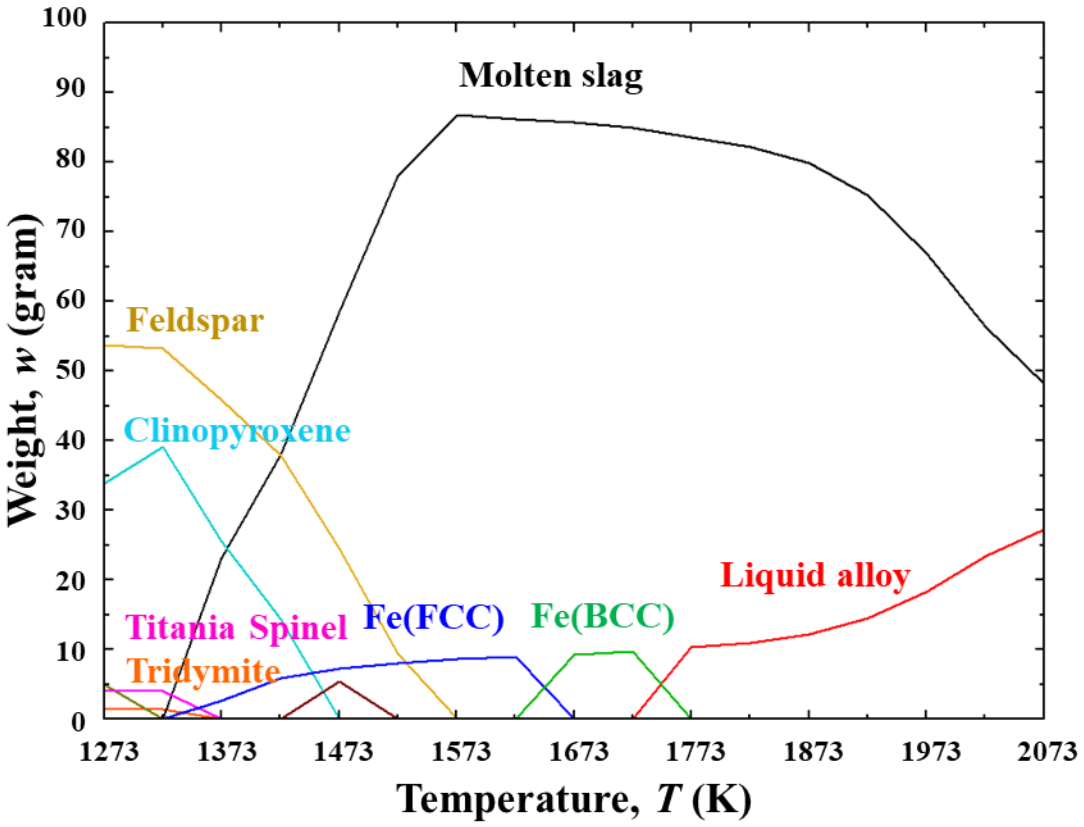

Fig. 4-3 Prediction of equilibrium phase of regolith simulant by FactSage at $P_{O2}=10^{-15}$ atm.

Table 4-2 Chemical compositions of molten slag and liquid alloy at 1873 K calculated by FactSage.

Molten slag	mass%	Liquid alloy	mass%
SiO_2	55.07	Fe	76.93
Al_2O_3	22.21		
CaO	11.79	Si	21.10
MgO	7.01		
Na_2O	2.57	Ti	1.97
Ti_2O_3	0.75		
TiO_2	0.58	Bal.	< 0.01
Bal.	< 0.01		

4.2.3 Apparatus and Procedure

Figure 4-4 shows a schematic diagram of the experimental setup. A high-temperature experimental apparatus was used to investigate the recovery behavior of metallic Fe from regolith simulant. A furnace with molybdenum disilicide heating elements was used. A B-type thermocouple connected to proportional integral derivative (PID) controller was located on the outside surface of the alumina reaction tube. An alumina Tammann tube (Nikkato Corporation, Japan, 95 mass%, diameter = 17 mm; height = 100 mm) was used as a container for the regolith simulant. Since the bottom of the crucible containing the sample was round, it was secured using an outer porous alumina crucible as shown in **Fig. 4-4**. An alumina crucible containing approximately 5 g of sample was placed in an alumina tube (outer diameter = 60 mm; inner diameter = 50 mm; height = 1000 mm, 99.8 mass%). After the furnace chamber was evacuated by a mechanical pump, it was filled with high purity argon (Ar) gas (99.999%). **Figure 4-5** shows the experimental process designed based on the thermodynamic prediction by FactSage, which is divided into two steps: reduction (step 1) and melting (step 2). Although low oxygen partial pressure is used to reduce Fe oxide in the lunar environment, it is very difficult to generate an oxygen partial pressure of 10^{-15} atm in a vacuum system. Therefore, this study used H_2 gas flow during the experimental process. Step 1 was a reduction process, in which regolith simulant particles less than 125 μm in diameter were reduced to fine Fe particles by H_2 gas. Step 2 was a melting process that melts regolith simulant and reduced Fe particles to recover metallic Fe from the molten slag. In this study, Ar–20%H_2 gas was selected, anticipated to lower the oxygen potential to satisfy for Fe oxide reduction, focusing on the feasibility for reduction of Fe oxide.

Approximately 5 g of sample was heated to 1273 K in an alumina crucible with Ar gas at a flow rate of 100 mL/min. At 1273 K, the sample was reduced with 100 mL/min of Ar–20%H_2 with reduction time (step 1). The sample was then heated to 1873 K and melted with melting time (step 2). After melting, the sample was cooled to room temperature and the crucible was crushed to recover the Fe alloy. In this study, the recovery is defined by Eq. (4-1):

$$\text{Recovery}\ (\%) = \frac{\text{Recovered bulk Fe alloy (g)}}{\text{Total Fe in original sample (g)}} \times 100 \qquad (4-1)$$

The recovered metallic Fe sample contained trace elements, and thus it was referred to as the "Fe alloy". However, as will be discussed later, since the concentrations of elements other than Fe were very small, the Fe alloy was assumed to be pure Fe when calculating the recovery ratio. Additionally, only the bulk Fe alloy was considered in the recovery calculations, and the fine Fe particles dispersed in the slag phase were excluded.

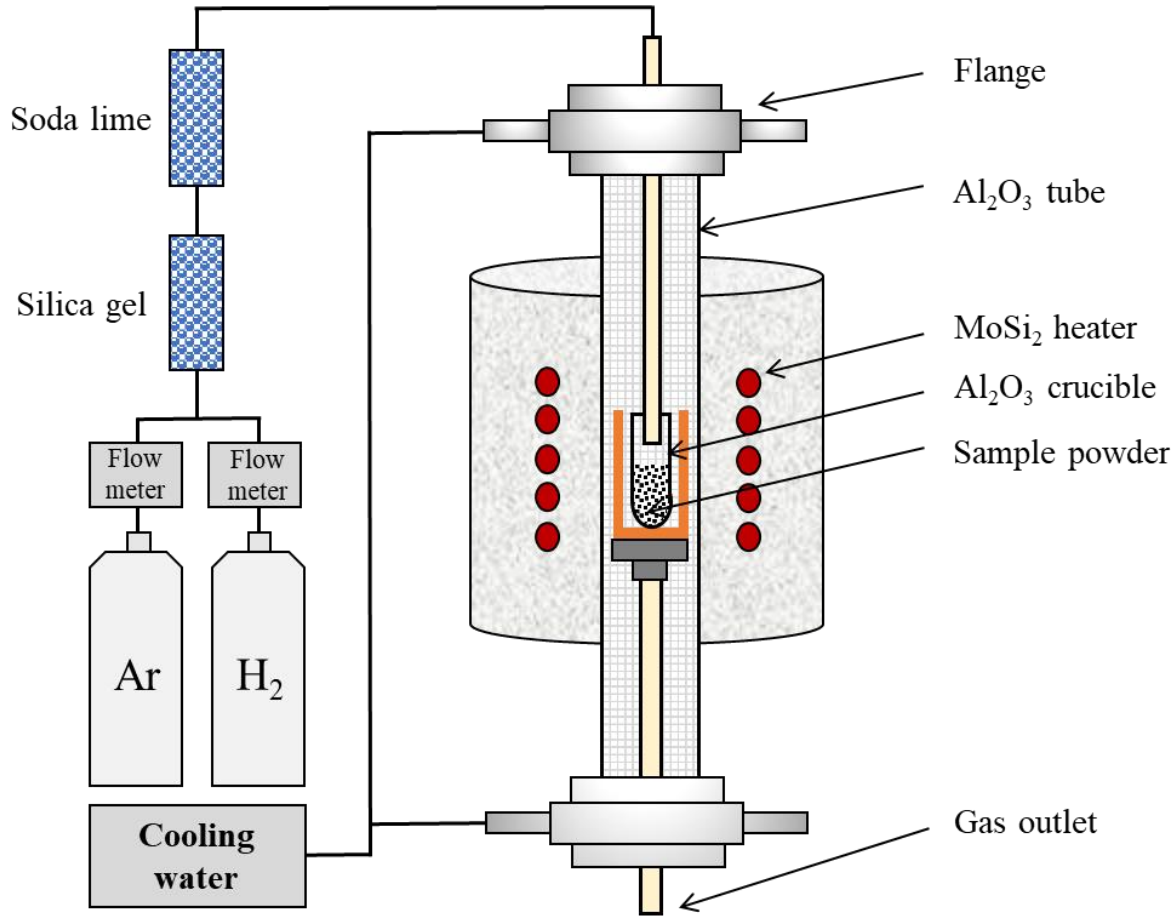

Fig. 4-4 Schematic of the experimental apparatus used in the experiment.

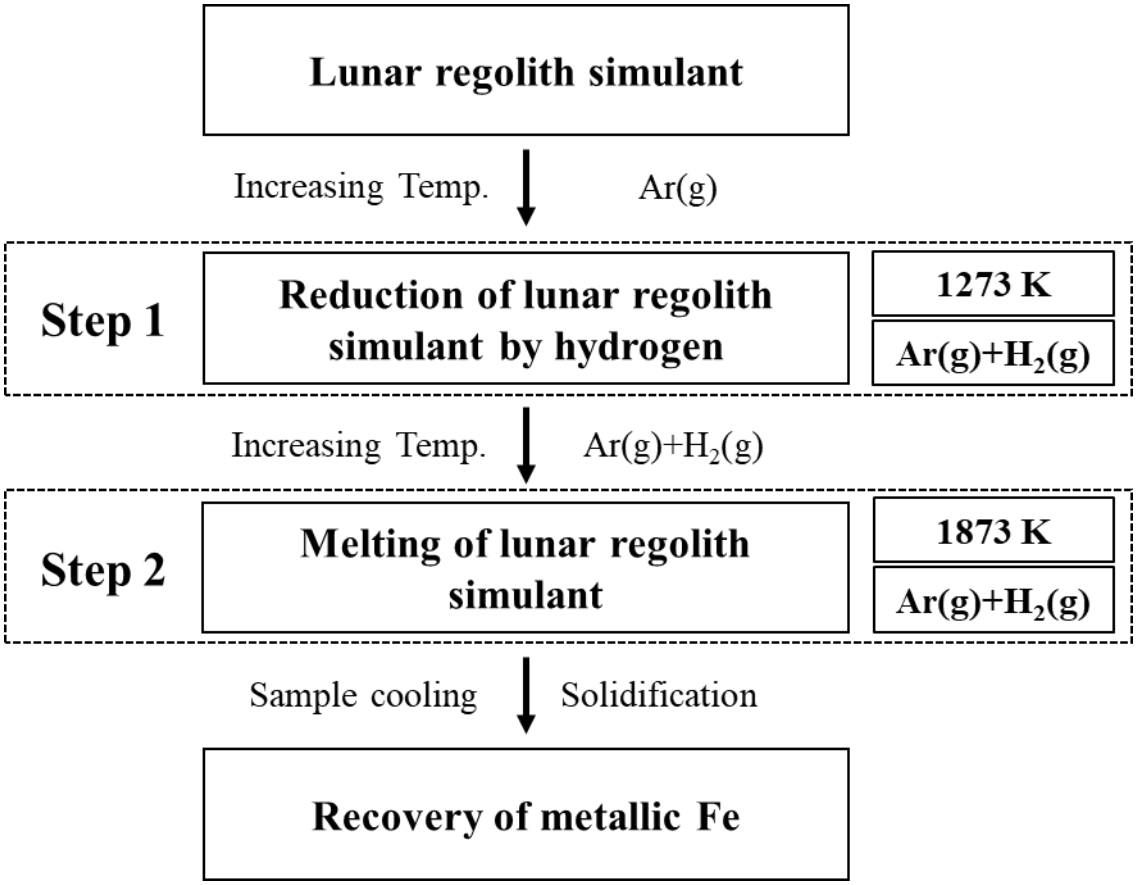

Fig. 4-5 Conceptual flowsheet of experimental process steps.

4.3 Results and Discussion

4.3.1 Reduction of Fe Oxide in Lunar Regolith Simulant by Hydrogen

As a preliminary experiment, reduction experiments were performed on regolith simulant under the conditions of Ar–10%H_2 at a flow rate of 100 mL/min. **Figure 4-6** shows XRD patterns of the original sample before reduction and the samples recovered after 30, 60, and 90 min of reduction at 1273 K by Ar–10%H_2. The iron peak appears from 30 min reduction, and its intensity increases with increasing reduction time. Based on the results of the preliminary experiments, all subsequent experiments were performed in Ar–20%H_2 at a flow rate of 100 mL/min.

Figure 4-7 shows the cross-section and EDX elemental mapping of the sample recovered after reduction at 1273 K for 2 h in Ar–20%H_2. The mapping images indicate the absence of oxygen (blue) in Fe-rich regions (bright orange), indicating that Fe oxides were reduced to Fe by H_2 in these Fe-rich regions.

Figure 4-8 shows the recovery ratio of Fe alloy as a function of reduction time at 1273 K, with the melting time fixed at 1 h at 1873 K. The recovery ratio of Fe alloy varied from approximately 24% to 41%, showing a significant increase with reduction time. These results indicate that sufficient time is required for the complete reduction of Fe oxides in the minerals to metallic Fe by H_2. Based on the results of this experiment, the reduction time was fixed at 2 h and subsequently a melting experiment was conducted. Here, in order to determine the reduction rate of regolith simulant by H_2 in the reduction step (step 1), the sample was maintained at 1273 K for 2 h and the change in weight loss of the sample was observed. Assuming that H_2 reacts only with oxygen combined as Fe oxide, the fraction of the weight loss is the same as the fractional reduction of Fe oxides. The fractional reduction of Fe oxide in the regolith simulant under the conditions of 2 h reduction was approximately 38.3%. The fractional reduction was obtained by calculating the weight loss as a percentage by measuring the weight of the sample before and after the reduction experiment in step 1.

Figure 4-9 shows XRD patterns of slag obtained after the melting experiment. The spectrum shows a broad peak indicating a glassy phase, suggesting that the regolith simulant was completely melted. **Figure 4-10** shows the appearance of the sample after the melting experiment, where the recovered slag was uniformly glassy, and the Fe alloy was located at the

bottom of the crucible in a spherical ball shape. This indicates that the regolith simulant completely melted at 1873 K, resulting in the Fe particles to settle at the bottom due to gravity. **Figure 4-11** shows SEM images of the cross-section of slag and bulk Fe alloy after reduction-melting of regolith simulant. Fine Fe particles that were not recovered were dispersed inside the slag, with diameters mostly ranging from a few μm to 10 μm, as shown in **Fig. 4-11**. **Table 4-3** shows the EDX results of the recovered bulk Fe alloy and the slag obtained after the melting experiment. The chemical composition of the recovered Fe alloy and slag was largely uniform. However, the composition of the recovered sample differs from the results calculated by FactSage in **Table 4-2**. The composition of the Fe alloy predicted by FactSage in **Table 4-2** contains large concentrations of Si and Ti, and the molten slag contains almost no Fe.

The reason for this difference is that the experiment was an open system with continuous processes and was not maintained long enough to reach equilibrium. From the perspective of free energy, SiO_2 and TiO_2 have relatively more stable free energy values compared to FeO, making their reduction more difficult. Therefore, it is considered that the reduction of Fe oxide will occur first, followed by the reduction of SiO_2 and TiO_2 from the molten slag.

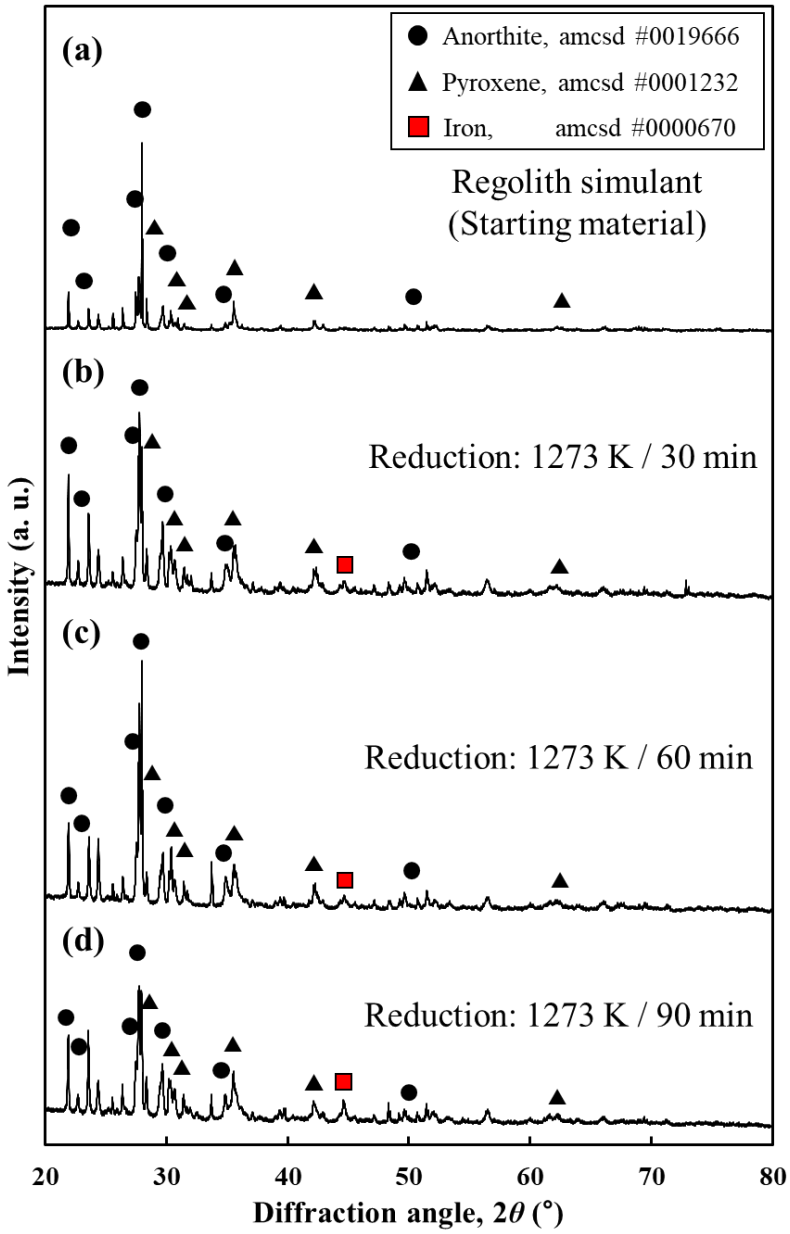

Fig. 4-6 Comparison of XRD patterns of the original sample before reduction and the samples recovered after reduction in Ar–10%H_2 atmosphere. (a) Regolith simulant, and after reduction of (b) 30 min, (c) 60 min, (d) 90 min.

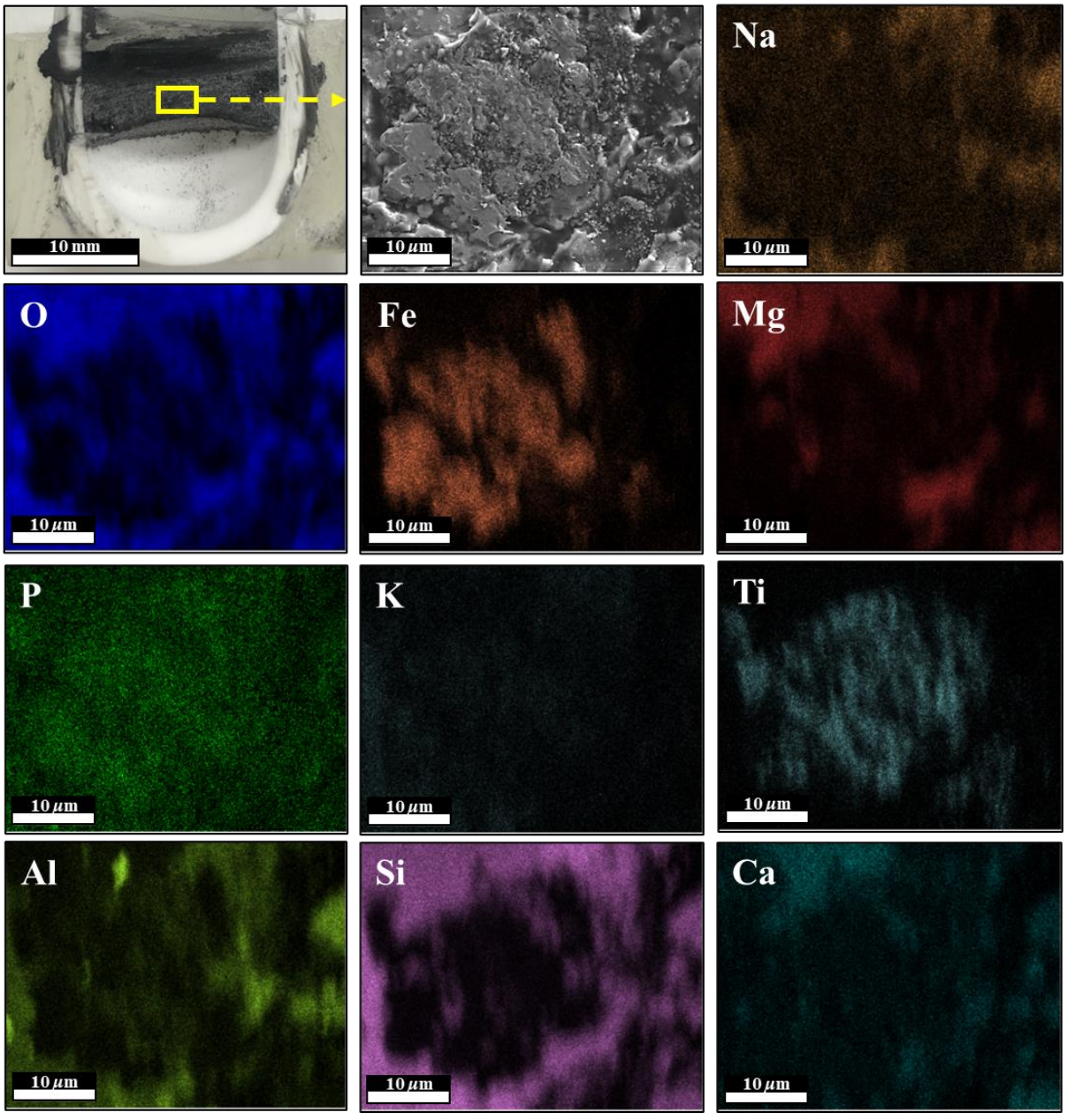

Fig. 4-7 Appearance of the cross-section and EDX elemental mapping of the sample recovered without a melting step after 2 h of reduction at 1273 K in Ar–20%H_2 atmosphere.

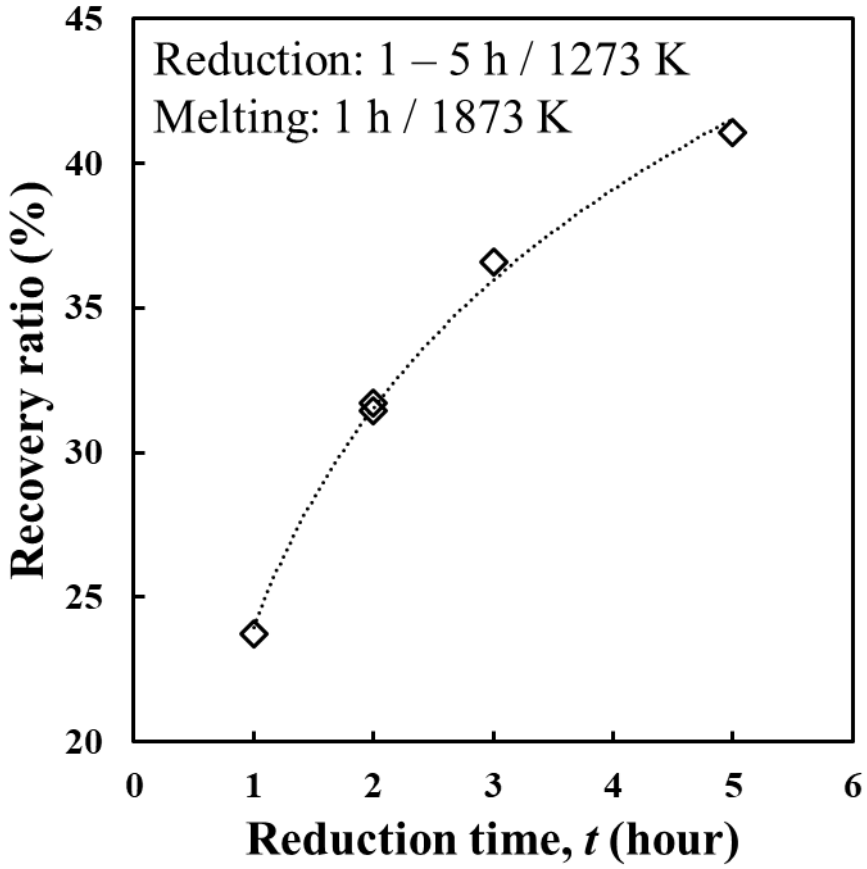

Fig. 4-8 Change in recovery ratio of Fe alloy with reduction time at 1273 K under melting condition of 1 h at 1873 K in Ar–20%H_2 atmosphere.

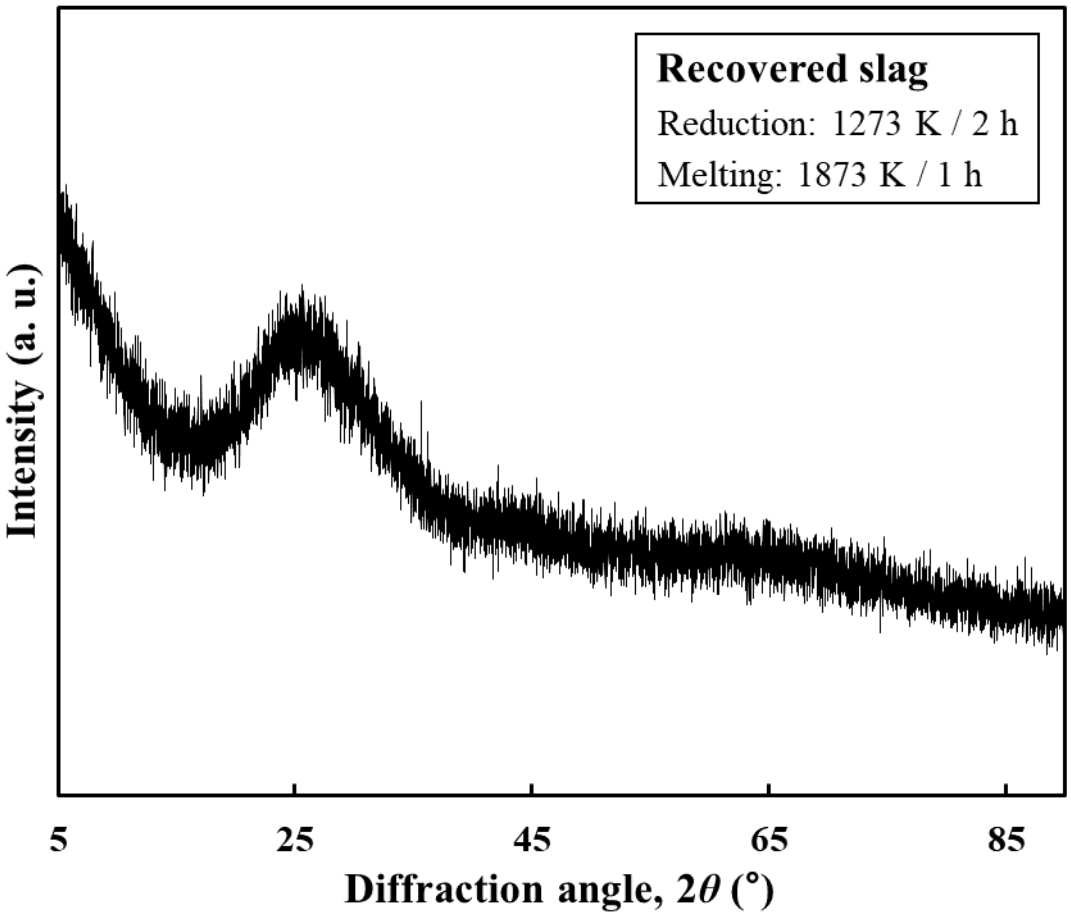

Fig. 4-9 XRD pattern of regolith simulant after melting at 1873 K in Ar–20%H_2 atmosphere.

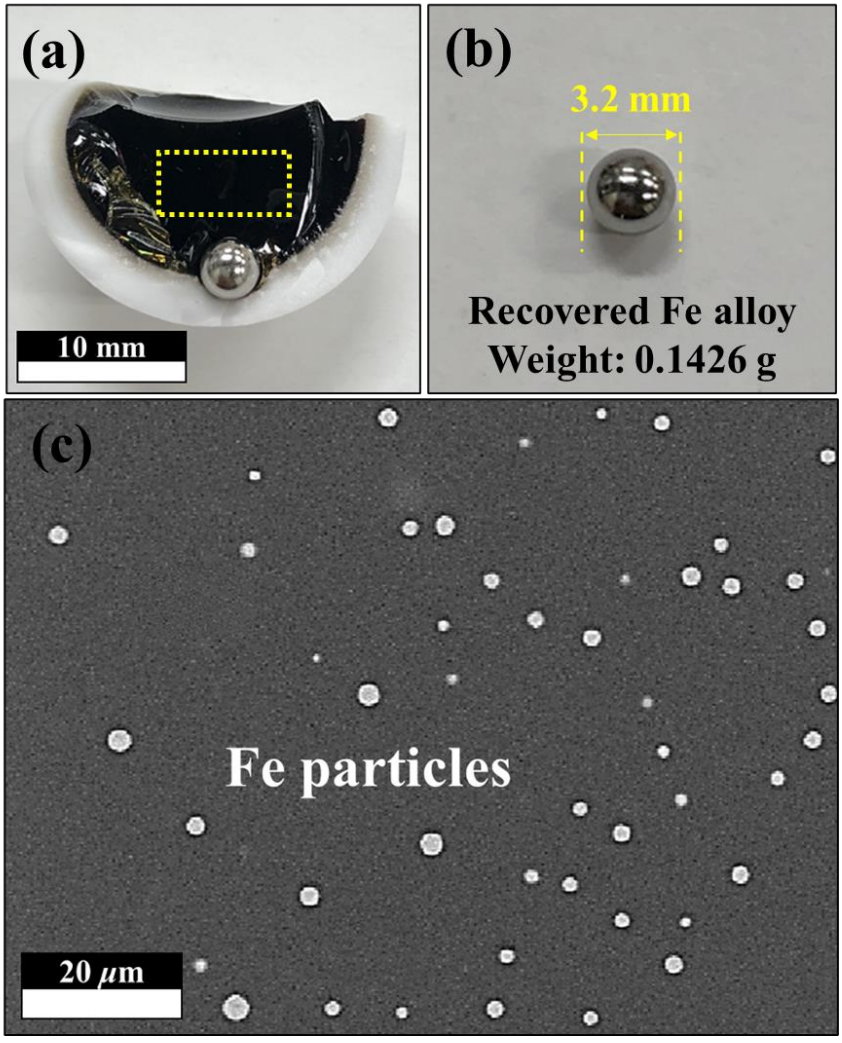

Fig. 4-10 Appearance of the sample recovered after 2 h of reduction at 1273 K and 1 h of melting at 1873 K. (a) Slag and Fe alloy recovered after reduction and melting experiment. (b) Recovered bulk Fe alloy. (c) SEM image of cross-section of area in yellow box in (a) showing fine Fe particles (white dots) in the slag.

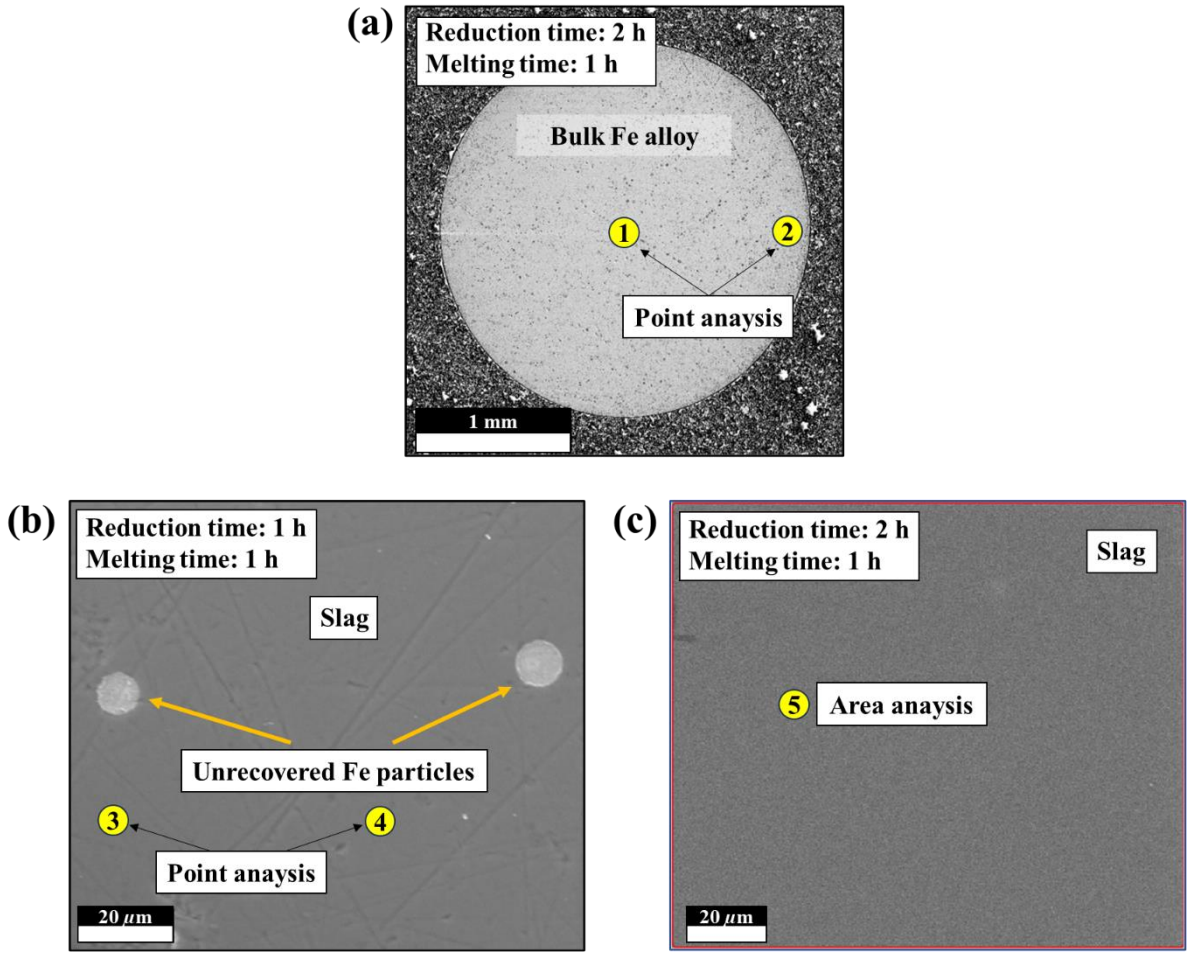

Fig. 4-11 SEM image of cross-section of the sample recovered after 1 to 2 h of reduction at 1273 K and 1 h of melting at 1873 K in Ar–20%H_2 atmosphere. (a) The cross-section of bulk Fe alloy recovered after the experiment. (b) The cross-section of the slag showing fine Fe particles. (c) The cross-section of the slag in area without Fe particles.

Table 4-3 Chemical compositions of bulk Fe alloy and slag in **Fig. 4-11** obtained by scanning electron microscopy with energy-dispersive X-ray spectroscopy.

No.	Bulk Fe alloy (mass%)			
	Fe	P	Si	Ti
(1)	97.77	2.07	0.10	0.05
(2)	97.64	2.17	0.15	0.04

No.	Slag (mass%)						
	SiO_2	CaO	Al_2O_3	MgO	Na_2O	FeO	TiO_2
(3)	51.26	10.90	18.70	6.47	3.14	7.66	1.86
(4)	51.30	10.74	18.57	6.31	3.01	7.96	2.11
(5)	47.64	11.11	21.04	5.85	3.27	9.08	2.02

4.3.2 Change in Recovery with Melting Time

Figure 4-12 shows the recovery ratio of Fe alloy as a function of melting time at 1873 K, with the reduction time fixed at 2 h at 1273 K. The recovery ratio varied with the melting time, approximately ranging from 30 to 35%, and it has been shown that the effect of the melting step on the recovery ratio is relatively minor compared to the reduction step, which showed a recovery rate of 24 to 41% as shown in **Fig. 4-8**. This result is due to the difference in reduction mechanisms between the solid and liquid states of the regolith simulant. The regolith simulant remains solid at 1273 K, allowing H_2 gas to penetrate the powder layer and proceed with the reduction on the surface of all particles bearing Fe oxides. However, at 1873 K, the regolith simulant completely melts into a liquid phase, resulting in H_2 reacting only with Fe oxides at the surface of the molten slag. Thus, the diffusivity of H_2 gas varies depending on the phase of the sample, resulting in different surface areas participating in the reduction reaction.

Figure 4-13 shows the cross-section and SEM images of the slag in the sample recovered after holding at 1273 K for 2 h in an Ar atmosphere without H_2, followed by melting at 1873 K for 1 h in an H_2 atmosphere. The recovered sample showed no presence of bulk Fe alloy, with only fine Fe particles observed within the slag. From **Fig. 4-13**, it is observed that the particle size increases from the surface towards the bottom. This result clearly indicates that H_2 gas only reacts with Fe oxide on the surface of molten slag in the melting step, whereas its reaction is less significant than in the reduction step. These results indicate that, considering the diffusivity of H_2 gas, the temperature of the reduction step should be lower than the melting point of the slag.

Figure 4-14 schematically illustrates the reduction process of Fe oxides by H_2 and the formation of bulk Fe alloy. During the reduction step at 1273 K, H_2 gas reacts with the Fe oxides in the regolith simulant powder, resulting in the formation of fine Fe particles. Subsequently, these fine Fe particles melt and coalesce inside the molten slag at 1873 K, forming bulk Fe alloy at the bottom of the crucible. These results indicate that, considering the diffusivity of H_2 gas, the temperature of the reduction step should be lower than the melting point of the slag.

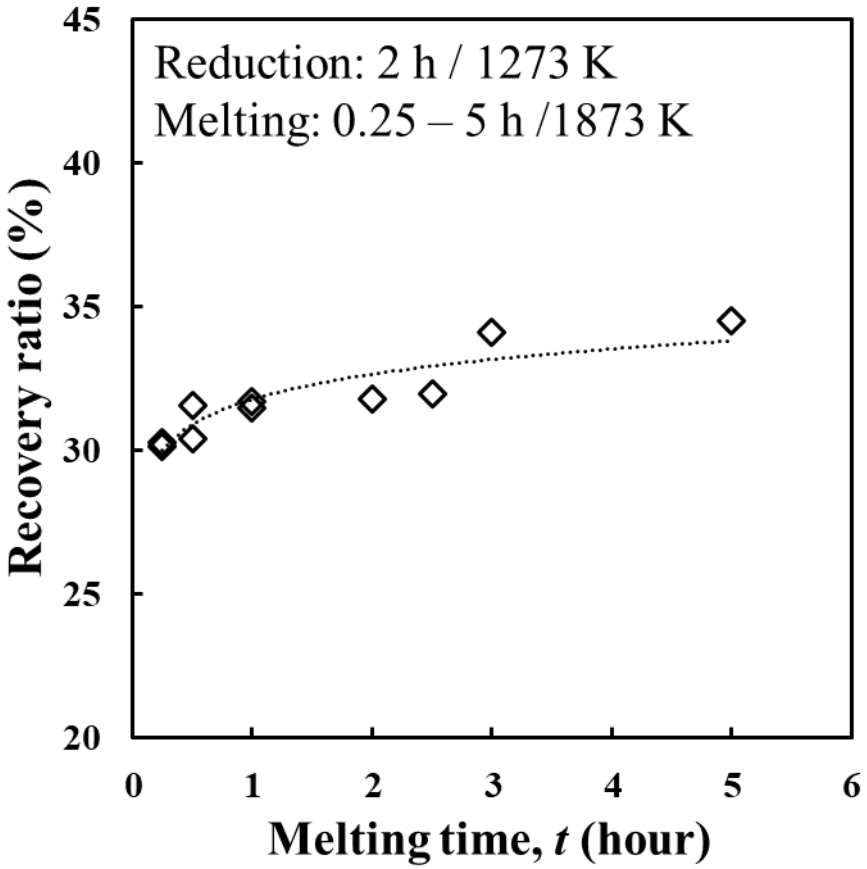

Fig. 4-12 Change in recovery ratio of Fe alloy with melting time at 1873 K under reduction condition of 2 h at 1273 K in Ar–20%H_2 atmosphere.

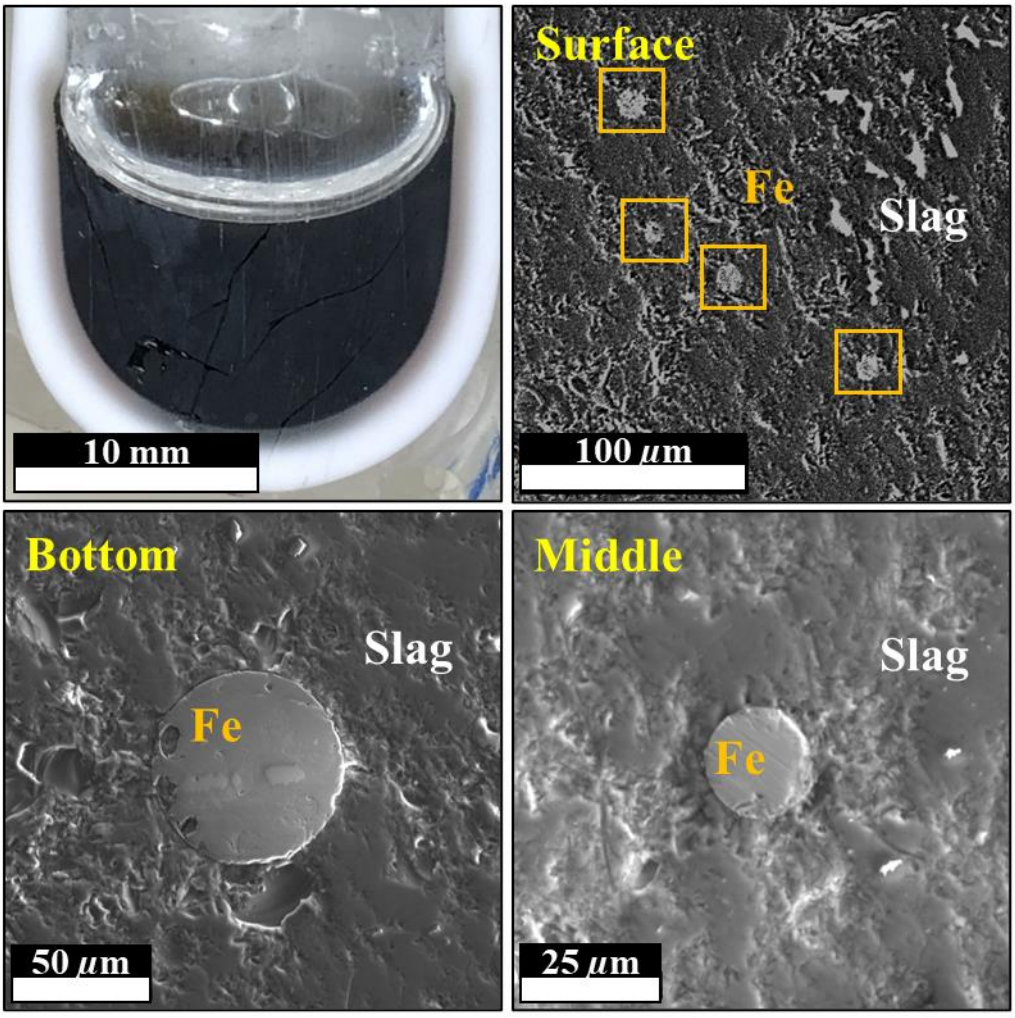

Fig. 4-13 Appearance of the cross-section of the recovered sample and SEM images of fine Fe particles on the surface and the inside of the slag after holding at 1273 K for 2 h in Ar atmosphere without H_2 and melting at 1873 K for 1 h in Ar–20%H_2 atmosphere.

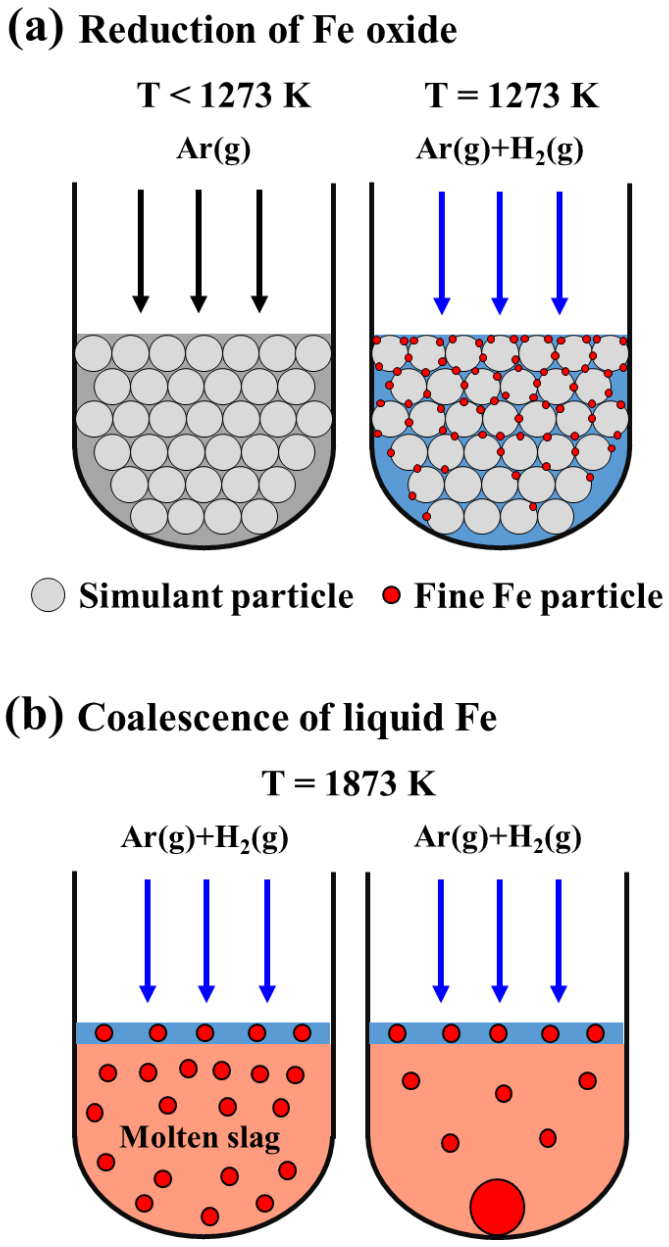

Fig. 4-14 Schematic diagram of the recovery process by H_2. (a) Reduction of lunar regolith simulant to metallic Fe. (b) Coalescence of liquid Fe particles in molten slag.

4.3.3 Effect of Slag Viscosity on Sedimentation of Initial Fe Particles

It was found that the coalescence and sedimentation of Fe particles during the melting step may affect the recovery after the reduction step. The molten slag and liquid metal phases were separated from each other due to the density difference at 1873 K. However, there were still many Fe particles in the molten slag that did not sink to the bottom of the crucible as shown in **Fig. 4-10**. The fine Fe particles are dispersed in the molten slag at 1873 K and gradually settle to the bottom over time. In this case, the terminal velocity of the Fe particles in Stokes' law for particles falling through a stationary liquid at 1873 K was obtained using Eq. (4-2):

$$v_{\mathrm{s}} = \frac{D_p^2(\rho_p - \rho_f)\mathrm{g}}{18\eta} \qquad (4-2)$$

where D_p is the diameter of the Fe particle, ρ_p is the density of Fe, ρ_f is the density of molten slag, g is the acceleration of gravity, and η is the viscosity of the molten slag. The viscosity of the molten slag was found to be 43.62 poise at 1873 K using FactSage, the acceleration of gravity is 9.8 m/s^2, the density of liquid Fe is 7.87 g/cm^3. The density of slag was calculated to be 2.47 g/cm^3 from the additivity of molar volume [10] in **Table 4-4** at 1873 K for the major elements, which are SiO_2, Al_2O_3, CaO, and MgO. The diameter of metallic Fe particles in slag generally ranged from approximately several μm to 10 μm (**Fig. 4-10**).

Figure 4-15 shows the variation in terminal velocity of Fe particles in the molten regolith simulant at 1873 K, as a function of particle diameter, on the Earth and the Moon. For Fe particles with a diameter of 10 μm, the terminal velocities are approximately 0.24 mm/h and 0.04 mm/h on the Earth and the Moon, respectively. These results indicate that considerable time is required for fine Fe particles to settle within the molten slag due to gravity. Therefore, when considering such sedimentation, the gravity conditions of the Moon, it is important to utilize physical properties to enhance the coalescence of such fine particles in the molten slag.

Table 4-4 Molar volumes of pure components (m^3/mol) [10].

Oxide	Temperature (T) dependence of molar volume (m^3/mol)
SiO_2	$27.516\ \{\ 1+1\cdot10^{-4}\ (\ T\ -\ 1773\ )\ \}\cdot10^{-6}$
Al_2O_3	$28.3\ \{\ 1+1\cdot10^{-4}\ (\ T\ -\ 1773\ )\ \}\cdot10^{-6}$
CaO	$20.7\ \{\ 1+1\cdot10^{-4}\ (\ T\ -\ 1773\ )\ \}\cdot10^{-6}$
MgO	$16.1\ \{\ 1+1\cdot10^{-4}\ (\ T\ -\ 1773\ )\ \}\cdot10^{-6}$

T: Temperature (K)

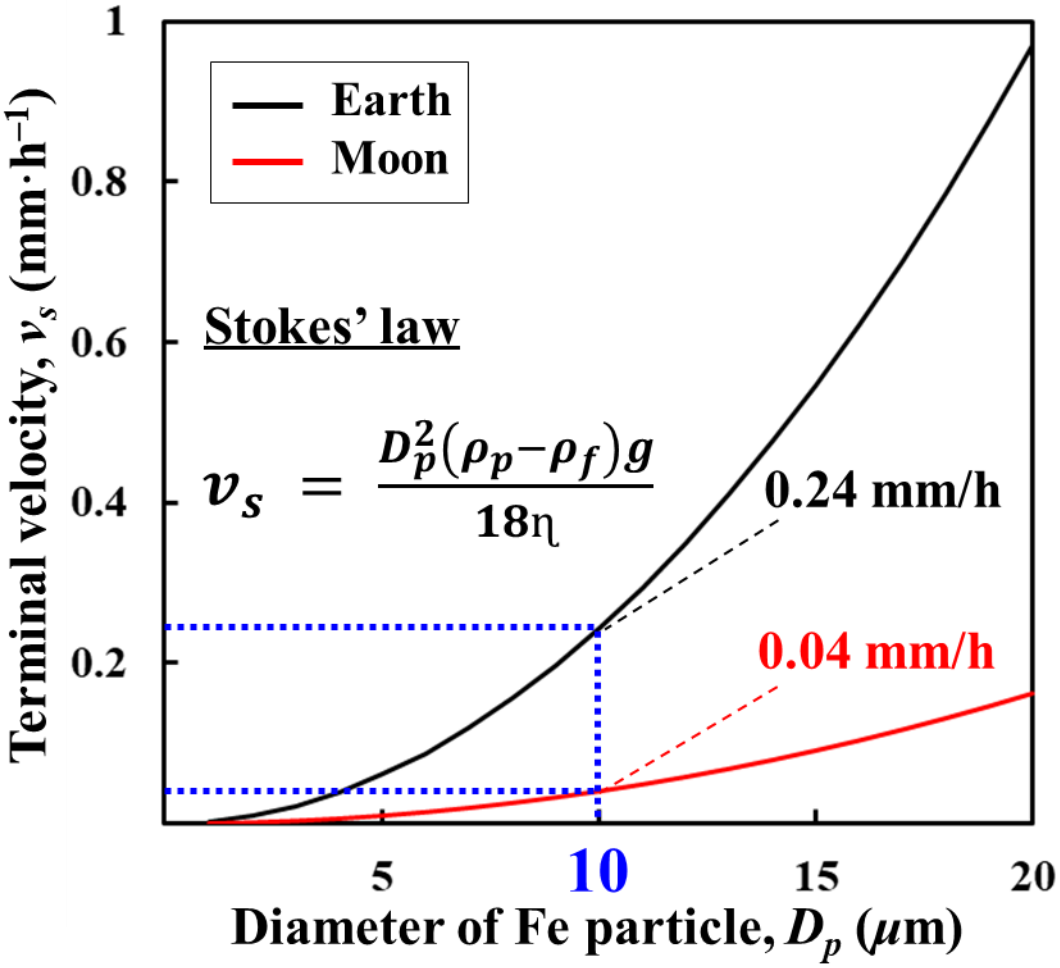

Fig. 4-15 Change in terminal velocity with the diameter of Fe particle in molten slag at 1873 K.

4.4 Summary

In this chapter, high-temperature H_2 reduction and melting experiments were conducted to extract metallic Fe from lunar regolith simulant. Also, thermodynamic calculations were performed to predict the equilibrium phase of regolith simulant at high temperature.

(1) By thermodynamic calculation, it was predicted that Fe oxide in regolith simulant would be reduced to metallic Fe at 1323 K and completely melted at 1773 K under oxygen partial pressure of 10^{-15} atm. Based on thermodynamic predictions, the experimental process was designed and then carried out in two steps: a reduction step at 1273 K (accelerated using H_2) and a melting step at 1873 K.

(2) In the reduction step, change in Fe recovery was investigated after keeping for 1 to 5 h at 1273 K and then melting for 1 h at 1873 K. The Fe recovery changed with reduction time from approximately 24 to 41%, and then the reduction time was determined to be 2 h. Fractional reduction of regolith simulant was investigated from the weight loss of samples before and after the reduction at for 2 h at 1273 K, which was approximately 38.3%.

(3) Spherical Fe alloy of over 3 mm in diameter was sedimented at the bottom of crucible although fine metallic Fe particles (several μm to 10 μm) were still dispersed in the slag phase. Fe recovery was approximately 30% to 35%, which is less than that of reduced Fe. Hence, to enhance recovery efficiency, it is necessary to coalesce the fine metallic Fe particles to increase the sedimentation velocity.

REFERENCES

[1] U. Hegde, R. Balasubramaniam and S. Gokoglu: Development and Validation of a Model for Hydrogen Reduction of JSC-1A, (NASA/Technical Memorandum), (2009), https://ntrs.nasa.gov/citations/20090023167, (accessed 2024-05-28).

[2] U. Hegde, R. Balasubramaniam, S. Gokoglu, K. Rogers, M. Reddington and L. Oryshchyn: Hydrogen Reduction of Lunar Regolith Simulants for Oxygen Production, (NASA/Technical Memorandum), (2011), https://ntrs.nasa.gov/citations/20110008071, (accessed 2024-05-28).

[3] H. M. Sargeant, F. A. J. Abernethy, M. Anand, S. J. Barber, P. Landsberg, S. Sheridan, I. Wright and A. Morse: Planetary and Space Science, 180 (2020), 104759.

[4] H. M. Sargeant, S. J. Barber, M. Anand, F. A. J. Abernethy, S. Sheridan, I.P. Wright and A.D Morse: Planetary and Space Science, 205 (2021), 105287.

[5] M. A. Gibson, C. W. Knudsen, D. J. Brueneman, C. C. Allen, H. Kanamori and D. S. McKay: Journal of Geophysical Research (Planets), 99 (1994), 10887.

[6] C. C. Allen, R. V. Morris and D. S. McKay: Journal of Geophysical Research (Planets), 99 (1994), 23173.

[7] C. C. Allen, R. V. Morris and D. S. McKay: Journal of Geophysical Research (Planets), 101 (1996), 26085.

[8] G. H. Heiken, D. T. Vaniman, and B. M. French: Lunar Source book, Cambridge University Press, New York, (1991), 121.

[9] A.H.C. Sirk, D.R. Sadoway and L. Sibille: The Electrochemical Soc., 28 (2010), 367.

[10] K. C. Mills and B. J. Keene: Int. Materials Reviews, 32 (1987), 1.

Chapter 5

Effect of Wettability on Coalescence of Dispersed Metallic Iron in Molten Lunar Regolith Simulant

5.1 Background

In chapter 4, metallic Fe alloy was successfully extracted from regolith simulant at low oxygen partial pressure using H_2 from both the reduction (step 1) and melting (step 2) processes. Fine Fe particles, forming through reduction in the regolith simulant, were found to be dispersed in the molten slag, and a bulk Fe alloy was sedimented at the bottom of slag probably by the coalescence of these particles. The results from chapter 4 indicated that, under the Moon's low gravity, reducing the viscosity of slag or promoting the coalescence of Fe particles to increase their size was essential for enhancing the recovery of metals.

In chapter 3, it was confirmed that the wettability affects the coalescence of the liquid droplet. When dispersed liquid Fe droplets in molten slag come into contact with each other, poorer wettability is expected to lead to faster drainage of the thin film formed between the droplets, thereby promoting the coalescence of the Fe droplets. In other words, the recovery ratio of Fe alloy may increase due to increasing a sedimentation rate by enhanced coalescence. Conversely, when the wettability between the droplet and slag is better, the recovery ratio may decrease. Since the wetting behavior between molten slag and liquid Fe is sensitive to the molten slag composition, oxide addition is considered to control wettability. In addition, the viscosity of molten slag changes depending on the addition of oxide, and as explained in chapter 1, the change in viscosity affects both the coalescence and sedimentation speed of droplets. Therefore, understanding the effect of viscosity and wettability on coalescence with oxide addition is highly valuable for the design of future lunar metallurgy.

In this chapter, the effect of wettability and viscosity on the coalescence of dispersed liquid Fe particles in molten slag was investigated through the following two approaches.

(1) The effect of added oxides on the recovery of metallic Fe from the regolith simulant was investigated. Specifically, the changes in viscosity of the molten slag on each oxide addition

were calculated using FactSage, and the relationship between viscosity and recovery ratio was determined. The following oxides and minerals were used as additives, focusing on ilmenite ($FeTiO_3$), a mineral abundant in mare regions, and albite ($NaAlSi_3O_8$), common in lunar highlands: TiO_2 (rutile), ilmenite, albite mixture, and $Na_2O{\cdot}xSiO_2$ (where $x = 2$ or 4) compounds.

(2) The effect of wettability between molten slag and liquid Fe on the coalescence of Fe particles was investigated based on the experimental recovery of (1). The effect of wettability on Fe recovery was systematically discussed through evaluation of the contact angle calculated from the Neumann's relation.

5.2 Experimental

5.2.1 Sample Preparation

The lunar regolith simulant was identical to the one used in the experiments in chapter 4. The prepared regolith simulant was uniformly mixed with additional oxides: TiO_2 (rutile), ilmenite, albite, and $Na_2O{\cdot}xSiO_2$ compounds. **Table 5-1** presents the chemical compositions for the experimental samples, both before and after mixing the regolith simulant with oxides. The addition of oxides was based on the composition of regolith simulant: e.g., the addition of TiO_2 was roughly from +50 mass% to +200 mass% based on the amount of TiO_2 contained in the regolith simulant. TiO_2 (rutile) powder reagent (99.0%; Wako., Inc.) and high-purity ilmenite powder (99.8%; Alfa Aesar Co., Inc.) were used. The mineral mixture of $Na_2O{\cdot}1.74Al_2O_3{\cdot}11.25SiO_2$ was used as albite. For the $Na_2O{\cdot}xSiO_2$ compounds, two different samples were prepared: $Na_2O{\cdot}4SiO_2$ and $Na_2O{\cdot}2SiO_2$. $Na_2O{\cdot}4SiO_2$ was prepared by pre-melting after mixing Na_2CO_3 and SiO_2 powder; $Na_2O{\cdot}2SiO_2$ was prepared by calcining sodium silicate powder ($Na_2O{\cdot}2SiO_2{\cdot}xH_2O$) at 773 K for 24 h. In this chapter, $Na_2O{\cdot}4SiO_2$ and $Na_2O{\cdot}2SiO_2$ are referred to as 1N·4S and 1N·2S, respectively, for convenience.

5.2.2 Procedure

Figure 5-1 shows the experimental process designed based on thermodynamic predictions by FactSage. To maintain the continuity of the experiments, all conditions were conducted in the same manner as described in chapter 4. As reported in chapter 4, the extent of reduction of Fe oxide in regolith simulant was approximately 38.3%. The concentration of oxides added was insignificant and was uniformly mixed with the simulant; therefore, a comparable reduction was assumed for all samples. The recovery ratio was obtained using Eq. (4-1) as described in chapter 4. In the case of ilmenite addition, Fe in the ilmenite was also considered in the original sample in Eq. (4-1) of chapter 4.

Table 5-1 Chemical compositions of slag for different experimental conditions.

Component (mass%)	No.	Addition	SiO_2	CaO	Al_2O_3	MgO	FeO	Fe_2O_3	TiO_2	Na_2O	Bal.
Regolith simulant	A0	-	49.60	9.45	16.90	5.62	6.13	6.53	1.53	2.61	1.63
TiO_2 (Rutile)	A1	+50%TiO_2	49.21	9.38	16.77	5.58	6.08	6.48	2.31	2.59	1.62
	A2	+100%TiO_2	48.82	9.30	16.63	5.53	6.03	6.43	3.08	2.57	1.60
	A3	+150%TiO_2	48.44	9.23	16.50	5.49	5.99	6.38	3.84	2.55	1.59
	A4	+200%TiO_2	48.06	9.16	16.38	5.45	5.94	6.33	4.58	2.53	1.58
Ilmenite	B1	+50%TiO_2	48.90	9.32	16.66	5.54	6.71	6.44	2.25	2.57	1.61
	B2	+100%TiO_2	48.23	9.19	16.43	5.46	7.27	6.35	2.95	2.54	1.58
	B3	+150%TiO_2	47.57	9.06	16.21	5.39	7.82	6.26	3.63	2.50	1.56
	B4	+200%TiO_2	46.93	8.94	15.99	5.32	8.35	6.18	4.29	2.47	1.54
Albite	C1	+2%SiO_2	49.95	9.31	16.94	5.54	6.04	6.44	1.51	2.67	1.61
	C2	+4%SiO_2	50.29	9.18	16.97	5.46	5.96	6.35	1.49	2.73	1.58
	C3	+6%SiO_2	50.61	9.05	17.00	5.38	5.87	6.26	1.47	2.78	1.56
	C4	+8%SiO_2	50.93	8.93	17.04	5.31	5.79	6.17	1.45	2.84	1.54
	C5	+10%SiO_2	51.25	8.81	17.07	5.24	5.71	6.09	1.43	2.89	1.52
$Na_2O{\cdot}4SiO_2$	D1	+15%Na_2O	50.18	9.27	16.58	5.51	6.01	6.41	1.50	2.93	1.60
	D2	+30%Na_2O	50.73	9.10	16.28	5.41	5.90	6.29	1.47	3.24	1.57
	D3	+45%Na_2O	51.27	8.94	15.98	5.31	5.80	6.17	1.45	3.54	1.54
	D4	+60%Na_2O	51.79	8.78	15.70	5.22	5.69	6.06	1.42	3.83	1.51
$Na_2O{\cdot}2SiO_2$	E1	+25%Na_2O	49.91	9.27	16.58	5.51	6.01	6.41	1.50	3.20	1.60
	E2	+50%Na_2O	50.20	9.10	16.28	5.41	5.90	6.29	1.47	3.77	1.57
	E3	+75%Na_2O	50.49	8.94	15.98	5.31	5.80	6.17	1.45	4.32	1.54
	E4	+100%Na_2O	50.77	8.78	15.70	5.22	5.69	6.06	1.42	4.85	1.51

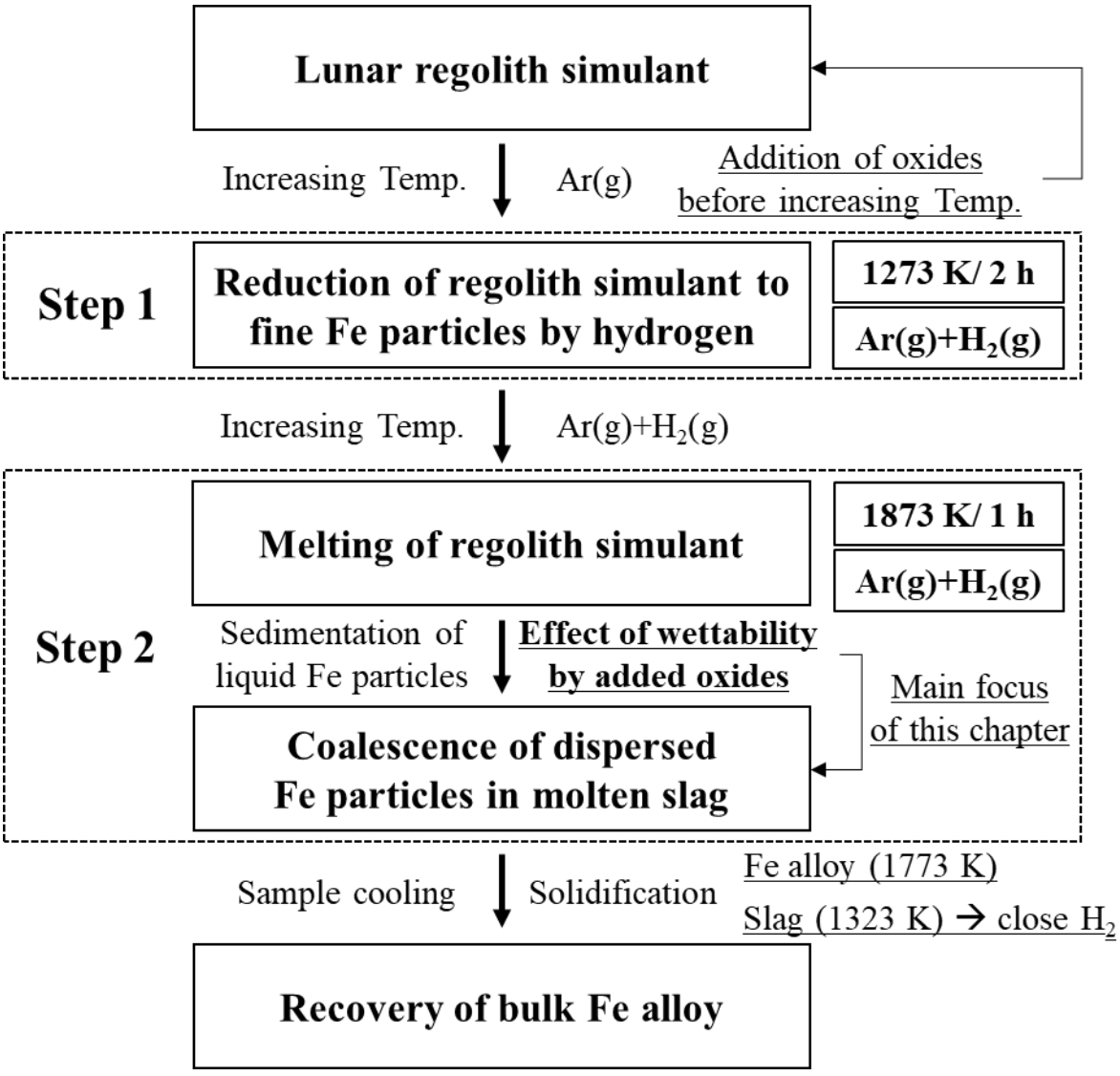

Fig. 5-1 Conceptual flowsheet of experimental process steps.

5.3 Results and Discussion

5.3.1 Effect of Additive Oxides on Fe Recovery

a. Effect of Addition of TiO_2 to Regolith Simulant

Figure 5-2 shows the variation in Fe recovery and viscosity of molten slag with the addition of oxides. The addition of oxides results in changes in the viscosity. Since metallic Fe was recovered from molten slag by gravity, the changes in recovery ratio due to oxide addition were considered in terms of the change in viscosity. Here, the viscosity of molten slag was calculated by FactSage 8.2 from the composition at 1873 K at an oxygen partial pressure of 10^{-15} atm for each experimental condition.

Figure 5-2(a) shows the variation in Fe recovery and viscosity of molten slag as a function of the amount of added TiO_2 to the regolith simulant under 2 h of reduction at 1273 K and 1 h of melting at 1873 K. The Fe recovery tended to decrease linearly with increase of TiO_2 content, and the viscosity also appeared to decrease. The decrease in viscosity with increasing TiO_2 content agrees well with the research conducted by Nakamoto et al. [1]. When considering the relationship between viscosity and recovery ratio, the decrease in the viscosity of molten slag is advantageous for metal recovery in the process by gravity separation. Additionally, TiO_2 may also positively contribute to the reduction of Fe oxides. It was reported that TiO_2 promotes the reduction of Fe oxides to Fe under a controlled gas atmosphere ($CO/CO_2/H_2/N_2$) [2]. Therefore, the addition of TiO_2 to regolith simulant could increase the recovery ratio by increasing the reduction rate in the reduction step. However, **Figure 5-2(a)** showed a decrease in the recovery ratio despite the decreasing viscosity and the possibility of TiO_2 contributing positively to the reduction. These results suggest that the decrease in recovery is not solely due to slag viscosity.

b. Effect of Addition of Ilmenite to Regolith Simulant

Figure 5-2(b) shows the variation in Fe recovery and the molten slag viscosity with the ilmenite addition. Fe recovery decreased with the ilmenite addition, as shown in **Fig. 5-2(b)**; where the molten slag viscosity also decreased. In general idea, a low slag viscosity can promote the sedimentation and the coalescence of Fe particles, thereby increasing the recovery ratio. However, the correlation between Fe recovery and the molten slag viscosity in **Fig. 5-2(b)** is not in agreement with such a trend.

c. Effect of Addition of Albite to Regolith Simulant

Figure 5-2(c) shows the variation of Fe recovery and the molten slag viscosity with the albite addition. As the amount of albite increased, the Fe recovery remained constant while the molten slag viscosity increased. From the perspective of coalescence and sedimentation of Fe particles by taking into account the viscosity of molten slag, the relationship presented in **Fig. 5-2(c)** is not reasonable.

d. Effect of Addition of $Na_2O{\cdot}xSiO_2$ Compounds to Regolith Simulant

Figures 5-2(d) and 5-2(e) show the analogous data with the addition of 1N·4S and 1N·2S, respectively. These results indicate that both the Fe recovery and molten slag viscosity increased with the increasing amounts of these compounds. As discussed in sections 5.3.1 a, b and c, this behavior is not explained by the trend of slag viscosity with addition of $Na_2O{\cdot}xSiO_2$ compounds.

Figure 5-3 presents a comparison of the combined results showing the variations in Fe recovery with slag viscosity for each oxide addition. Given that low viscosity in molten slag is beneficial for recovering metal particles through gravity separation, the behavior of Fe recovery shown in **Fig. 5-3** cannot be explained from the variation in slag viscosity. This suggests that a more significant factor affects the Fe recovery. Therefore, it is reasonable to assume that the influence of oxide addition on the coalescence of fine Fe particles can be attributed to changes in wettability, as described in chapter 3. In the following section, the changes in wettability due to the addition of oxides and the methods used to evaluate these changes are discussed.

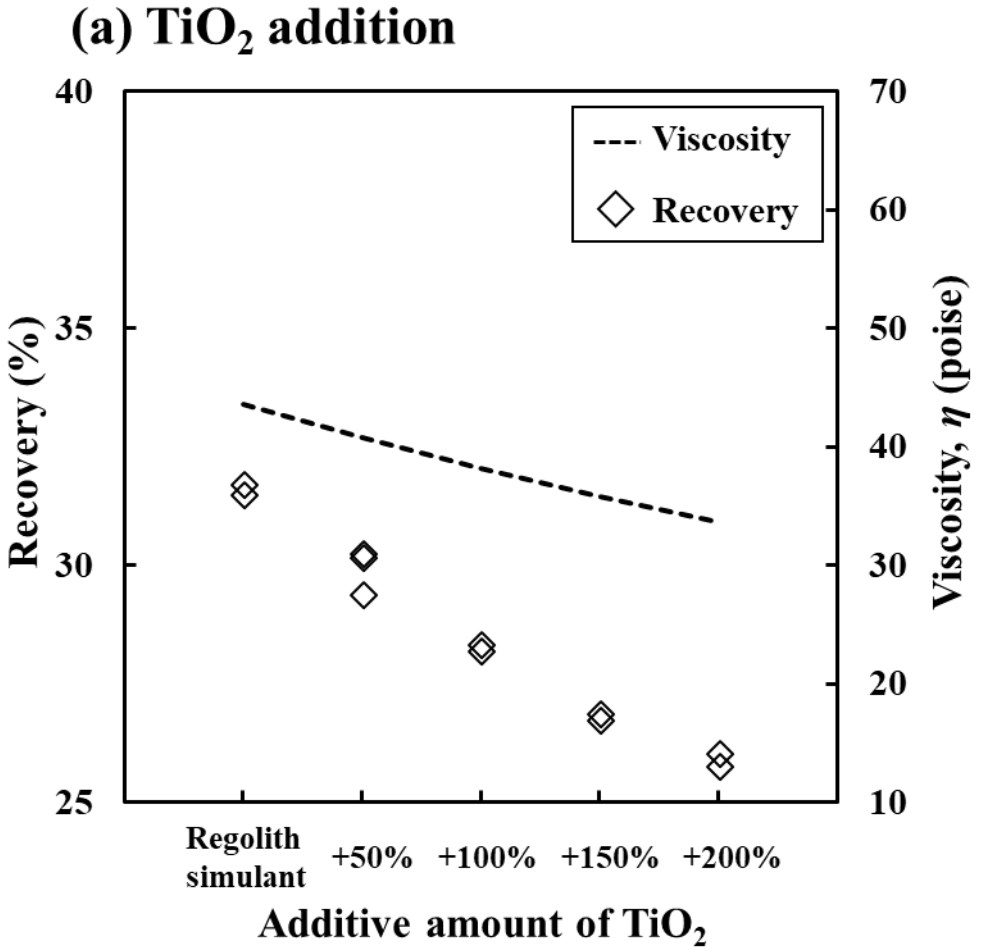

Fig. 5-2 Variation in the recovery of Fe alloy and the viscosity of molten slag with an additive added to the regolith simulant after 2 h of reduction at 1273 K and 1 h of melting at 1873 K.

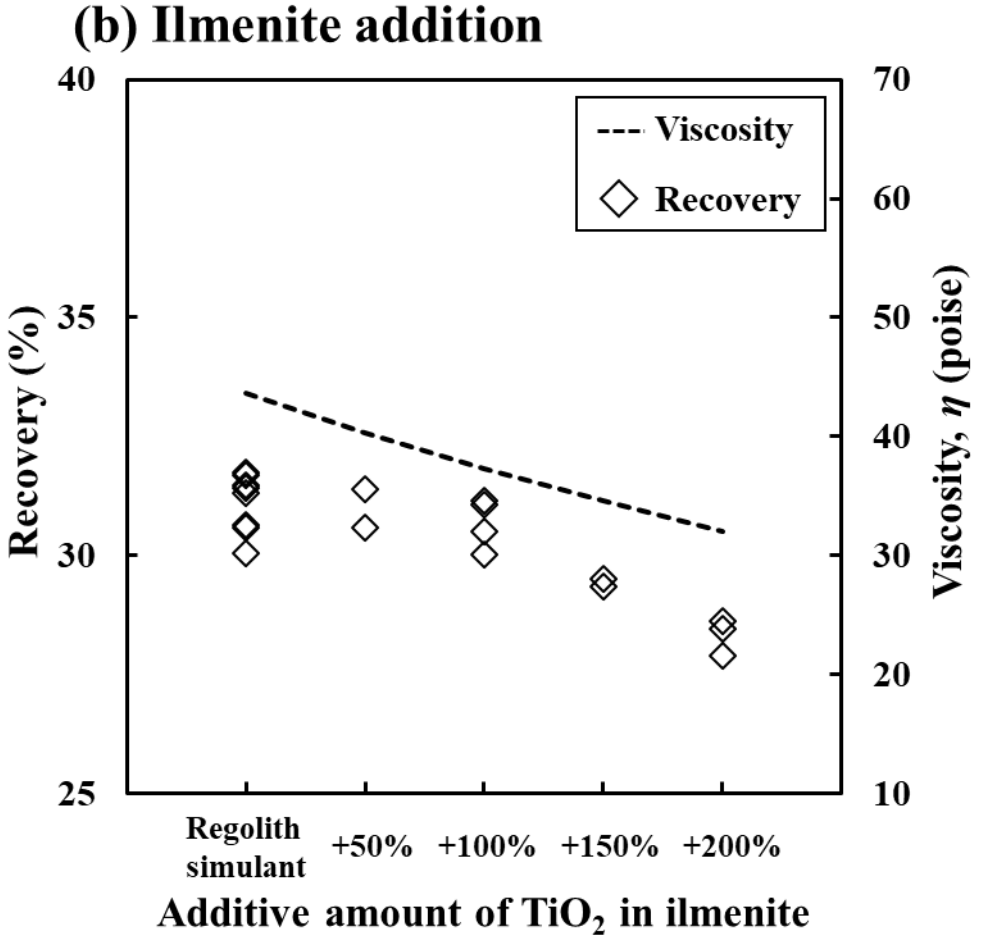

Fig. 5-2 Variation in the recovery of Fe alloy and the viscosity of molten slag with an additive added to the regolith simulant after 2 h of reduction at 1273 K and 1 h of melting at 1873 K. (Cont.)

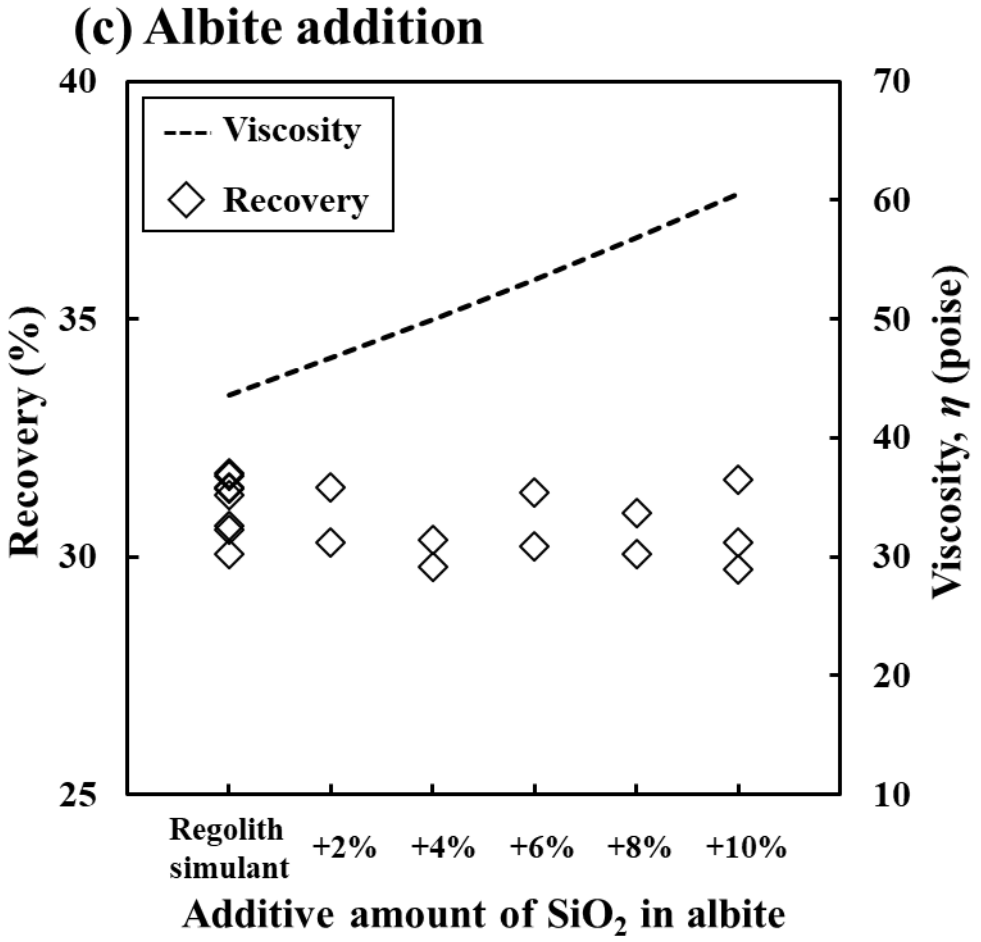

Fig. 5-2 Variation in the recovery of Fe alloy and the viscosity of molten slag with an additive added to the regolith simulant after 2 h of reduction at 1273 K and 1 h of melting at 1873 K. (Cont.)

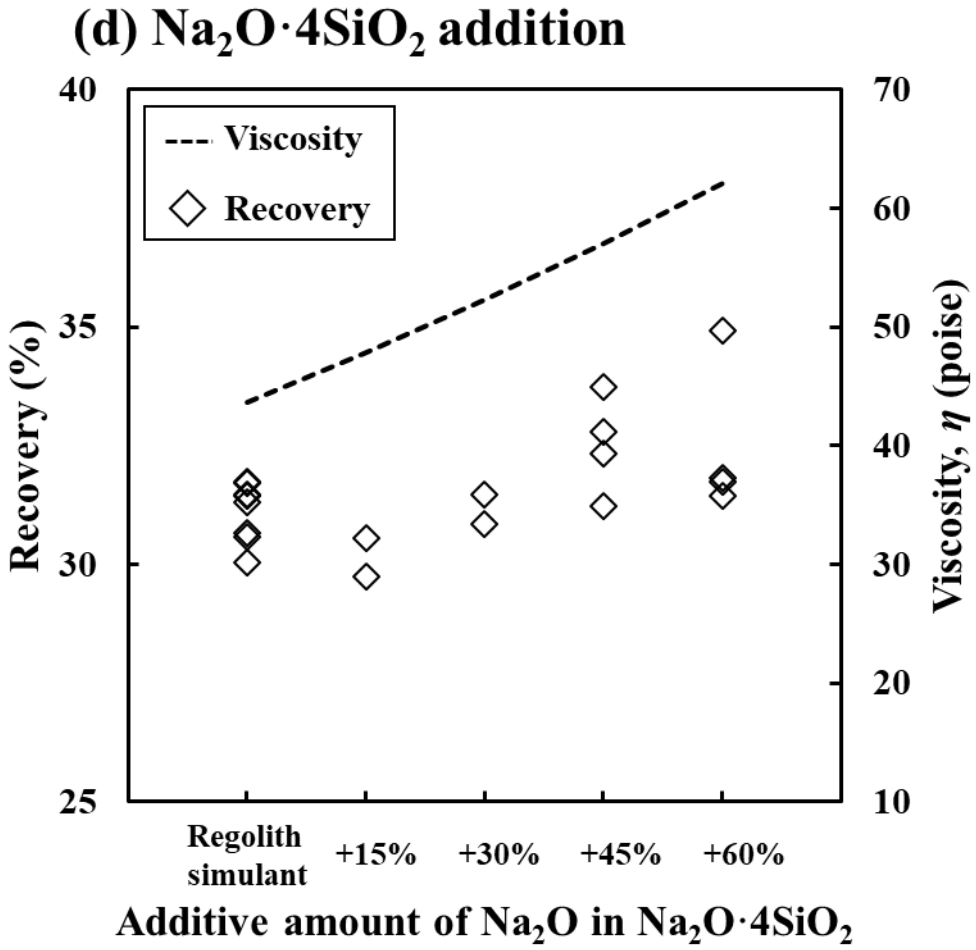

Fig. 5-2 Variation in the recovery of Fe alloy and the viscosity of molten slag with an additive added to the regolith simulant after 2 h of reduction at 1273 K and 1 h of melting at 1873 K. (Cont.)

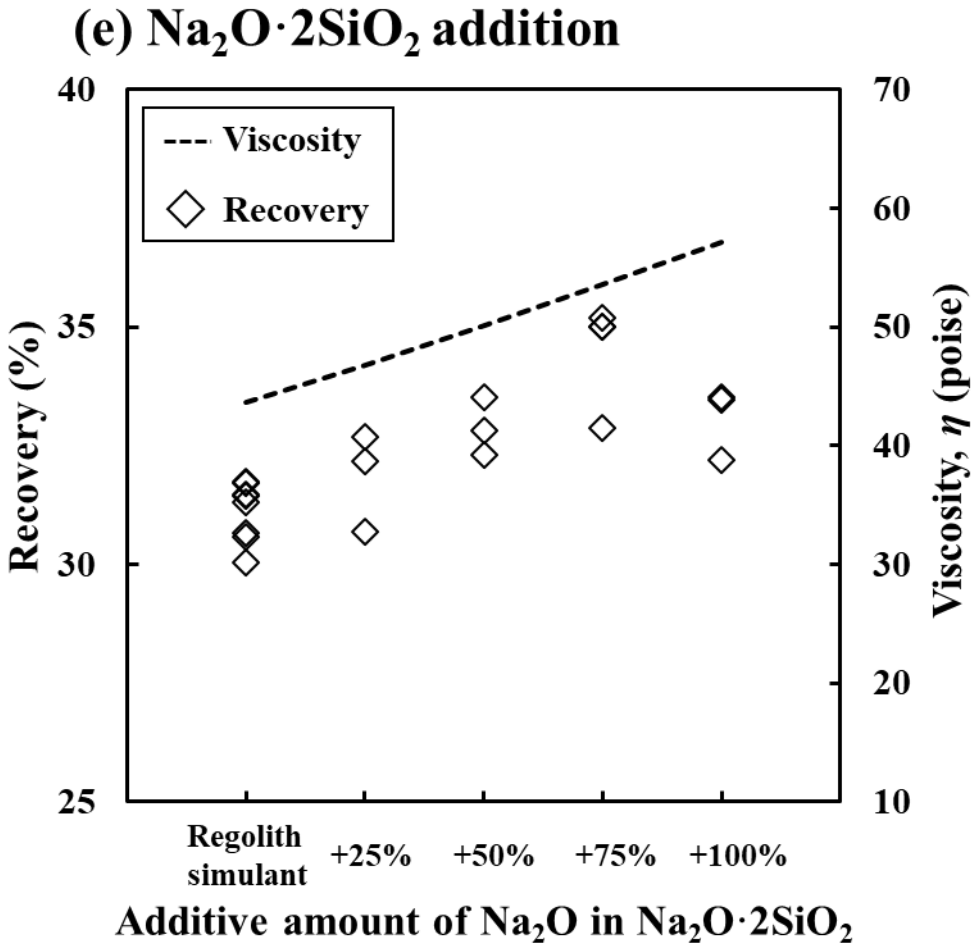

Fig. 5-2 Variation in the recovery of Fe alloy and the viscosity of molten slag with an additive added to the regolith simulant after 2 h of reduction at 1273 K and 1 h of melting at 1873 K. (Cont.)

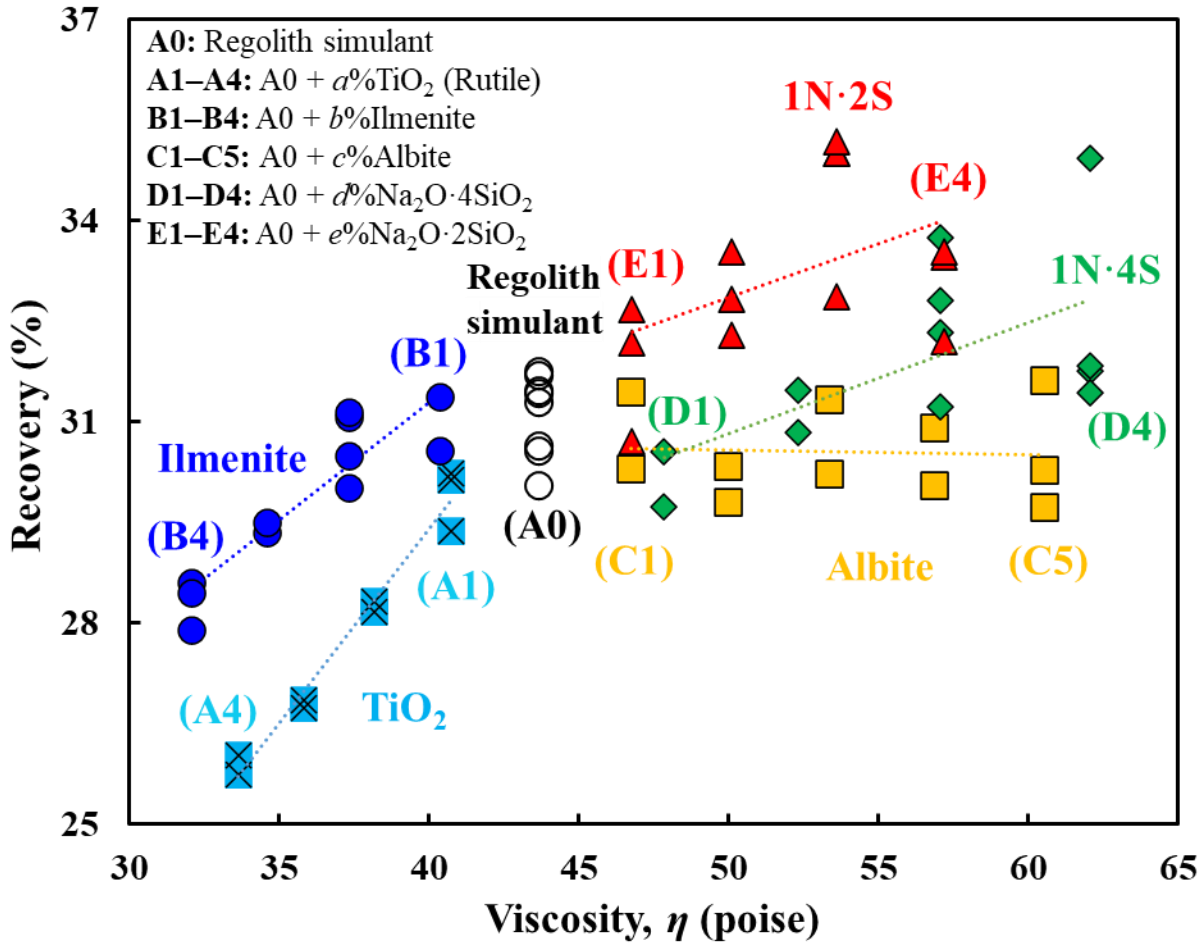

Fig. 5-3 Comparison of the slag compositions for the variations in Fe recovery with the viscosity.

5.3.2 Evaluation of Wettability at Interface between Molten Slag and Liquid Fe

The wettability of different oxides on liquid Fe was evaluated by Neumann's relation [3]. **Figure 5-4** illustrates the balance of forces at the triple point, showing the surface tension of liquid Fe (σ_{Fe}), the surface tension of the molten slag (σ_{slag}), and the interfacial tension between the two phases ($\sigma_{Fe/slag}$). θ is the contact angle between the molten slag and liquid Fe, and α is the apparent contact angle. In this study, wettability is defined by the size of the contact angle (θ) in **Fig. 5-4**. Based on Neumann's relation, equation (5-1) is derived.

$$\left[\sigma_{\mathrm{Fe/slag}}\right]^2 = \left[\sigma_{\mathrm{Fe}}\right]^2 + \left[\sigma_{\mathrm{slag}}\right]^2 - 2\sigma_{\mathrm{Fe}} \cdot \sigma_{\mathrm{slag}} \cdot \cos\alpha \qquad (5-1)$$

Additionally, Eq. (5-2) is obtained from the balance of forces in the vertical direction:

$$\sigma_{\mathrm{Fe/slag}} \cdot \sin(\theta - \alpha) = \sigma_{\mathrm{slag}} \cdot \sin\alpha \qquad (5-2)$$

Once the values of $\sigma_{Fe/slag}$, σ_{Fe}, and σ_{slag} are obtained, the contact angle can be calculated from Eqs. (5-1) and (5-2). The samples selected in **Table 5-1** for the wettability evaluation are as follows: Regolith simulant (A0), +200%TiO_2 (A4), +200%TiO_2 of ilmenite (B4), +10%SiO_2 of albite (C5), +60%Na_2O of 1N·4S (D4), and +100%Na_2O of 1N·2S (E4). **Table 5-2** shows the chemical compositions of the slags in the samples (A0, A4, B4, C5, D4, E4) recovered after the reduction-melting process, as analyzed by scanning electron microscopy with energy-dispersive X-ray spectroscopy (SEM-EDX).

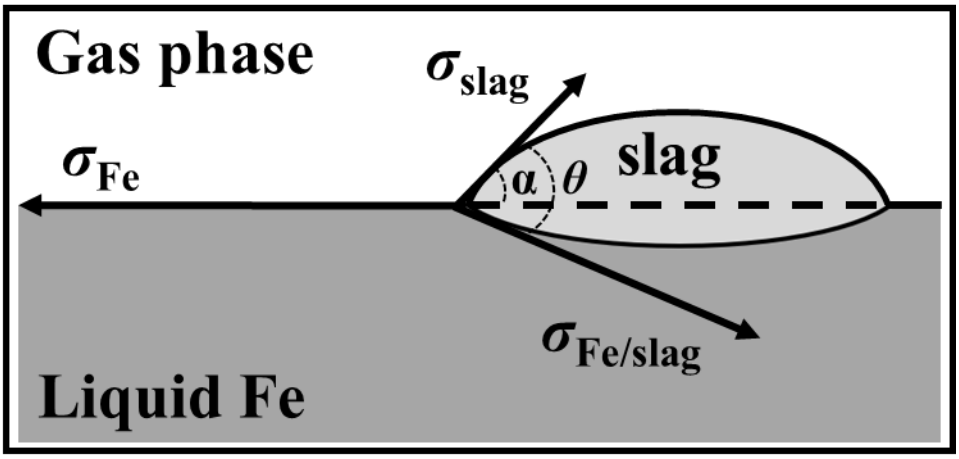

Fig. 5-4 Schematic diagram of a droplet of molten slag on surface of liquid Fe, indicating the balance of forces at the triple point.

Table 5-2 Chemical compositions of slags collected after melting experiments obtained by scanning electron microscopy with energy-dispersive X-ray spectroscopy and equilibrium oxygen contents of liquid Fe for different experimental compositions.

No.	Slag composition							[mass%O]*
	SiO_2	CaO	Al_2O_3	MgO	Na_2O	FeO	TiO_2	
R. S (A0)	47.64	11.11	21.04	5.85	3.27	9.08	2.02	2.30×10^{-2}
TiO_2 (A4)	47.10	10.41	18.62	5.56	2.12	9.71	6.47	2.20×10^{-2}
Ilmenite (B4)	46.10	11.53	17.96	5.08	2.71	11.69	4.93	2.98×10^{-2}
Albite (C5)	50.89	8.84	21.06	6.10	4.18	7.39	1.53	1.79×10^{-2}
1N·4S (D4)	51.30	9.46	21.01	5.24	5.14	6.03	1.82	1.58×10^{-2}
1N·2S (E4)	50.87	8.76	21.70	5.19	6.25	5.67	1.55	1.65×10^{-2}

*Oxygen content [mass%O] in liquid Fe predicted by FactSage.

5.3.3 Evaluation of Surface Tension of Liquid Fe

The surface tension of pure liquid iron is significantly reduced even by trace concentrations of dissolved impurities (such as oxygen, sulfur, selenium, and tellurium) in the liquid iron [3,4]. Impurities such as oxygen and sulfur act as surface-active components, adsorbing to the surface of the liquid iron and reducing its surface tension. In this study, only oxygen was considered as an impurity of liquid Fe in molten regolith simulant, while other potential impurities were excluded. Since the presence of FeO in molten slag leads to an increase in the oxygen content in liquid Fe, the surface tension of liquid Fe is strongly affected by FeO activity in slag [3]. Ogino et al. [5] empirically derived the following relationship from the Gibbs-Langmuir adsorption equation [6] to consider the effect of oxygen concentration in liquid Fe at 1873 K.

$$\sigma_{\mathrm{Fe}} = 1910 - 825\log(1 + 210[\mathrm{mass\%O}])\ (\mathrm{mN/m}) \qquad (5-3)$$

The oxygen content in liquid Fe, [mass%O], was estimated from the following relationship:

$$\mathrm{Fe_{(l)}} + \mathrm{O}\ [\mathrm{mass\%}] = \mathrm{FeO_{(l)}} \qquad (5-4)$$

Activity of FeO was obtained from the slag composition by FactSage. [mass%O] for each experimental condition, which was obtained by Eq. (5-4) and FactSage calculation, is presented in **Table 5-2**. The surface tension (σ_{Fe}) of the liquid Fe was calculated by Eq. (5-3) for each condition using [mass%O] in **Table 5-2**.

5.3.4 Evaluation of Surface Tension of Molten Slag

The model developed by Tanaka et al. [7], based on the Butler's equation [8], was applied to the seven-component SiO_2–CaO–Al_2O_3–MgO–Na_2O–FeO–TiO_2 system to evaluate the surface tension of ionic mixtures. The surface tension of the molten slag was calculated by Eq. (5-5):

$$\sigma = \sigma_i^{\mathrm{Pure}} + \frac{RT}{A_i}\ln\frac{M_i^{\mathrm{Surf}}}{M_i^{\mathrm{Bulk}}} \qquad (5-5)$$

where

$$M_i^{\mathrm{P}} = \frac{\frac{R_{\mathrm{A}}}{R_{\mathrm{X}}} \cdot \mathrm{N}_i^P}{\frac{R_{\mathrm{Si^{4+}}}}{R_{\mathrm{SiO_4^{4-}}}} \cdot N_{\mathrm{SiO_2}}^{\mathrm{P}} + \frac{R_{\mathrm{Ca^{2+}}}}{R_{\mathrm{O^{2-}}}} \cdot N_{\mathrm{CaO}}^{\mathrm{P}} + \frac{R_{\mathrm{Al^{3+}}}}{R_{\mathrm{O^{2-}}}} \cdot N_{\mathrm{Al_2O_3}}^{\mathrm{P}} + \frac{R_{\mathrm{Mg^{2+}}}}{R_{\mathrm{O^{2-}}}} \cdot N_{\mathrm{MgO}}^{\mathrm{P}} + \frac{R_{\mathrm{Na^{+}}}}{R_{\mathrm{O^{2-}}}} \cdot N_{\mathrm{Na_2O}}^{\mathrm{P}} + \frac{R_{\mathrm{Fe^{2+}}}}{R_{\mathrm{O^{2-}}}} \cdot N_{\mathrm{FeO}}^{\mathrm{P}} + \frac{R_{\mathrm{Ti^{4+}}}}{R_{\mathrm{O^{2-}}}} \cdot N_{\mathrm{TiO_2}}^{\mathrm{P}}} \quad (5-6)$$

Subscript *i* refers to the following components: SiO_2, CaO, Al_2O_3, MgO, Na_2O, FeO, or TiO_2. Subscripts A and X refer to the cations and anions of component *i*, respectively. Superscripts "Surf" and "Bulk" indicate the surface and bulk, respectively. *R* is the gas constant, *T* is the absolute temperature, and σ_i^{Pure} is the surface tension of pure molten component *i*, which is treated as a model parameter. $A_i = N_0^{1/3} \cdot V_i^{2/3}$ corresponds to the molar surface area in a monolayer of pure molten component *i* (N_0: Avogadro's number, V_i: molar volume of pure molten component *i*). N_i^P is the mole fraction of component *i* in phase P (P = Surf or Bulk). R_{A} is the radius of the cation, and R_{X} is the radius of the anion; for example, in the case of the SiO_2–CaO–Al_2O_3–MgO–Na_2O–FeO–TiO_2 system.

$$R_{\mathrm{A}} = R_{\mathrm{Si^{4+}}}, R_{\mathrm{Ca^{2+}}}, R_{\mathrm{Al^{3+}}}, R_{\mathrm{Mg^{2+}}}, R_{\mathrm{Na^{+}}}, R_{\mathrm{Fe^{2+}}}, R_{\mathrm{Ti^{4+}}} \quad (5-7)$$

$$R_{\mathrm{X}} = R_{\mathrm{SiO_4^{4-}}}, R_{\mathrm{O^{2-}}} \quad (5-8)$$

where $\mathrm{SiO_4^{4-}}$ is considered to be the minimum anionic unit in SiO_2, and the value of $R_{\mathrm{Si^{4+}}}/R_{\mathrm{SiO_4^{4-}}}$ was empirically determined to be 0.5 [7,9-11]. This model can be widely applied to a variety of molten slags because it is based only on the surface tension, molar volume, and ionic radii of the pure components in the system [7,9-16]. The above Eq. (5-5) have been derived from Butler's equation [8] by considering the following assumptions [I] and [II].

[I] It is well known that molten ionic mixtures readily undergo surface relaxation processes, such as the spontaneous changes in ionic distance at the surface, enabling the energetic state of the surface to approach the bulk state. Thus, the contribution from excess Gibbs energy terms is neglected in Butler's equation.

[II] In ionic substances, it is well known that the ionic structures depend upon the ratio of the cationic to anionic radii. In order to evaluate the ionic structures and physicochemical properties of ionic materials, the ratio of the cationic and anionic radii should be considered.

Information on ionic radii was obtained from Shannon [17] and Ikemiya et al. [18], while the molar volumes of the pure oxides provided by Mills and Keene [19] were utilized. These values are listed in **Tables 5-3** and **5-4**, respectively. The temperature dependence of the surface tension for pure SiO_2 was taken from the NIST database for the calculations in this study [20]. The temperature dependences of surface tensions for pure CaO, Al_2O_3, MgO, FeO, and Na_2O, as evaluated in previous studies [9-11], were applied; that for pure TiO_2 was obtained by fitting data from literature and using extrapolation [21]. The equations for determining the temperature dependences of surface tension are listed in **Table 5-5** [9-11,20,21]. The surface tension (σ_{slag}) of the molten slag was calculated by Eq. (5-5) for each experimental condition.

Table 5-3 Ionic radii of cations and oxygen ion [17,18].

Ion	Radius (10^{-1} nm)
Si^{4+}	0.42
Ca^{2+}	0.99
Al^{3+}	0.51
Mg^{2+}	0.66
Na^{+}	0.97
Fe^{2+}	0.74
Ti^{4+}	0.61
O^{2-}	1.44

Table 5-4 Molar volumes of pure components [19].

Oxide	Temperature (T) dependence of molar volume (m^3/mol)
SiO_2	$27.516\{1+1\cdot10^{-4}\,(T-1773)\}\cdot10^{-6}$
CaO	$20.7\{1+1\cdot10^{-4}\,(T-1773)\}\cdot10^{-6}$
Al_2O_3	$28.3\{1+1\cdot10^{-4}\,(T-1773)\}\cdot10^{-6}$
MgO	$16.1\{1+1\cdot10^{-4}\,(T-1773)\}\cdot10^{-6}$
Na_2O	$33.0\{1+1\cdot10^{-4}\,(T-1773)\}\cdot10^{-6}$
FeO	$15.8\{1+1\cdot10^{-4}\,(T-1773)\}\cdot10^{-6}$
TiO_2	$24.0\{1+1\cdot10^{-4}\,(T-1773)\}\cdot10^{-6}$

T: Temperature (K)

Table 5-5 Temperature dependence of surface tension of pure components [9-11,20,21].

Oxide	Temperature (T) dependence of surface tension (mN/m)
SiO_2	$243.2 + 0.031 \cdot T$
CaO	$791 - 0.0935 \cdot T$
Al_2O_3	$1024 - 0.177 \cdot T$
MgO	$1770 - 0.636 \cdot T$
Na_2O	$438 - 0.116 \cdot T$
FeO	$504 + 0.0984 \cdot T$
TiO_2	$724.51 - 0.174 \cdot T$

T: Temperature (K)

5.3.5 Evaluation of Interfacial Tension between Molten Slag and Liquid Fe

Interfacial tension is a function of the composition of slag and metal, decreasing as the silica content in the slag increases and as the oxygen and sulfur content in the metal increases [3]. Various numerical models have been proposed to calculate the interfacial tension between two immiscible liquids [3]. Girifalco and Good [22] introduced the ratio (Φ) of adhesion energy to cohesion energy for calculating interfacial tension. In this study, equation (5-9) developed by Girifalco and Good [22] was applied to the molten slag-liquid Fe system for evaluation of interfacial tension ($\sigma_{Fe/slag}$).

$$\sigma_{Fe/slag} = \sigma_{Fe} + \sigma_{slag} - 2\Phi\left(\sigma_{Fe} \cdot \sigma_{slag}\right)^{0.5} \qquad (5-9)$$

where the interaction coefficient Φ represents the ratio corresponding to adhesion ($\Delta G^{a}_{Fe/slag}$) and cohesion (ΔG^{c}_{Fe}, ΔG^{c}_{slag}) for the two liquid phases [3]. Φ approaches zero when interaction between the phases is absent, and increases as the attraction between phases strengthens [3]. Experimental data for the calculation of Φ for the seven-component molten slag were collected from the literature [23-27], and the slag compositions and temperatures that were collected are listed in **Table 5-6**. Systems containing oxygen or sulfur in the liquid Fe and one of FeO, TiO_2, or Na_2O in the molten slag were included, considering the chemical composition of the regolith simulant. Based on the form of the equation proposed by Cramb and Jimbo [3], equation (5-10) was developed here for calculation of Φ for the seven-component molten slag by regression analysis of the values obtained from the data in **Table 5-6**.

$$\Phi = 0.002904(\%SiO_2) + 0.006573(\%CaO) + 0.001325(\%Al_2O_3) + 0.005500(\%MgO) + 0.007164(\%Na_2O) + 0.013557(\%FeO) + 0.005897(\%TiO_2) \qquad (5-10)$$

The Φ value obtained by Eq. (5-10) was applied to the following Eq. (5-11) suggested by Cramb and Jimbo [3] for the consideration of the effect of oxygen on FeO in molten slag.

$$\Phi_{(2)} = \Phi_{(1)} + \frac{\left(0.82 - \Phi_{(1)}\right) \cdot (\%FeO)}{100} \qquad (5-11)$$

where $\Phi_{(2)}$ is the Φ value of the system after FeO addition, and $\Phi_{(1)}$ is the Φ value calculated by regression. The accuracy and applicability of Eq. (5-11) were validated by comparing the experimentally measured and calculated values. **Figure 5-5** shows a comparison between the measured and calculated interfacial tensions, showing the good agreement. Therefore, the interfacial tension ($\sigma_{Fe/slag}$) was calculated by Eq. (5-9) for each condition using $\Phi_{(2)}$.

Table 5-6 Systems and temperatures used for evaluation of interaction coefficient Φ.

System	Temperature (K)	Ref.
SiO_2–CaO–FeO	1873	23, 24
SiO_2–CaO–Al_2O_3–FeO	1853, 1873	23, 25, 26
SiO_2–CaO–Al_2O_3–Na_2O	1873	23
SiO_2–CaO–Al_2O_3–FeO–Na_2O	1873	23
SiO_2–CaO–Al_2O_3–MgO–FeO	1873	25
SiO_2–CaO–Al_2O_3–MgO–TiO_2	1873	27

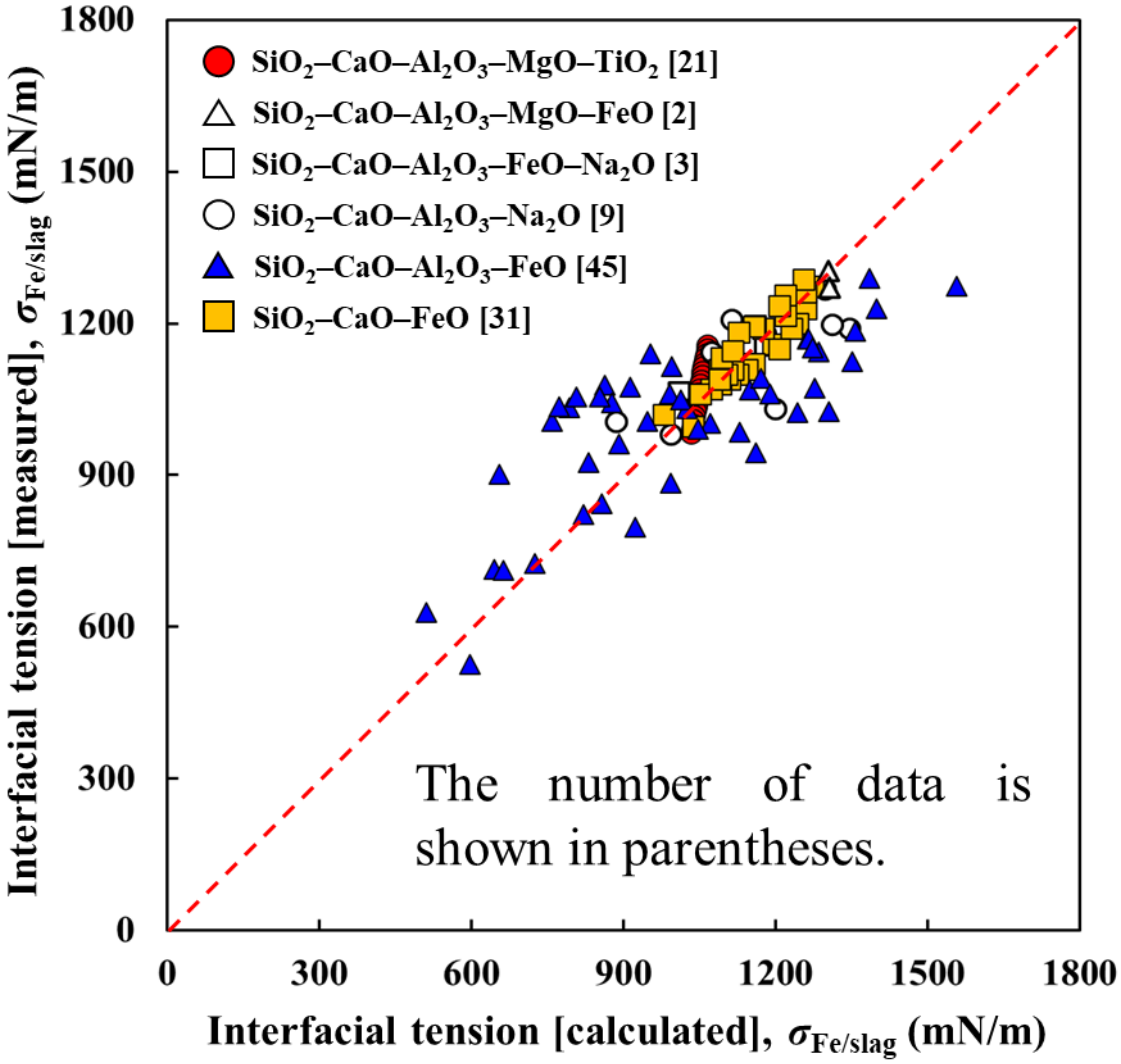

Fig. 5-5 Comparison of measured interfacial tensions with values calculated by Eq. (5-9).

5.3.6 Relationship between Wettability and Fe Recovery

Table 5-7 presents all calculated values of surface tensions (σ_{Fe}, σ_{slag}), interfacial tension ($\sigma_{Fe/slag}$), apparent contact angle (α), and contact angle (θ) for each experimental condition. The surface tension of liquid Fe (1200–1386 mN/m) and the interfacial tension between liquid Fe and molten slag (892–1148 mN/m) vary with the additive oxide more than the surface tension of molten slag (352–379 mN/m) does. The adsorption of oxygen at the surface of iron and the interface between liquid Fe and molten slag, which are determined by the concentration of oxygen in Fe, significantly decreases the surface tension and the interfacial tension, respectively [4,5]. The surface tension of liquid Fe decreases with the additive oxide (ilmenite) which increases the concentration of oxygen in liquid Fe as shown in **Table 5-2**. Conversely, it increases with TiO_2, albite, 1N·4S, or 1N·2S, all of which decrease the oxygen concentration. When ilmenite is added, FeO contained in ilmenite is the source of oxygen in liquid Fe. The other additives dilute FeO in molten slag, which leads to the decline in oxygen in liquid Fe. On the other hand, the interfacial tension between liquid Fe and molten slag is decreased by TiO_2 or ilmenite, and increased by albite, 1N·4S or 1N·2S. The effect of TiO_2 on the interfacial tension is opposite to that on the surface tension of liquid Fe. This tendency appears only in the case of TiO_2 addition. It is reported that the interfacial tension is affected by not only the adsorption as mentioned above but also the interface structure of slag side, that can be estimated based on the surface structure of molten slag [4]. The surface tension of molten slag increases with the addition of TiO_2 or ilmenite, and decreases with albite, 1N·4S or 1N·2S, which means that the effect of TiO_2 or ilmenite on the surface structure is different from that of albite, 1N·4S or 1N·2S. Therefore, it is considered that the effect of TiO_2 on the interfacial tension is affected mainly by the change of surface structure with the additive while the concentration of oxygen in liquid Fe changed by the additive is the main factor to vary the interfacial tension in the case of ilmenite, albite, 1N·4S or 1N·2S. The trend of contact angle between liquid Fe and molten slag, which is calculated by the balance of the above three tensions, indicates that the addition of TiO_2 or ilmenite decreases the contact angle and that of albite, 1N·4S or 1N·2S increases it, which is similar to that of interfacial tension.

The effect of interfacial tension between molten slag and liquid Fe on Fe recovery was initially investigated. It has been reported that an increase in interfacial tension between two liquid phases in a liquid-liquid system facilitates the coalescence of dispersed droplets in the

liquid by lowering interfacial energy [28-30]. In other words, when the interfacial tension between molten slag and liquid Fe increases, the coalescence of Fe particles becomes easier, which leads to an increase in the recovery of Fe alloy. **Figure 5-6** shows the variation in mean recovery with respect to interfacial tension for the selected experimental conditions. Although there appears to be a weak positive correlation, a distinct correlation cannot be identified owing to the wide scatter.

Figure 5-7 shows the variation in mean recovery with contact angle (θ). A strong positive correlation is observed between the contact angle and recovery. This result indicates that a high contact angle, which corresponds to poorer wettability, facilitates Fe recovery, leading to the coalescence of Fe particles. The proposed mechanism explaining the effect of wettability on the coalescence of Fe particles is as follows. When the molten slag wets Fe particles, it tends to penetrate the contact point between the particles due to capillary action. As the Fe particles come closer together, a repulsive force arises at this contact point [31]. In other words, molten slag interferes with contact between Fe particles, hindering their coalescence. As the contact angle increases, i.e., the wettability deteriorates, the repulsive force at the contact point between two particles decreases, leading to an increase in recovery. Consequently, it is considered that the observed variations in recovery were attributed to wettability changes caused by the added oxides, which influenced the coalescence of the Fe particles in the molten slag.

Regarding the effect of major oxides (TiO_2, Na_2O, SiO_2) on the coalescence with wettability change, the results in **Fig. 5-7** indicate that the contact angle and recovery ratio for TiO_2 (A4) and ilmenite (B4) are smaller than that of R. S (A0). This means that TiO_2 makes the wettability better and interferes with the coalescence of Fe particles in molten slag. On the other hand, the contact angle and recovery for 1N·4S (D4) and 1N·2S (E4) are higher than that of R. S (A0) as shown in **Fig. 5-7**. In particular, it indicates that the contact angle and recovery ratio increase as the amount of Na_2O added increases. That is, it is considered that Na_2O makes the wettability worse and promotes the coalescence of Fe particles in molten slag. When the concentration of SiO_2 in the regolith simulant increases, as in the cases of albite (C5), 1N·4S (D4), and 1N·2S (E4), the wettability becomes relatively worse compared to the addition of TiO_2 or FeO. Therefore, this suggests that wettability is a factor that greatly affects Fe recovery when recovering metal by gravity separation under low gravity.

Table 5-7 Calculated wettability parameters for different experimental compositions.

No.	σ_{Fe}	σ_{slag}	$\sigma_{Fe/slag}$	α	θ
R. S (A0)	1278	374	1009	37.81	50.96
TiO_2 (A4)	1291	377	996	32.89	44.75
Ilmenite (B4)	1200	379	892	29.95	42.20
Albite (C5)	1351	362	1102	40.56	52.89
1N·4S (D4)	1386	356	1148	42.43	54.52
1N·2S (E4)	1373	352	1145	43.59	55.82

*σ (mN/m), α (º), θ (º)

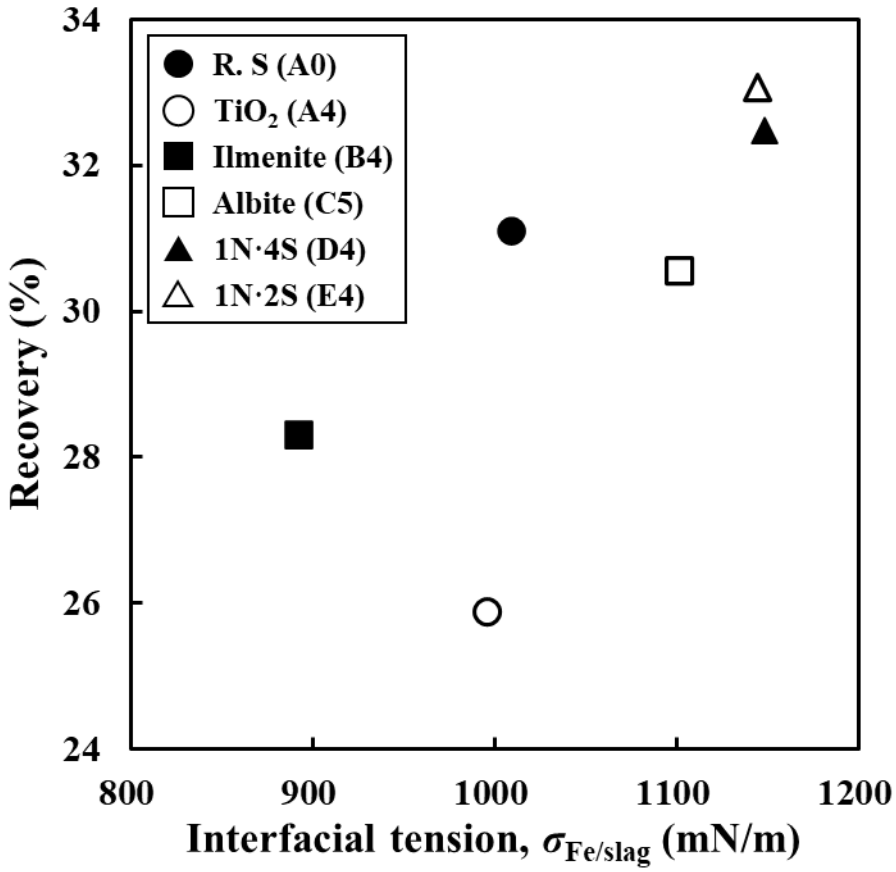

Fig. 5-6 Variation of mean Fe recovery from regolith simulant as a function of interfacial tension.

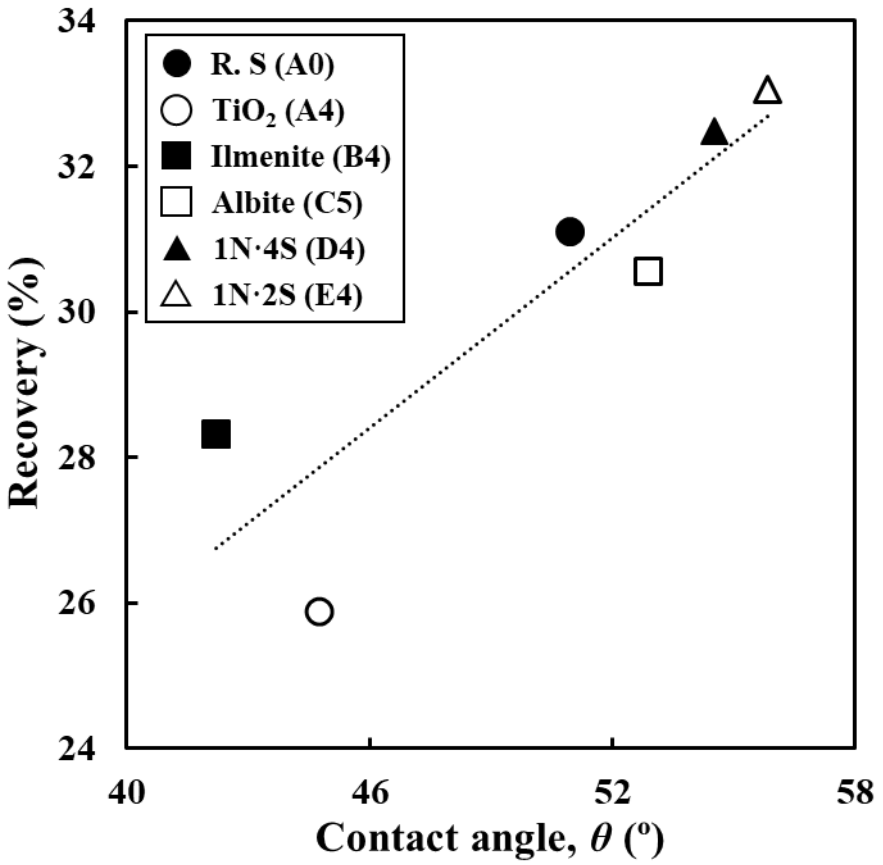

Fig. 5-7 Variation of mean Fe recovery from regolith simulant as a function of contact angle.

5.3.7 Effect of Capillary Action on Wettability between Droplets

The results in **Fig. 5-7** clearly show that wettability affects the coalescence of liquid Fe particles in molten slag. Nakamoto et al. [31] reported that the cause of the change in wettability was due to a change in pressure caused by capillary action acting on the particles at the point of contact between the particles in the molten slag. The coalescence behavior of liquid Fe in molten slag due to capillary action can be explained by Eq. (5-12).

$$\Delta P = P_1 - P_2 = -\frac{2\gamma_L \cdot \cos\theta}{H} \qquad (5-12)$$

Here, γ_L is the surface tension of the liquid, θ is the particle-liquid contact angle, and H is the capillary size, which represents the spacing between particles around the contact point. ΔP is the difference between the pressure (P_1) in the liquid and the pressure (P_2) in the gap formed by capillary action. The wettability between molten slag and metal is determined by the contact angle between them. Wettability is a phenomenon that occurs due to the difference in surface tension between the two liquids. SiO_2-based molten slags, such as regolith simulant, generally exhibit lower surface tension than liquid Fe, leading to good wettability with it [32]. Therefore, slag from regolith simulant will always form an acute angle with liquid Fe ($\theta < 90°$).

Figure 5-8 shows the direction of force acting on liquid Fe particles in molten slag in terms of wettability when $P_1 < P_2$. The black arrows in the figure indicate the direction of flow of molten slag at the contact point between two particles, while the blue arrows indicate the direction of the force acting on the liquid Fe particles due to capillary. When two liquid Fe particles in molten slag come into contact, the molten slag will penetrate the contact point between the two liquid particles (black arrow), as shown in **Fig. 5-8(a)**. A force is applied to the outside from the contact point of the Fe particles due to capillary action (blue arrow). Therefore, a repulsive force acts at the contact point between the particles as shown in **Fig. 5-8(b)**, making it difficult for the particles to coalesce.

As explained in chapter 3, coalescence occurs after drainage of the thin molten slag film between the droplets [33], which depends on the wettability. The repulsive force at the point of contact makes it difficult for the thin film to drain smoothly. That is, the better the wettability between the molten slag and the Fe droplets, the shorter the slip length, which slows down the drainage rate of the thin molten slag film between the Fe droplets, resulting in a slower

coalescence of Fe particles in the molten slag. On the other hand, the worse the wettability between molten slag and Fe droplets, the longer the slip length, which accelerates the drainage rate of the thin molten slag film between Fe droplets, resulting in accelerated coalescence of Fe particles in molten slag. In terms of the additives to the regolith simulant, TiO_2 and ilmenite are considered to be oxides that decrease the contact angle, whereas albite and $Na_2O{\cdot}xSiO_2$ compounds are considered to be oxides that increase the contact angle. Therefore, the coalescence of Fe particles in molten slag can be controlled by the additives to the regolith simulant, even in a system with good wettability, such as between the molten slag and Fe droplets.

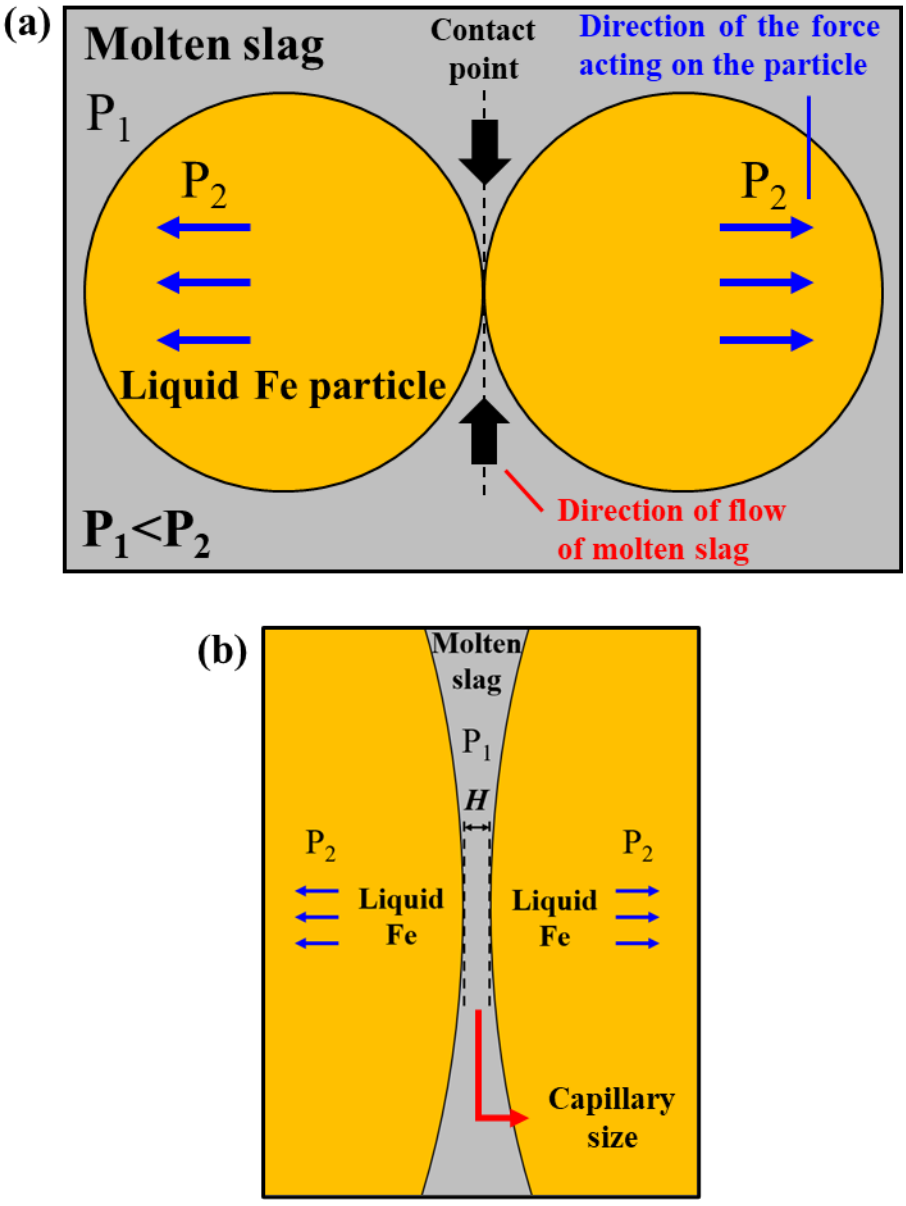

Fig. 5-8 Interfacial behavior between particles in molten slag. (a) Direction of the force acting on the particles when the molten slag wets liquid Fe particles. (b) Capillary size at the contact point.

5.4 Summary

High-temperature H_2 reduction and melting experiments were performed to extract and recover metallic Fe from lunar regolith simulant with the addition of various oxides. In addition, the differences in Fe recovery with the addition of oxides were investigated in terms of viscosity and wettability at the interface between molten slag and liquid Fe. The effect of wettability between molten slag and liquid Fe on the variation in Fe recovery was discussed based on the calculated contact angles. From the discussion of the relationship between wettability and coalescence, the following results were obtained.

(1) Recovery of the Fe alloy decreased with the addition of ilmenite, did not change with albite, and increased with $Na_2O{\cdot}xSiO_2$ compounds. This recovery trend is not explained by the viscosities of the respective molten slags.

(2) Recovery of the Fe alloy was strongly positively correlated with the contact angle between the molten slag and liquid Fe. It is concluded that wettability is a dominant factor for the recovery of Fe particles in these slags.

REFERENCES

[1] M. Nakamoto, Y. Tsugawa, A. Kiyose, J. Lee and T. Tanaka: J. High Temp. Soc., 32 (2006), 74.

[2] T. Paananen, K. Kinnunen: Steel Research Int., 80 (2009), 408.

[3] A. W. Cramb and I. Jimbo: Steel Research Int., 60 (1989), 157.

[4] K. Ogino, S. Hara, T. Miwa and S. Kimoto: Tetsu-to-Hagané, 65 (1979), 2012.

[5] K. Ogino, K. Nogi and C. Hosoi: Tetsu-to-Hagané, 69 (1983), 1989.

[6] G. R. Belton: Metall. Mater. Trans. B, 7 (1976), 35.

[7] T. Tanaka, T. Kitamura and I. A. Back: ISIJ Int., 46 (2006), 400.

[8] J. A. V. Butler: Proc. R. Soc. A, 135 (1932), 348.

[9] M. Nakamoto, A. Kiyose, T. Tanaka, L. Holappa and M. Hämäläinen: ISIJ Int., 47 (2007), 38.

[10] M. Nakamoto, T. Tanaka, L. Holappa and M. Hämäläinen: ISIJ Int., 47 (2007), 211.

[11] M. Hanao, T. Tanaka, M. Kawamoto and K. Takatani: ISIJ Int., 47 (2007), 935.

[12] T. Tanaka, K. Hack, T. Iida and S. Hara: Z. Metallkd., 87 (1996), 380.

[13] T. Tanaka, S. Hara, M. Ogawa and T. Ueda: Z. Metallkd., 89 (1998), 368.

[14] T. Ueda, T. Tanaka and S. Hara: Z. Metallkd., 90 (1999), 342.

[15] T. Tanaka and S. Hara: Z. Metallkd., 90 (1999), 348.

[16] T. Tanaka, M. Nakamoto and T. Usui: Proc. of Japan-Korea Workshop on Science and Technology in Ironmaking and Steelmaking, The Iron and Steel Institute of Japan, Tokyo, (2003), 56.

[17] R. D. Shannon: Acta Cryst., A32 (1976), 751.

[18] N. Ikemiya, J. Umemoto, S. Hara and K. Ogino: ISIJ Int., 33 (1993), 156.

[19] K. C. Mills and B. J. Keene: Int. Mater. Rev., 32 (1987), 1.

[20] G. J. Jang: NIST Properties of Molten Salts Database (formerly SRD 27), National Institute of Standards and Technology, (1992), https://doi.org/10.18434/mds2-2298, (accessed 2024-08-19).

[21] B. S. Mitin and Yu. A. Nagibin: Inorg. Mater., 7 (1971), 709.

[22] L. A. Girifalco and R. J. Good: J. Phys. Chem., 61 (1957), 904.

[23] H. Gaye, L. D. Lucas, M. Olette and P. V. Riboud: Can. Met. Quart., 23 (1984), 179.

[24] K. Mukai, H. Furukawa and T. Tsuchikawa: Tetsu-to-Hagané, 63 (1977), 1484.
[25] N. Shinozaki, K. Fujiike, K. Mori and K. Kawai: Tech. Rep. Kyushu Univ., 62 (1989), 575.
[26] H. Sun, K. Nakashima and K. Mori: ISIJ Int., 46 (2006), 407.
[27] Y. Mao, W. Luo, F. Lu and Y. Zhu: Gangtie, 22 (1987), 11.
[28] S. Natsui, R. Nashimoto, T. Kumagai, T. Kikuchi and R. O. Suzuki: Metal. and Mater. Trans. B, 48 (2017), 1792.
[29] Y. Chen, S. Narayan and C. S. Dutcher: Langmuir, 36 (2020), 14904.
[30] J. Isaksson, A. Andersson, T. Vikström, A. Lennartsson and C. Samuelsson: Journal of Sustainable Metallurgy, 9 (2023), 1378.
[31] M. Nakamoto, T. Tanaka, M. Suzuki, K. Taguchi, Y. Tsukaguchi and T. Yamamoto: ISIJ Int., 54 (2014), 1195.
[32] M. Nakamoto, H. Goto, M. Suzuki and T. Tanaka: Int. J. Microgravity Sci. Appl., 32 (2015), 320103.
[33] M. He, N. Wang, Q. How, M. Chen and H. Yu: Powder Technol., 362 (2020), 550.

Chapter 6
Conclusions

The purpose of this research is to design a process for extracting metal resources from lunar regolith and to investigate the various physicochemical properties of high-temperature melts, especially focusing on electrical conductivity of multicomponent slags and the wettability between molten slag and liquid Fe to realize “lunar metallurgy”. This dissertation consists of six chapters. The main conclusions presented in each chapter are summarized as follows.

Chapter 1: Introduction

“Lunar metallurgy” was defined in this dissertation as the extraction of metals from the lunar regolith. Metallurgical issues for two promising processes for utilizing lunar regolith, molten oxide electrolysis (MOE) and hydrogen reduction (HR), were discussed. This study aims to present a vision for the successful realization of lunar metallurgy based on a deep understanding of two metallurgical limitations that may arise in the process: (1) the electrical conductivity information of multicomponent oxides and (2) the coalescence mechanism of Fe droplets.

Chapter 2: Neural Network Modeling of Multicomponent Oxides for Estimation of Electrical Conductivity of Lunar Regolith

The electrical conductivity of multicomponent oxides for MOE process was accurately reproduced using neural network modeling. Using this predictive model, changes in electrical conductivity based on its composition and temperature variations in lunar mare regolith were estimated. The effect of oxides on electrical conductivity was influenced by the magnitude of the attractive force acting between cations and oxygen ions.

Chapter 3: Effect of Wettability on Coalescence Behavior of Droplet in Two Immiscible Liquids

Difference in wettability was confirmed to affect the droplet coalescence. Two immiscible liquids, liquid paraffin and 89% glycerin aqueous solution, were used in the experiment, and two cases were defined: “wetting” and “non-wetting”. The results of coalescence experiments

showed that wetting cases required more time for coalescence than non-wetting cases.

Chapter 4: Reduction and Recovery Behavior of Lunar Regolith Simulant to Metallic Fe by Hydrogen

Metallic Fe alloys were successfully recovered from lunar regolith simulant through the hydrogen reduction-melting process. Fine metallic Fe particles were dispersed inside the recovered slag. Therefore, increasing the sedimentation velocity through the coalescence of dispersed droplets was identified as an important issue to enhance the recovery ratio.

Chapter 5: Effect of Wettability on Coalescence of Dispersed Metallic Iron in Molten Lunar Regolith Simulant

Wettability was found to affect the recovery and coalescence of Fe droplets dispersed in molten slag. Wettability evaluation results indicated a strong positive correlation between the Fe recovery ratio and the contact angle. TiO_2 and ilmenite decrease the contact angle between molten slag and liquid Fe (better wettability), while albite and $Na_2O{\cdot}xSiO_2$ compound increase it (worse wettability).

This dissertation describes the physicochemical properties between molten slag and liquid Fe in pyrometallurgical Fe extraction from lunar regolith. The predictive model of the electrical conductivity for multicomponent oxides containing TiO_2 using neural network computation was developed, regarded as a guideline aiming to highly efficient MOE process to accommodate a multiple of lunar regolith. Clarification of the contribution of wettability to the coalescence of liquids gives new insight into interfacial properties to dynamic phenomena. Fe extraction from regolith simulant was demonstrated with reduction-melting process designed by thermodynamic calculation, and it was found that a higher recovery ratio was achieved by controlling wettability between molten slag and liquid Fe. These results emphasize the considerable influence of wettability on high-temperature processing, and furthermore, the indispensability of deep understanding of kinetics in the phenomena governed by wettability. Therefore, the findings in this dissertation are expected to contribute to the fields of surface and interface science, and the realization of lunar metallurgy and additionally the development of newly appeared pyrometallurgical processes in the future.

Publications

The main content of this dissertation is composed of papers published in the following academic journals.

1. “Effect of Titanium Dioxide on Aggregation of Reduced Metallic Iron in Molten Slag”:
   S. Lim, M. Nakamoto, K. Fuji-ta and T. Tanaka:
   Materials Transactions, Vol. 64 (2023), No. 3, 672–680.

2. “Estimation of Electrical Conductivity of Molten Multicomponent Slag by Neural Network Computation”:
   S. Lim, Y. Nobe, M. Nakamoto, K. Fuji-ta and T. Tanaka:
   ISIJ International, Vol. 64 (2024), No. 3, pp. 513–520.

3. “Effect of Wettability on Droplet Agglomeration in Two Immiscible Liquids”:
   S. Lim, I. Hatakeyama, M. Nakamoto, T. Yoshikawa and T. Tanaka:
   ISIJ International, Vol. 64 (2024), No. 8, pp. 1334–1337.

4. “Evaluation of Wettability at Interface between Molten Slag and Liquid Fe on Recovery of Metallic Fe from Lunar Regolith”,
   S. Lim, M. Ieuji, M. Nakamoto, K. Fuji-ta, T. Yoshikawa and T. Tanaka:
   ISIJ International, Vol. 64 (2024), No. 9, pp. 1345–1352.

Acknowledgements

I would like to give my sincere thanks to my supervisor, Professor Takeshi Yoshikawa, for his invaluable advice and guidance throughout my doctoral course. Thanks to his insight and expertise, I have improved not only the quality of my dissertation but also my research attitude. I am truly honored and grateful to have the opportunity to learn from such a respected scholar.

I would like to give my sincere thanks to my former supervisor, Professor Toshihiro Tanaka, for his valuable guidance. I received valuable advice from him in reviewing the theoretical considerations and experimental methods of this study.

I am grateful to the committee of my dissertation, Professors Yuichiro Koizumi, Hiroaki Tsuchiya, and Masashi Nakamoto, for their valuable comments and discussions on my research. Their comments were extremely helpful in improving the quality of my thesis.

I would like to thank Professor Masashi Nakamoto again, who contributed to this research, for his guidance and advice, which helped me overcome many challenges in conducting this study and writing this thesis.

I would also like to express my thanks to Professor Kiyoshi Fujita for his assistance and advice on geological knowledge, which was helpful in conducting this research.

I am grateful to Professor Masanori Suzuki for his advice in thermodynamics and experimental techniques for this study. I also wish to thank Professor Katsuyama Shigeru for his various forms of support in my lab life.

Lastly, I would like to thank my family for their unwavering support throughout my studies.

Sunglock Lim

Osaka, Japan
July 2024